Diffractively Coupled Resonators for Interferometric Applications and Optical Feedback to Laser Diodes

Von der Fakultät für Mathematik und Physik
der Gottfried Wilhelm Leibniz Universität Hannover
zur Erlangung des Grades

Doktor der Naturwissenschaften
– Dr. rer. nat. –

genehmigte Dissertation
von

Dipl.-Phys. Michael Britzger

geboren am 12. März 1979 in Marktoberdorf

2012

Referent:	Prof. Dr. Karsten Danzmann
Korreferent:	Prof. Dr. Roman Schnabel
Tag der Promotion:	14.12.2012

Abstract

All-reflective topologies based on reflection gratings are a promising approach for future laser interferometric gravitational wave (GW) observatories. Without light transmitted through a substrate, thermal effects are avoided that are associated with residual absorption in the bulk material. The latter limit the maximal light power employable in current GW detectors. Hence, all-reflective interferometry allows for higher amounts of light power and thus an enhancement of the shot-noise limited sensitivity.

In this work the interferometric applications of 3-port-grating coupled cavities were investigated. Such gratings have three orders of diffraction and can be mounted in second-order Littrow configuration. The low-efficiency first diffraction order acts as the coupling port to a Fabry-Pérot resonator whose end mirror is placed parallel to the grating surface. When 3-port gratings are used as coupling components to interferometer arm cavities, they create a second detection port. This topology was analyzed theoretically and experimentally. Dielectric 3-port gratings with minimal second-order diffraction efficiency were used in a table-top experiment where phase-modulation signals were generated inside the arm resonators and simultaneously detected at the two signal ports. Taking into account optical losses it was shown that with this multi-port readout scheme the signals add up to being equivalent to a Michelson-type interferometer with transmissively coupled arm cavities that have the same intra-cavity power.

The second application investigated in the framework of this thesis was the use of 3-port grating cavities for optical feedback to semiconductor laser diodes. Optical feedback is a widely used technique to improve the performance of semiconductor lasers. The investigated setup combined the principles of an extended cavity and an external resonator in a single device. The 3-port grating configuration has the potential to provide strong optical feedback, simultaneously realizing a laser with an inherent mode-cleaning device. For the proof of concept, an external cavity with a finesse of 1855 was realized, being the highest value ever reported for a 3-port-grating coupled cavity. With optical feedback, the laser threshold of the laser diode employed was reduced by a factor of four. Furthermore, high polarization discrimination and a circular TEM_{00} output mode were achieved.

Keywords: 3-port diffraction grating, all-reflective interferometry, optical feedback

Kurzfassung

Rein-reflektive Beugungsgitter sind ein vielversprechender Ansatz für laserinterferometrische Gravitationswellendetektoren. Sie vermeiden Transmission durch die optischen Substrate und die damit verbundenen thermischen Effekte aufgrund von Absorption, welche die maximal einsetzbare Lichtleistung in Detektoren begrenzen. Rein-reflektive Konzepte erlauben eine Erhöhung der Lichtleistung und somit eine Verbesserung der schrotrauschlimitierten Messempfindlichkeit von zukünftigen Detektoren.

In dieser Arbeit wurden zwei Anwendungen von Dreiport-Gitter-Resonatoren untersucht. Diese Gitter haben drei Beugungsordnungen und können in der zweiten Littrow-Ordnung aufgebaut werden. Hierbei dient die niedereffiziente erste Beugungsordnung als der Kopplungsport zu einem optischen Resonator, dessen Endspiegel parallel zur Gitteroberfläche positioniert ist. Die Verwendung eines solchen Gitters als Kopplungskomponente für den Armresonator eines Michelson-Interferometers und der daraus resultierende zweite Detektionsport wurden theoretisch und experimentell untersucht. Es wurde ein dielektrisches Dreiport-Gitter mit minimaler zweiter Beugungseffizienz verwendet. Im Experiment wurden Phasenmodulations-Signale erzeugt und an beiden Detektionsports detektiert. Unter Berücksichtigung der optischen Verluste wurde gezeigt, dass die Summe der detektierbaren Signale einen vergleichbaren Wert erreicht, wie in einem konventionellen Michelson-Interferometer mit transmittiv gekoppelten Armresonatoren und gleicher interner Leistung.

Die zweite Anwendung, die im Rahmen dieser Arbeit untersucht wurde, ist der Einsatz von Dreiport-Gitter-Resonatoren für optische Rückkopplung in Halbleiterlaserdiodensystemen. Um die optischen Eigenschaften von Laserdioden zu verbessern, wird optische Rückkopplung routinemäßig in der Laserphysik angewendet. Das präsentierte Konzept kombiniert einen erweiterten Resonator mit einem externen Resonator. Die untersuchte Konfiguration erlaubt starke optische Rückkopplung in Kombination mit einem inhärenten Modenfilter. Ein externer Resonator mit einer Finesse von 1855 wurde realisiert. Dies ist der bis dato höchste Wert für einen Dreiport-Gitter-Resonator. Durch die optische Rückkopplung konnte die Laserschwelle der verwendeten Laserdiode um einen Faktor vier gesenkt werden. Es wurden eine hohe Polarisationsreinheit und eine zirkulare TEM_{00} Ausgangsmode erzielt.

Stichwörter: Dreiport-Gitter, rein-reflektive Interferometrie, optische Rückkopplung

Contents

Abstract i

Kurzfassung iii

Contents v

1. Introduction 1

1.1. The detection of gravitational waves 1
1.2. Laser interferometric gravitational wave detectors 3
1.3. Dominant noise sources in GW interferometers 6
1.3.1. Fundamental noise sources 6
1.3.2. Thermal effects 8
1.4. All-reflective interferometry 9
1.5. Diffractive optics for optical feedback to laser diodes 12
1.6. Structure of the thesis 13

2. Properties of 3-port-grating coupled cavities 15

2.1. Diffractive optics 15
2.1.1. The grating equation 16
2.1.2. Dielectric reflection gratings 18
2.2. The scattering matrix formalism 20
2.2.1. 2-port scattering matrix 21

2.2.2. 3-port scattering matrix . . . 22
2.3. Optical resonators . . . 26
2.3.1. Linear Fabry-Pérot resonator . . . 26
2.3.2. 3-port-grating coupled cavity . . . 30
General description . . . 30
Light fields at the 3-port-grating coupled cavity . . . 32
2.3.3. Two cavities coupled with a 3-port grating . . . 36
Theoretical description . . . 37
Exemplary experimental configuration . . . 39
2.4. Signal response of optical resonators . . . 44
2.4.1. Modulation of light fields - The phasor picture . . . 44
Phase modulation . . . 44
Amplitude modulation . . . 46
2.4.2. Signal response of optical resonators in the phasor picture . . . 48
2.4.3. Linear Fabry-Pérot cavity in the phasor picture . . . 49
2.4.4. 3-port-grating cavity in the phasor picture . . . 50
Introduction . . . 50
3-port grating with $\eta_2 = \eta_{2\mathrm{min}}$ . . . 52
3-port grating with $\eta_2 = \eta_{2\mathrm{max}}$ . . . 53
3-port grating with $\eta_2 = \eta_{2\mathrm{mid}}$ . . . 54
2.5. Transfer functions . . . 56
2.6. Chapter summary . . . 60

3. A Michelson interferometer with grating arm cavities 63
3.1. Grating characterization . . . 63
3.2. Experimental setup . . . 66
3.2.1. General layout . . . 66
Laser preparation . . . 66
Elliptical mode matching . . . 66
Setup . . . 68
3.2.2. Arm cavities . . . 68
Grating cavity characterization . . . 70
EOM-induced loss . . . 71

Cavity mode matching and stabilization 73
3.2.3. Interferometer control 75
3.3. Measurement procedure and discussion 77
3.4. Chapter summary 80

4. 3-port gratings for optical feedback to laser diodes 81
4.1. Introduction 81
4.1.1. Optical feedback to semiconductor laser diodes 81
4.1.2. Regimes of optical feedback 83
4.1.3. Classical configurations for optical feedback 84
Extended resonators 84
External resonators 86
4.1.4. Concept of 3-port gratings for optical feedback 88
4.2. Second-order Littrow external-cavity diode laser 90
4.2.1. Laser diode and external cavity 90
4.2.2. Grating and grating-cavity characterization 92
4.2.3. Experimental setup 93
4.2.4. Results 96
Decreasing the laser threshold 96
Circular beam profile 98
Longitudinal single-mode operation 99
4.3. Conclusion 100

5. Summary and outlook 103

A. Characterization of 3-port gratings 107
A.1. 3-port gratings G0.035_x 107
A.2. 3-port gratings with very low first-order diffraction efficiency 108
A.3. High-finesse 3-port grating cavities 110
A.4. List of characterized 3-port gratings 111

Bibliography 113

Acknowledgements 127

Curriculum vitae **129**

Publications **131**

List of Figures

1.1. Effect of the two GW polarization modes h_+ and $h_\times$ on a ring of eight free-falling test masses 2
1.2. The effect of a $+$-polarized GW on a Michelson-type laser interferometer 4
1.3. Optical layouts of GW detectors 4
1.4. Design sensitivities of GW detectors from the first to the third generation 5
1.5. From transmissive to all-reflective 1 10
1.6. From transmissive to all-reflective 2 11
1.7. Three types of optical feedback configurations 13

2.1. Diffraction at an all-reflective grating 16
2.2. Littrow configurations 17
2.3. Grating structure with respect to the multilayer coating 19
2.4. Two photographs of 3-port gratings 20
2.5. Light fields at an (partially) transmissive component 21
2.6. Light fields at a 3-port grating 23
2.7. Light incident onto a 3-port grating 23
2.8. 3-port grating: Phases ϕ_1 and ϕ_2 as a function of η_2 25
2.9. Input and output amplitudes at a transmissively-coupled linear Fabry-Pérot resonator 26
2.10. Power reflectivity and transmittance of linear Fabry-Pérot cavities . . 29
2.11. Power transmittance of a linear Fabry-Pérot cavity 30

2.12. Scheme of the input and output amplitudes of a 3-port-grating coupled cavity . . . 31
2.13. Labeling of the ports of a 3-port-grating coupled cavitiy. . . . 33
2.14. Output characteristics of 3-port-grating coupled cavities. . . . 34
2.15. Output fields at the ports C1 and C3, in transmission of the end mirror, and the intra-cavity field . . . 35
2.16. Three-component cavities . . . 37
2.17. 3-port grating, grating cavity, and grating cavity with power-recycling 38
2.18. Intra-cavity power build-up in the arm cavity as a function of the detunings Φ_1 and Φ_2 of the PR cavity and the arm cavity . . . 41
2.19. Output power at the additional grating port $\mathrm{C3_{PR}}$ as a function of the detunings Φ_1 and Φ_2 of the power-recycling cavity and the arm cavity 42
2.20. Back-reflected power at port $\mathrm{C1_{PR}}$ as a function of the detunings Φ_1 and Φ_2 . . . 43
2.21. Phasor diagram for phase modulation sidebands . . . 46
2.22. Phasor diagram for amplitude modulation sidebands . . . 47
2.23. Illustrated signal outcoupling behaviour of linear and grating cavities. 48
2.24. Phasor diagram of a linear impedance-matched Fabry-Pérot cavity on resonance . . . 49
2.25. Power outputs at the two reflection ports C1 and C3 of a single-ended 3-port-grating cavity as a function of η_2 and the cavity detuning Φ. . . 51
2.26. Phasor diagram for a 3-port-grating cavity with $\eta_2 = \eta_{2\mathrm{min}}$ on resonance. . . . 52
2.27. Phasor diagram for a 3-port-grating cavity with $\eta_2 = \eta_{2\mathrm{max}}$ on resonance. . . . 53
2.28. Phasor diagram for a 3-port-grating cavity with $\eta_2 \neq \eta_{2\mathrm{min/max}}$ on resonance. . . . 55
2.29. Phasor diagram for the ports C1 and C3 of a 3-port-grating cavity with $\eta_2 \neq \eta_{2\mathrm{min}}$ . . . 55
2.30. Transfer functions for phase modulation sidebands for a single-ended linearly coupled Fabry-Pérot cavity . . . 57
2.31. Transfer functions for phase modulation sidebands at the 3-port-grating cavity . . . 59

2.32. Phase quadrature readout for the reflection port of the linear cavity and the two output ports of the grating coupled cavity 60

3.1. Michelson-type laser interferometers with conventional arm cavities and 3-port grating arm cavities 64
3.2. Grating characterization 64
3.3. Output characteristics of a 3-port-grating cavity as a function of the end mirror transmissivity. 66
3.4. Schematic of the experiment 69
3.5. Measurement of the cavity linewidth of the interferometer's arm cavity 2 70
3.6. Output characteristics and intra cavity fields of the two arm cavities depending on the optical loss 72
3.7. Outputs and PDH error signal of arm cavity 1 74
3.8. Outputs and PDH error signal of arm cavity 2 74
3.9. Visibility and stabilization scheme of detection port 1 76
3.10. Visibility and stabilization scheme of detection port 2 77
3.11. 13.7 MHz signals generated by $EOM_{1,2}$ and detected by $PD_{1,2}$ 79

4.1. Laser diode in an extended resonator configuration 85
4.2. Littrow configuration with a mode-selective grating in first-order Littrow mount 85
4.3. Littman-Metcalf configuration with a fixed grating and a rotatable mirror 86
4.4. Littman-Littrow configuration with a fixed grating and a second rotatable grating 87
4.5. Diode lasers with resonant optical feedback from an external cavity . 87
4.6. Concept of the laser diode with optical feedback from an external 3-port-grating coupled cavity 89
4.7. Amplification profile and CAD drawing of the AR-coated ridge-waveguide GaAs laser diode 90
4.8. Photographs of the laser diode and the external cavity 91
4.9. Photograph of the $1'' \times 1''$ fused silica substrate with the grating structure 92
4.10. Setup for the grating characterization procedure 93
4.11. Grating cavity prealignment setup 94

4.12. FSR of the external cavity 95
4.13. Schematic of the external-cavity diode laser setup 96
4.14. Laser diode output power as a function of the current at different output wavelengths 97
4.15. Output beam and major and minor beam profiles 98
4.16. Output mode and gaussian fit to the major beam width 99
4.17. Longitudinal single-mode operation observed with a scanning Fabry-Pérot interferometer 100

A.1. Photograph of the gratings after the EBL-process 109
A.2. Finesse of a 3-port grating coupled cavity as a function of the cavity loss and the first-order diffraction efficiency 111

Chapter 1

Introduction

1.1. The detection of gravitational waves

Almost 100 years ago Albert Einstein laid the foundation for the field of modern gravitational physics with the publication of his article "Die Grundlagen der allgemeinen Relativitätstheorie" [1]. In contrast to classical Newtonian gravity where space and time are independently represented as a constant and stiff background, Einstein's General Theory of Relativity describes '*space-time*' as a dynamically variable geometry. One consequence of the theory predicted by Einstein himself is the existence of gravitational waves (GW) as tidal distortions of space-time that propagate at the speed of light [2, 3]. These ripples in the curvature of space-time are caused by accelerated masses. A gravitational wave manifests as a stretching and squeezing of the geometry of space-time transversal to the GW's direction of propagation. The GW's amplitude is often referred to as *strain* [4] and is defined as a relative length change according to

$$h = \frac{2\,\Delta L}{L}, \tag{1.1}$$

where ΔL is the change in the distance L between two spacetime events that are caused by a GW. Due to the high elastic stiffness of space-time, very large masses, moving at relativistic speeds, are needed for a nominal effect on space-time. Promising sources are massive astrophysical objects such as neutron star and/or black hole binaries and their coalescences, supernovae and pulsars. But also the remaining gravitational fingerprint of the early universe from times where it was not yet transparent

for electromagnetic waves is a source for a gravitational background radiation. For a more profound discussion of the General Theory of Relativity and potential sources for gravitational waves see [5–7].

A GW can be expressed as a superposition of the two polarization modes h_+ and $h_\times$ [8]. The effect of an accordingly polarized GW is often illustrated as in Fig. 1.1: It shows the effect of a GW on a ring of free-falling test masses for the two polarizations over one full cycle of the GW. The direction of propagation of the GW is perpendicular to the image plane. For both polarizations the distance between the masses is squeezed and stretched in the orthogonal direction, respectively.

Since the mid 20th century the detection of gravitational waves is one major goal of physicists all around the world. The first direct detection would not only provide another profound proof of Einstein's Theory, but it will open a new window for astronomy to detect events that cannot be accessed by observation in the electromagnetic spectrum. This will establish a new era of gravitational wave astronomy.

The first indirect evidence of the existence of GWs was achieved by Russell Hulse and Joseph Taylor and reported to the community in 1979. They observed a decrease in the orbital period of the neutron star binary PSR19132+16 that fitted the energy loss due to emission of gravitational waves predicted by the Theory of General Relativity [9, 10]. For this discovery the Nobel prize was awarded to Hulse and Taylor in 1993. A direct detection has, however, not been realized up to now.

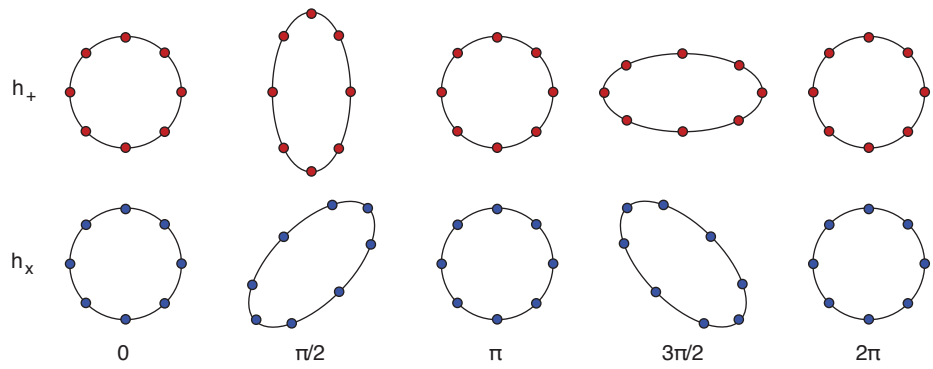

Figure 1.1.: Effect of the two GW polarization modes h_+ and $h_\times$ on a ring of eight free-falling test masses over one full cycle of the GW. The distance between the masses is squeezed and stretched in the orthogonal direction, respectively.

In principle, the detection relies on the measurement of the GW-induced distance variations between test-masses. It is the tininess of the relative length changes that makes the direct detection of gravitational waves one of the most challenging endeavours in modern experimental physics. Even the relative length change induced by massive astrophysical events such as merging neutron stars or black holes and supernovae are extremely small. For instance, when measuring on earth a supernova at a distance of 10 kpc (hence well inside our galaxy) is expected to result in a strain of only $h \approx 10^{-22}$ [11].

First attempts at a direct detection were undertaken by Joseph Weber and his team in the 1960's. Their approach employed aluminum cylinders as so-called resonant bar detectors for the length measurement. The GW should excite a resonant mode of the bar. The movement could then be detected by attached piezo-electric transducers. In 1969 Weber claimed to have performed a direct detection of GWs [12], but his results were never reproduced, and thus the scientific community did not accept his findings. Nevertheless the race was opened to develop instruments sensitive enough for a direct detection of GWs. First efforts were undertaken with other bar detectors and it was shown that Weber's instrument could not have been sensitive enough for an actual detection [13–15]. More and more the development of large-scale laser-interferometric detectors became the focal point of interest of the fast-growing international GW community [16]. Due to their broadband detection ability and rapidly evolving technologies these instruments have become the most promising approach for a direct detection nowadays [7].

1.2. Laser interferometric gravitational wave detectors

Laser interferometric gravitational wave detectors are based on the concept of a Michelson-type interferometer. Figure 1.2 illustrates the effect of an incident GW on such a detector. The GW causes a differential arm length change and thus an effective phase shift between the light fields propagating along the two arms of the interferometer. This differential modulation of the arm length can be detected at the output port of the detector as a change of the interference pattern at the GW's frequency.

The phase shift induced by the GW depends on the arm length as well as on the wavelength of the laser used. In addition to long arms, the sensitivity of a conven-

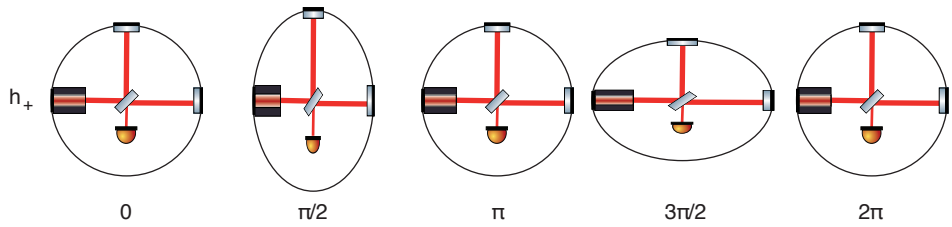

Figure 1.2.: The effect of a +-polarized GW on a Michelson-type laser interferometer. The direction of propagation is perpendicular to the plane defined by the arms of the interferometer.

tional Michelson interferometer can be enhanced by increasing the amount of optical power stored in the arms [4, 8]. For this several optical layouts and concepts have been developed as illustrated in Fig. 1.3. Optical resonators in the arms as shown in Fig. 1.3 (c) can be used to increase the circulating light power. The power-recycling technique resonantly enhances the carrier light by introducing a power-recycling mirror in the entrance of the interferometer. The signal recycling technique follows the same principle to resonantly enhance the signal [see Fig. 1.3 (b)] [8].

An international network of ground-based detectors has been established over the last two decades. These large-scale detectors utilize variations of these optical concepts. The instruments of the LIGO collaboration (Laser Interferometer Gravitational Wave Observatory) are located in the USA at two sites in the states of Louisiana (Livingston) and Washington (Hanford) with arm lengths of 4 km [17]. The LIGO interferometers utilize arm-cavities and power-recycling as depicted in Fig. 1.3 (c).The Virgo

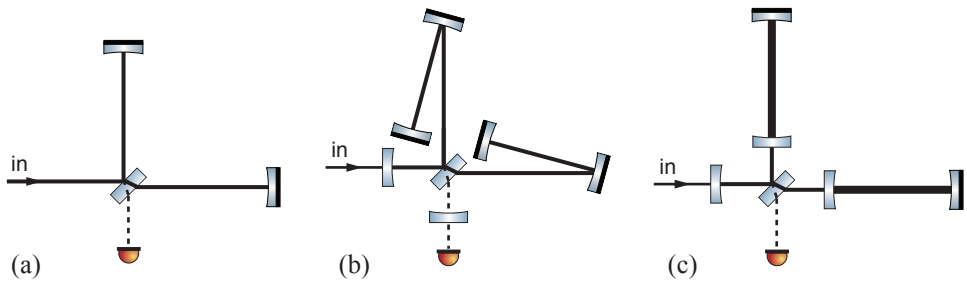

Figure 1.3.: (a) The classical layout of a Michelson interferometer. (b) The GEO600 detector employs 600 m arms that are folded once as well as the dual-recycling technique. (c) The LIGO detectors and the Virgo detector have arm cavities and a power-recycling cavity.

detector of the French-Italian cooperation has a similar optical layout. It has 3 km long arms and is located in Cascina, Italy [18]. The observatory of the German-British collaboration GEO600 was built near Hannover in Germany. It has 600 m arms that are folded once resulting in an effective optical path length of 1200 m [19]. It does not employ arm cavities, but the so-called *dual*-recycling as shown in Fig. 1.3 (b) [20, 21]. This first generation of ground-based detectors has successfully taken data over several *science runs* although no direct detection has been realized up to now [22, 23]. The designed strain sensitivities of initial, advanced and future interferometers are shown in Fig. 1.4.

While GEO600 is currently the only observatory taking data currently and being upgraded simultaneously [24, 25], the LIGO and Virgo detectors are shut down at the moment for major upgrades into Advanced LIGO [26] and Advanced Virgo [27]. In the same vacuum system as the 4 km interferometer in LIGO Hanford a 2 km instrument was established initially, which is now planned to be relocated to India as a second generation detector [28]. The upgrade to the second generation will signifi-

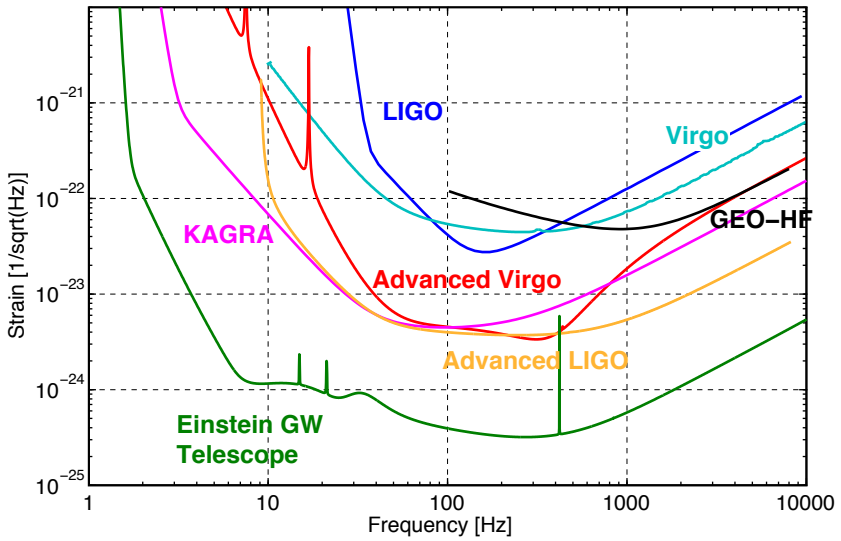

Figure 1.4.: Design sensitivities of current and planned laser interferometric GW detectors. First generation: LIGO, Virgo. Second generation: GEO-HF, Advanced Virgo, Advanced LIGO and KAGRA. Proposed third generation: Einstein GW Telescope. Source: see Ref. [32].

cantly increase the sensitivities and, consequently, the detection probability. Thus the network of the second generation gravitational wave observatories is expected to operate and to finally detect for the first time within the near future [29]. Recently, a Japanese observatory KAGRA (initially named LCGT) was approved; it will be the first large-scale detector operating underground and at cryogenic temperatures [30]. Meanwhile, an extensive study has been carried out to define technical, infrastructural and scientific prospects of a European third-generation observatory, the Einstein Telescope (ET) [31, 32]. While second-generation devices are expected to present a first direct GW detection, it will be the third-generation observatories that will reach sensitivities high enough to enable routine gravitational wave astronomy.

1.3. Dominant noise sources in GW interferometers

1.3.1. Fundamental noise sources

The interferometric GW observatories built and operated over the last two decades are the most sensitive length measurement devices ever built by mankind. For an up-to-date introduction the author refers to Ref. [7] and the references therein. The three fundamental noise sources that currently are or will be limiting factors for every ground-based laser-interferometric detector are

Seismic noise Distortions of the surrounding environment couple to the detector and, at frequencies below a few tens of Hertz, lead to a signal that is not distinguishable from a GW's signal and thus might mask or imitate a real signal. To isolate the test masses from the environment and to attenuate the seismic vibrations and disturbances complex passive and active concepts are pursued as well as multistage pendulum systems [33]. Additionally the instrument is housed in a large vacuum system. An overview on the requirements for future detectors is given in [32]. It includes the so-called 'gravity-gradient noise' that is a Newtonian gravitational interaction between the test masses and the surrounding soil and local seismic activities that cannot be shielded from the mirrors.

Quantum noise The noise source that originates from the quantum nature of light and constitutes a fundamental limit to the the sensitivity of standard interferometers is called *quantum noise*. At high frequencies *shot noise* is the limiting noise; phase fluctuations of the vacuum noise that can be seen as a photon counting error. Zeropoint fluctuations of the electromagnetic field entering the system at the interferometer's dark port cause apparent displacement noise when being detected with the photo detector in the detection port of the interferometer. A GW signal at the output port is proportional to the laser power whereas the relative shot noise itself is proportional to only the square root of the laser power [6]. Thus, the shot noise level in terms of displacement can be reduced by increasing the circulating laser power in the interferometer. For this reason arm cavities and power recycling techniques are used in GW interferometers.

Improving the shot-noise limited sensitivity by increasing the circulating light power will in return enhance the *radiation pressure noise* proportionally to the square root of the laser power [34]. This noise originates from amplitude fluctuations of the vacuum that "shake" the mirrors and thereby cause a noise floor that falls off as a $1/f^2$ slope above the resonance frequency of the pendulum system [29]. It is thus only significant at low frequencies. Although radiation pressure noise is not yet a limiting noise source it is expected to limit the sensitivity of future detector generations. Thus the circulating laser power should be optimized for the best sensitivity. For the Einstein Telescope a so-called xylophone mode has been proposed consisting of two independent interferometer-types optimized respectively for high and low frequencies using optimal power levels of the circulating laser light. While in one interferometer the stored power is planned to reach the Megawatt-range for an improvement of the shot-noise limited sensitivity in the upper frequency-band, in the second interferometer the circulating laser power will be at kilowatt-level for lower radiation pressure noise and optimized sensitivity at low frequencies, correspondingly [32].

Thermal noise The limiting noise in the mid-frequency detection band originates from thermally driven motion due to non-zero temperatures of the substrates, the suspensions and the mirror coatings that is commonly referred to as *thermal noise* [35,36]. The mirror thermal noise affects the mirror's substrate as well as the coatings. The three major contributions can be divided into Brownian thermal noise, which is a dis-

placement of the mirror surface induced by Brownian motion, and the closely related thermo-elastic [37] and thermo-refractive [38] noises. Thermo-elastic noise is due to temperature fluctuations that on their part drive mechanical noise in the material due to a non-zero expansion coefficient of the substrates and the coatings. In analogy, the thermo-refractive noise is due to a temperature dependent change of the index of refraction of materials. Thermally-induced fluctuations will therefore change the optical path length which makes this noise source mainly important for transmissive optics. The mirror coatings, however, also contribute to the thermo-refractive noise since the multilayer stacks are still partially illuminated in the reflection process.

The total amount of thermal energy (integrated over the frequency) is constant and is determined by the temperature of the system [7]. Brownian thermal noise can be reduced by concentrating the thermal energy in sharp resonance peaks well outside the detection band which is done by using materials with high mechanical quality, namely low energy dissipation. Hence, thermally-induced fluctuations are concentrated around the resonant frequencies which then reduces the thermal noise contribution in the off-resonance region. Materials of the test masses as well as the suspensions and coatings need to have low mechanical loss to avoid thermally driven broadening of the resonance peaks and the simultaneous increase of the off-resonant noise.

Future GW detectors are expected to be limited by thermal noise [36]. An approach to improve the sensitivity without changing external parameters is the operation at cryogenic temperatures. KAGRA, the second-generation Japanese GW observatory currently under construction is planned to operate at a test mass temperature of 20 K [30].

1.3.2. Thermal effects

Thermally driven effects in the interferometer's optical components induced by absorption are described by the term *thermal effects*. The materials that are currently employed in GW detectors show residual absorption with values as low as 1 ppm/cm or lower [39]. Absorption leads to local heating in the beamsplitter or the coupling components to the arm cavities. Since the expansion coefficient of most materials is not zero this absorption-induced heating leads to a deformation of the component's surface and a distortion of the wavefront which in the end degenerates the interference

fringe at the output port of the interferometer and consequently limits the amount of power employable in the interferometer [40].

Another thermal effect is the so-called thermal lensing. The transmission-induced absorption causes a temperature gradient in the substrate. Since the index of refraction is a function of temperature, this leads to a gradient of the optical path length around the optical axis [41]. In analogy to the change of the geometrical optical parameters by a conventional lens this causes a change of the radius of curvature of the wavefront. Hence, the amount of storable power and thus the sensitivity of the interferometer is limited by these two thermal effects.

1.4. All-reflective interferometry

Thermal lensing might become a problem for the second generation and all the more for the third generation detectors [32, 42]. In general thermal effects and thermal noise will be a limiting factor in the most sensitive frequency band of interferometric GW detectors. The choice of optical materials is strongly restricted to materials of thermally and mechanically high quality that additionally are highly transparent for the used laser wavelength. However, when further increasing the stored power even the tiniest absorption will eventually induce effects that set a limit to the sensitivity achievable.

All-reflective gratings have been proposed for use in future detectors because of their ability to split and recombine monochromatic light without transmitting light through the optical component [43, 44]. Since an all-reflective replacement of the (partially) transmitting mirrors avoids any transmission, all-reflective optics eliminate all absorption-induced thermal effects in the bulk material. In addition, they permit the use of opaque or less transmissive substrates that may allow cooling down to temperatures not achievable with transmissive substrates. Materials such as crystalline silicon for potential substrate candidate might be used in all-reflective topologies [45]. In comparison to the currently used fused silica, silicon offers favorable mechanical properties at cryogenic temperatures but is not transparent at the currently used wavelength of 1064 nm [32, 46].

Figure 1.5 summarizes the basic principle of all-reflective optics. Every partially transmissive optic in an interferometer can be replaced by an appropriate diffractive

component [see Fig. 1.5 (a)]. Thus, diffractively coupled cavities that can replace arm cavities inside interferometers are feasible without having to transmit light through a substrate [see Fig. 1.5 (b)].

In 2003, within the Sonderforschungsbereich TR7 [47], a joint project was started between the Universities of Hannover and Jena in order to evaluate the prospects of all-reflective interferometer topologies by using custom made dielectric diffraction gratings as potential all-reflective replacements of the transmissive key components of optical resonators and laser interferometers. Within the last decade, various experimental and theoretical investigations of dielectric all-reflective interferometric concepts were carried out. As all-reflective cavity couplers high-efficiency gratings with two orders of diffraction were investigated that are mounted in first-order Littrow configuration [48]. These two-port gratings have, however, the drawback of stringent restrictions on beam pointing and alignment [49]. An alternative with considerably relaxed requirements is provided by the so-called *3-port* gratings used in second-order Littrow configuration where the angle of the incident laser beam and the grating period are chosen such that the second diffraction order is back-reflected towards the laser source. Thus, the diffraction efficiency of the first diffraction order is used as the

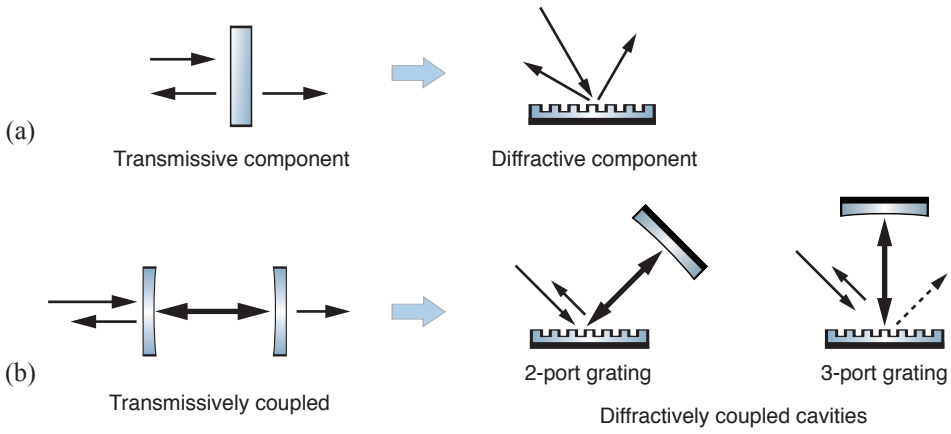

Figure 1.5.: From transmissive to all-reflective: (a) Every (partially) transmissive mirror can be replaced by an appropriate diffraction grating. (b) Gratings with two orders of diffraction (resulting in two ports) and three orders (three ports) mounted in Littrow configuration can be employed as diffractive couplers to Fabry-Pérot cavities.

coupling efficiency to a resonator that is arranged perpendicular to the grating surface. Low-loss 3-port gratings as potential all-reflective cavity couplers as shown in Fig. 1.5 have been investigated theoretically and experimentally [50, 51]. Note that the optical layout of the interferometer changes considerably when choosing all-reflective topologies. In Fig. 1.6 (a) this shown for a Michelson-type interferometer with a diffractive 50/50 beamsplitter and with power-recycling [52, 53].

However, the dominant noise source limiting the GW detectors in the mid-frequency band will not originate from the bulk materials, but from the coating of the mirrors [54–56]. Currently used multilayer coatings for a wavelength of 1064 nm consist of alternating layers of SiO_2 and tantala (Ta_2O_5) as the high index layer. The thermo-refractive noise contribution originates from the tantala layers although only some microns of this material are applied to the bulk material. Therefore several alternatives have been investigated to minimize the coating-thermal noise such as doping the tantala with TiO_2 [57] or replacing the end mirror by a system of mirrors to reduce the number of tantala layers that are exposed to the high build-ups of the intra-cavity

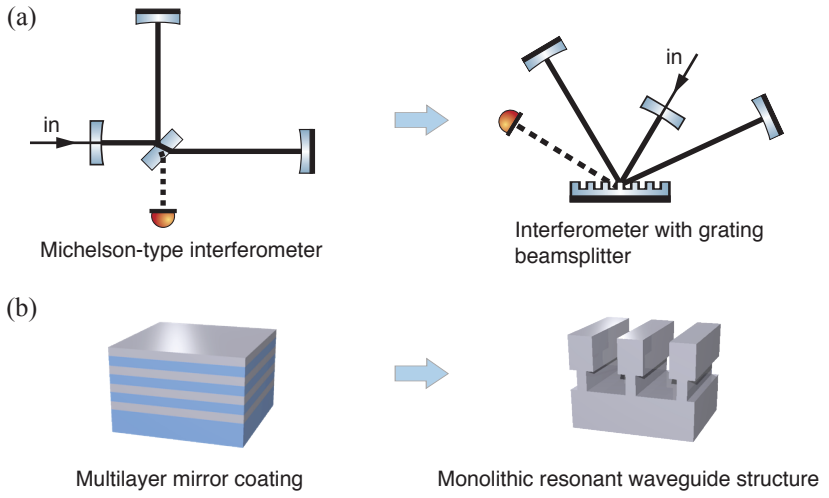

Figure 1.6.: From transmissive to all-reflective: (a) The (partially) transmissive beamsplitter of a Michelson-type interferometer can be replaced by an all-reflective 50:50 diffraction grating beamsplitter. (b) The resonant waveguide structure can be realized with a monolithic T-structure to act as highly reflective and coating-free surface [61].

field [58]. One approach, investigated in the framework of the Hannover-Jena collaboration, follows the idea of so-called resonant waveguide gratings which also make use of nanostructured surfaces [59]. They reduce the amount of applied tantala to only one layer or can even be manufactured without any additional coating layer [60]. In this context a monolithic and highly reflective waveguide structure from a single silicon crystal for a wavelength of 1550 nm was demonstrated recently [61]. The corresponding monolithic T-structure is depicted in Fig. 1.6 (b).

The combination of coating-reduced or coating-free waveguide grating mirrors and diffractive components is therefore an issue that is currently under investigation within the collaboration to finally realize a coating-free *and* all-reflective interferometry [62].

1.5. Diffractive optics for optical feedback to laser diodes

In laser physics diffraction gratings have a widespread application as frequency selective devices [63]. In the framework of the Hannover-Jena collaboration 3-port gratings have been studied intensively and, apart from their interferometric applications, it was proposed to use 3-port grating cavities for optical feedback to semiconductor laser diodes [64].

Optical feedback is a technique widely used to enhance the performance of laser diode systems [65]. In this process, a part of the emitted light field is spectrally filtered by an external device and then sent back to the laser diode. One approach, commonly referred to as *first-order Littrow configuration*, employs an optical grating placed outside the front facet of the laser diode [see Fig. 1.7 (a)]. The grating provides spectral selectivity for the optical feedback and forms an extended cavity with the back facet of the diode [66]. Figure 1.7 (b) shows the *Littman configuration* [67] which enhances the Littrow-setup by an additional mirror serving as the tuning component that reflects the diffracted order. In both cases, however, optical loss channels as well as the elliptical beam profiles limit the performance and applicability. A similar approach is given by the use of external cavities for resonant optical feedback [68]. This concept, usually referred to as a *diode laser with resonant optical feedback* has the advantage that the reflectivity values achievable for dielectric HR mirrors are usually orders of

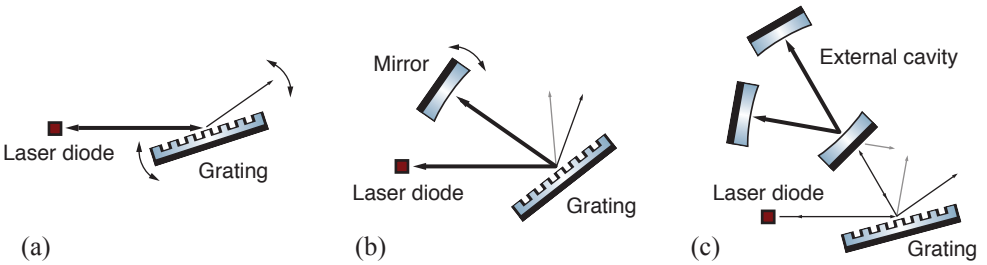

Figure 1.7.: (a) Extended resonator laser diode with a grating in first order Littrow mount. (b) Littman-configuration with an additional rotatable mirror. (c) Grating enhanced external cavity setup for optical feedback.

magnitude higher than the corresponding performance of optical gratings. Thus, much higher optical finesses can be realized. Depending on the finesse of the external cavity and on the strength of the optical feedback, linewidths of a few kHz and tuning ranges of a few hundred MHz can be achieved. Up to now, proposals to combine gratings and external resonators (e. g. [69]) suffer from the disadvantage of a fairly complex setup involving several optical components and thus from growing handling complexities.

The optical feedback concept proposed within the framework of this thesis combines the principles of an extended laser diode resonator and an external resonator by using an external cavity with a dielectric 3-port grating as the coupling component. This combines the frequency selectivity of a grating with the linewidth narrowing of an external cavity. Such a cavity can provide an exceptionally strong optical feedback hand-in-hand with a high-finesse cavity, and thus, the external 3-port-grating coupled cavity makes it possible to yield a spectrally and spatially filtered output beam with a perfectly circular profile. Furthermore, the proposed concept combines the laser light source and a mode-cleaning cavity [70] in one single device. Thus, it provides a high-quality TEM_{00} spatial mode at almost any wavelength in the VIS and near-IR band, depending on the laser diode used.

1.6. Structure of the thesis

The focus of this thesis was the investigation of the interferometric applicability of 3-port diffraction gratings, in particular the application of 3-port-grating coupled cav-

ities. Two main issues were addressed. The first application that has been investigated theoretically and experimentally in the framework of this thesis is the use of 3-port gratings as cavity couplers to the arm cavities of an all-reflective Michelson-type interferometer. The second application proposed and demonstrated here is the use of 3-port-grating coupled cavities for optical feedback to semiconductor laser diodes.

Chapter 2 provides an introduction to diffractive optics that is followed by the theoretical description of 3-port gratings using the scattering-matrix formalism. These gratings have a symmetrical rectangle profile with respect to the grating normal (binary structure). Since a 3-port grating splits and combines three instead of (e.g. for a partially transmissive mirror) two light fields, the consequences on the cavity output-characteristics are investigated.The theoretical considerations were experimentally verified with two cavities that were coupled by a 3-port grating. The results of this earlier work are summarized. Grating cavities were investigated with respect to phase modulation signals. The transfer functions and the phasor picture as a more intuitive approach are provided.

Chapter 3 presents the experimental realization of a Michelson-type interferometer with 3-port grating arm resonators. It provides an optical characterization of the diffractive couplers that were used, along with a discussion of the experiment. Phase-modulation signals are generated inside the arm resonators and simultaneously detected at the two signal ports. It was shown that the signal can be summed to be equivalent to a single-output-port Michelson interferometer with arm cavities, taking into account optical loss in agreement with the theoretical consideration in Chap. 2.

Chapter 4 presents the proposal and the proof of concept of an external-cavity diode laser with 3-port-grating cavity as the external device for optical feedback. An introduction to optical feedback techniques and commonly used configurations and the characterization results of the employed 3-port grating and the external high-finesse cavity are provided. The successful optical feedback is verified by a decrease of the laser threshold. Measurements of the output profile are presented.

Chapter 5 sums up the research carried out in the framework of this thesis and provides an outlook to further research on all-reflective interferometry and to potential applications of 3-port grating cavities for optical feedback. The Appendix A contains a list of 3-port gratings that were manufactured in Jena and characterized in Hannover regarding their diffraction efficiencies and optical loss.

Chapter 2

Properties of 3-port-grating coupled cavities

In this chapter, an introduction to diffractive optics is provided, followed by the theoretical description of binary 3-port gratings using the scattering-matrix formalism. Such a grating has to be described by a 3×3-matrix, since it splits and combines three light fields at each port of the grating. As a consequence, the light fields that interfere at the ports of the 3-port-grating cavity show a more complex behavior with respect to their relative phases that depends on the diffraction efficiencies of the grating. The phasor picture offers an intuitive view into that behavior. In its context the signal response of 3-port grating cavities is determined.

2.1. Diffractive optics

Diffraction gratings are optical devices with a periodically structured surface. Similar to prisms, gratings redirect the incident light beam into new directions by sending each color into an unique exiting angle, a phenomenon known as dispersion. Because of their wavelength selectivity gratings offer a broad spectrum of applications in various scientific and industrial fields. They are used for pulse compression in non-linear optics [71], for spectroscopy [63] and in numerous applications for optical feedback configurations in laser optics (see Chap. 4).

2.1.1. The grating equation

Traditionally gratings have been used in experiments employing polychrome light. More recently their applications for single-frequency configurations have come into focus. For monochromatic light, the diffraction characteristics of a reflection grating are completely described by

$$\sin\alpha + \sin\beta_m = \frac{m\lambda}{d}, \tag{2.1}$$

where λ is the wavelength of the field that is incident at an angle α onto a reflection grating with the grating period d [72]. The reflected light field of the mth diffraction order is diffracted into the corresponding diffraction angle β_m. The angle's sign is defined with respect to a plane perpendicular to the grooves at the grating center (see Fig. 2.1). The validity of Eq. (2.1) is restricted to cases in which the incident and diffracted beams are perpendicular to the grooves [72]. For the zeroth diffraction order ($m = 0$) the diffraction corresponds to a conventional reflection at a surface with $\alpha = -\beta_0$. The diffraction order is an integer and – according to the grating equation – is restricted to cases where $|m\lambda/d| \leq 2$ is valid. The special case of

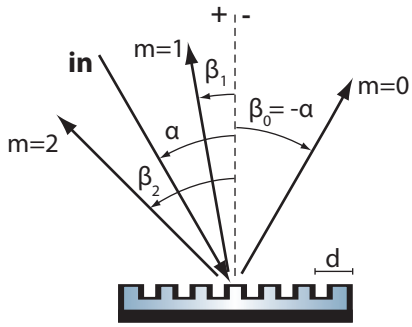

Figure 2.1.: Diffraction at an all-reflective grating with the period d, the angle of incidence α and the diffraction angle β_m of the mth diffraction order.

the equal angles of the incident monochromatic beam and the mth diffraction order ($\alpha = \beta_m$) is termed mth-order LITTROW-configuration where Eq. (2.1) simplifies to

$$2\sin\alpha = \frac{m\lambda}{d}. \tag{2.2}$$

In this case, the mth diffraction order is reflected back towards the light source. A grating mounted in Littrow-configuration can be used for optical feedback experiments since it reflects a spatially filtered part of the incident light back to the source as described in Chap. 4. Moreover, this configuration provides the possibility to use the grating as an all-reflective coupling component to an optical cavity, replacing a conventional transmissive mirror. Figure 2.2 shows two different types of gratings in Littrow configuration. This arrangement that historically has been termed as "Littrow-mount", is a grating with two diffraction orders ($m = 0, 1$) where the first diffraction order is diffracted towards the source with $\alpha = \beta_1$. Such a grating, optimized for a certain wavelength, is called a 2-port-grating. Here, the (low-efficiency) zeroth diffraction order can be used to couple light into a cavity [73]. The 3-port grating in Fig. 2.2 provides an additional diffraction order and an additional port, respectively. Here, the second-order Littrow restrictions in the grating equation ($\alpha = \beta_2$) yield the angle $\beta_1 = 0$ for the first diffraction order that provides the coupling to a cavity that is arranged perpendicular to the grating surface. Thus, high-finesse cavities are feasible, if one assumes a low first-order coupling-efficiency and a high reflectivity at normal incidence. Throughout this work, all diffractively coupled cavities implemented were 3-port-grating coupled.

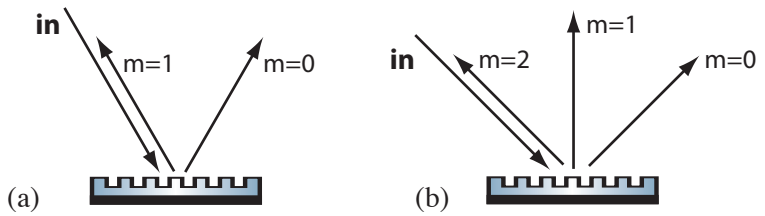

Figure 2.2.: (a) 2-port grating in first-order Littrow mount. (b) 3-port grating in second-order Littrow mount.

The grating period d is the only grating parameter addressed in the grating equation. If more than one diffraction order exists, the incident power divides into the diffracted orders. Note that the power diffraction efficiencies (i. e. the ratio of power distribution into the diffraction orders) are not described by Eq. (2.1). They are defined by other grating parameters such as the geometry of the periodic structure (e.g. binary or blazed) or the index of refraction of the used materials. The dielectric gratings used in

this work are binary structured, which means that the diffractive structure is a symmetrical rectangle profile with respect to the grating normal. The relevant grating structure parameters are the groove depth and the fill factor, which is the ratio of groove width to ridge width.

2.1.2. Dielectric reflection gratings

Since the end of the last century dielectric reflection gratings gained more and more in importance, because they provided higher damage thresholds in comparison to the traditionally used metal gratings (for a historical overview, see [72,74]). Initially, low-efficiency all-reflective gratings were etched in the upmost layer of highly reflective multlayer stacks [75]. Since that time, a rapid evolution took place with respect to simulation methods, computational and manufacturing skills, electron beam lithography and etching techniques [76]. In interferometric applications dielectric gratings attracted notice when Sun *et al.* demonstrated an all-reflective Sagnac interferometer in 1998 [73], motivated by earlier all-reflective proposals for future gravitational wave detectors [43, 44]. Still using metal gratings as a beam splitter Sun stated in his publication: "*Gratings that are etched on the top of multilayer dielectric coatings have lower loss, higher damage threshold, and more precisely controllable diffraction characteristics than traditional metal gratings and are expected to fulfill the requirements of interferometers in gravitational-wave detection.*" [73] Against this background, in 2003 a joint project was started between the Universities of Hannover and Jena with the purpose to experimentally and theoretically investigate dielectric all-reflective interferometry concepts. Interferometers with dielectric beam splitters were demonstrated and 2-port and 3-port cavity couplers for potentially all-reflectively coupled arm resonators were investigated [50–53]. Improving simulation and etching techniques within the project have led to the resonant waveguide gratings as coating-free mirrors for interferometric applications [77, 78] and to a deeper understanding of how to design and manufacture dielectric gratings with respect to their requested diffraction efficiencies [79].

The dielectric gratings used in the experiments and reported in this work have a grating period of 1450 nm resulting in a second-order Littrow angle of $\beta_2 = 47.2\,^\circ$ for the used laser wavelength of 1064 nm. For the case of a grating having a period

in the order of the applied wavelength ($d \sim \lambda$) several computer based models exist to design and simulate the grating structures with respect to the power distributions into the diffraction orders. These models solve Maxwell's equations with appropriate boundary conditions and are generally referred to by the term 'rigorous methods'. For an example of an commercially available program, please see Ref. [80]. For a historical overview of the variety of methods and technical details the author refers to Ref. [76]. The used gratings were designed and manufactured by our project partners at the Institute of Applied Physics in Jena [81].

Since the gratings require a high reflectivity at normal incidence and at zeroth order diffraction, respectively, two different methods exist to apply the grating structure with respect to a highly reflective multilayer coating as shown in Fig. 2.3. For high efficiency gratings, the structure is written and etched into the top layer of a dielectric multilayer stack. This traditional technique was used to fabricate the dielectric gratings for high-power chirped-pulse amplification [82] or for the high efficiency 2-port couplers in [48]. This approach allows a separate design of grating structure and multilayer stack which minimizes the loss due to residual transmission. Since for low-efficiency gratings shallow grating structures are required, a different approach has been developed. In that the grating structure is directly etched into the substrate and then overcoated with the highly reflective multilayer coating. The advantage of this technique is that surface roughnesses and etching artifacts are flattened and that the deep grating structure gets washed out layer by layer until becoming a nearly flat mirror with a binary structure of some tens of nanometers [83]. The preliminary design of the structure with respect to the diffraction efficiencies obtained after the coating

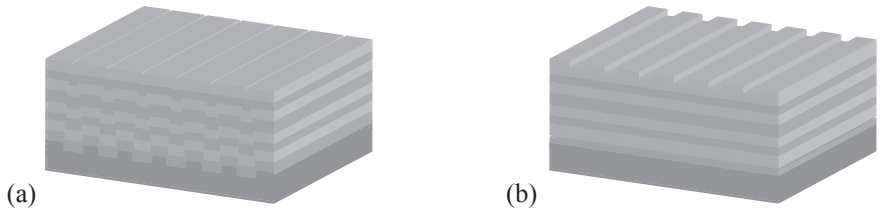

Figure 2.3.: Two design and fabrication methods of highly reflective dielectric gratings (a) Over coated grating-in-substrate structure. (b) Grating-on-top structure.

procedure has to account for this washing out of the structure [84]. Consequently such a volume grating requires much more complex simulation efforts and, furthermore, very precise knowledge of the coating and etching procedures [79].

Technically improved electron-beam writing instruments that avoid stitching artifacts by having larger writing ranges [85], and simultaneously improved etching techniques have led back to the grating-on-top design. Recently, dielectric 3-port gratings with a groove depths of 10-20 nm have been fabricated in Jena with diffraction efficiencies of below 0.1 % for the first diffraction order [86]. Figure 2.4 (a) shows one of the newly fabricated gratings, a one inch fused silica substrate with a binary 1450 nm grating structure written and etched in the top SiO_2 layer of a multilayer stack consisting of fused silica and tantala (Ta_2O_5). Current commercially available electron-beam lithography instruments allow to homogeneously process large substrates of up to an area $9'' \times 9''$ [87] as exemplarily shown in Fig. 2.4 (b).

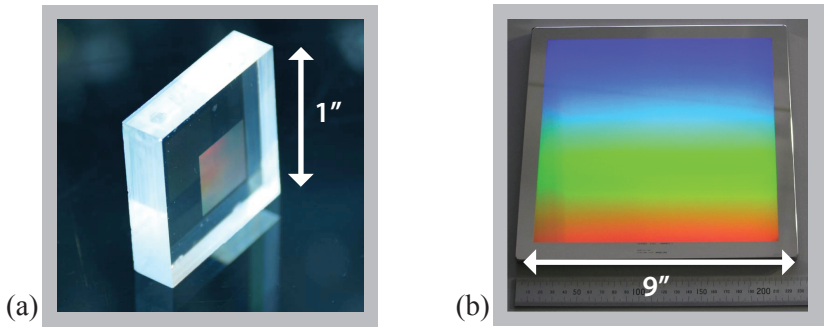

Figure 2.4.: (a) $1'' \times 1''$ fused silica substrate with grating-on-top structure. (b) $9'' \times 9''$ substrate with binary 1450 nm grating structure (spectral effects are from the applied chrome resist).

2.2. The scattering matrix formalism

The scattering matrix formalism provides the amplitude and phase relations of a light field between the input and output ports of an optical component. The component, having n input and output ports, is described by an $n \times n$ matrix that connects the complex amplitudes of an n-dimensional input vector $\mathbf{a}$ with the corresponding matrix

elements of an n-dimensional output vector $\mathbf{b}$.

$$\mathbf{b} = \mathbf{S} \times \mathbf{a} \tag{2.3}$$

Using the amplitude coefficients c_{ij} and the corresponding phases ϕ_{ij} for each matrix element, the most general notation [88] of a scattering matrix reads

$$\mathbf{S}_{n\times n} = \begin{pmatrix} c_{11}e^{\mathrm{i}\phi_{11}} & c_{12}e^{\mathrm{i}\phi_{12}} & \dots & c_{1n}e^{\mathrm{i}\phi_{1n}} \\ c_{21}e^{\mathrm{i}\phi_{21}} & c_{22}e^{\mathrm{i}\phi_{22}} & \dots & c_{2n}e^{\mathrm{i}\phi_{2n}} \\ \vdots & \vdots & \ddots & \vdots \\ c_{n1}e^{\mathrm{i}\phi_{n1}} & c_{n2}e^{\mathrm{i}\phi_{n2}} & \dots & c_{nn}e^{\mathrm{i}\phi_{nn}} \end{pmatrix}. \tag{2.4}$$

For a loss-less component conservation of energy implies

$$P_{\mathrm{out}} = \mathbf{b}^\dagger\mathbf{b} = (\mathbf{S}\mathbf{a})^\dagger(\mathbf{S}\mathbf{a}) = (\mathbf{a}^\dagger\mathbf{S}^\dagger)(\mathbf{S}\mathbf{a}) = \mathbf{a}^\dagger(\mathbf{S}^\dagger\mathbf{S})\mathbf{a} = P_{\mathrm{in}}, \tag{2.5}$$

with power P_{in} and P_{out} being the input and the output optical powers, respectively. Consequently, for a loss-less component unitarity must hold:

$$\mathbf{S}^\dagger\mathbf{S} = \mathbb{1}. \tag{2.6}$$

The reversibility of the optical path furthermore implies

$$|\mathbf{S}_{ij}| \;=\; |\mathbf{S}_{ji}|. \tag{2.7}$$

2.2.1. 2-port scattering matrix

A loss-less beam splitter or a (partially) transmissive mirror can be seen as an optical component with two ports (see Fig. 2.5). It is therefore described by a 2×2 scattering matrix. Each incoming light field is then split into two partial beams at a certain

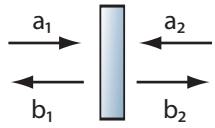

Figure 2.5.: Incoming fields a_i and reflected and transmitted fields b_i at a 2-port component.

amplitude reflectivity ρ and an amplitude transmission τ. Taking into account the Eqs. (2.6) and (2.7), the general scattering matrix can be written as

$$\mathbf{S}_{2\mathrm{p}} = \begin{pmatrix} \rho\, e^{\mathrm{i}\phi_{11}} & \tau\, e^{\mathrm{i}\phi_{12}} \\ \tau\, e^{\mathrm{i}\phi_{21}} & \rho\, e^{\mathrm{i}\phi_{22}} \end{pmatrix}. \tag{2.8}$$

From the unitarity of the scattering matrix $\mathbf{S}_{2\mathrm{p}}$, the following equations can be derived:

$$\rho^2 + \tau^2 = 1, \tag{2.9}$$
$$\rho\,\tau\,(e^{\mathrm{i}(\phi_{11}-\phi_{21})} + e^{\mathrm{i}(\phi_{12}-\phi_{22})}) = 0, \tag{2.10}$$
$$\rho\,\tau\,(e^{\mathrm{i}(\phi_{12}-\phi_{11})} + e^{\mathrm{i}(\phi_{22}-\phi_{21})}) = 0, \tag{2.11}$$

and consequently the conditions

$$(\phi_{12} - \phi_{11}) + (\phi_{21} - \phi_{22}) = \pm(2n+1)\pi, \tag{2.12}$$
$$(\phi_{11} - \phi_{21}) + (\phi_{12} - \phi_{22}) = \pm(2n+1)\pi, \tag{2.13}$$

have to be solved. One possibility is to choose the phases such that $\phi_{11} = \phi_{22} = 0$ and $\phi_{12} = \phi_{21} = \pi/2$. Thus, one description of the 2-port scattering matrix for a (partially) transmissive component can be written as

$$S_{2\mathrm{p}} = \begin{pmatrix} \rho & \mathrm{i}\tau \\ \mathrm{i}\tau & \rho \end{pmatrix}. \tag{2.14}$$

Another solution can be found by setting $\phi_{11} = \phi_{12} = \phi_{21} = 0$ and $\phi_{22} = \pi$, providing an alternative scattering matrix

$$S_{2\mathrm{p}} = \begin{pmatrix} \rho & \tau \\ \tau & -\rho \end{pmatrix}. \tag{2.15}$$

that is physically equivalent to Eq. (2.14) and also widely used in the literature [88]. Note that the phases are independently chosen with respect to the values of the transmission and reflection coefficients.

2.2.2. 3-port scattering matrix

The scattering matrix for a 3-port component can be derived in analogy to the 2-port component. Here, at each port three instead of two light fields are split and combined

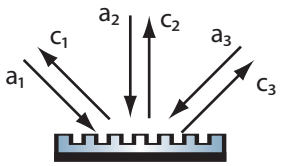

Figure 2.6.: Incoming fields a_i and outgoing fields c_i at a 3-port grating.

[89]. Consequently, it is a 3×3-matrix that connects the vector of the incoming fields a_i with the outgoing fields c_i (see Fig. 2.6). Since the 3-port gratings used in this work are binary gratings, $\eta_{-1} = \eta_1$ holds [see Fig. 2.7 (b)]. From Eq. (2.4), the general 3×3 scattering matrix can be written as

$$\mathbf{S}_{3\mathrm{p}} = \begin{pmatrix} \eta_2\, e^{\mathrm{i}\phi_{11}} & \eta_1\, e^{\mathrm{i}\phi_{12}} & \eta_0\, e^{\mathrm{i}\phi_{13}} \\ \eta_1\, e^{\mathrm{i}\phi_{21}} & \rho_0\, e^{\mathrm{i}\phi_{22}} & \eta_1\, e^{\mathrm{i}\phi_{23}} \\ \eta_0\, e^{\mathrm{i}\phi_{31}} & \eta_1\, e^{\mathrm{i}\phi_{32}} & \eta_2\, e^{\mathrm{i}\phi_{33}} \end{pmatrix}. \tag{2.16}$$

The amplitude coefficients η_0, η_1 and η_2 denote the diffraction efficiency of each diffraction order for a 3-port grating in second-order Littrow mount as shown in Fig. 2.7 (a). The coefficient ρ_0 denotes the amplitude reflectivity of the grating at normal incidence. Note that the restrictions made in Eq. (2.16) originate from the

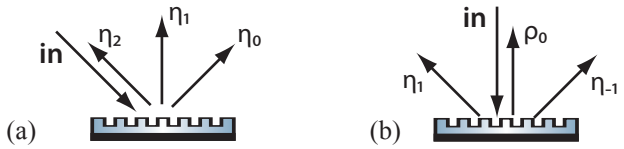

Figure 2.7.: Light incident onto a 3-port grating. (a) Second-order Littrow mount. (b) Normal incidence at 0°. Because of the symmetrical binary grating surface structure, $\eta_{-1} = \eta_1$ is valid.

symmetrical binary structure. The general representation of a 3-port scattering matrix that also holds for non-binary structures can be found in [51]. From the conservation of energy in Eq. (2.6) it follows that

$$\eta_0^2 + \eta_1^2 + \eta_2^2 = 1 \quad \text{and} \quad \rho_0^2 + 2\eta_1^2 = 1, \tag{2.17}$$

which is represented in Fig. 2.7. The assumption of the component being loss-less and the resulting unitarity of the scattering matrix lead to nine equations with thirteen

variables. They are reduced to eleven by applying the relations of Eq. (2.17). From the reciprocity of the device follows that the phase which the light picks up when diffracted into a certain order is independent from the input port [89]. Thus, the phase relations can be restricted as follows:

$$\phi_0 := \phi_{13} = \phi_{22} = \phi_{31}, \tag{2.18}$$

$$\phi_1 := \phi_{12} = \phi_{21} = \phi_{23} = \phi_{32}, \tag{2.19}$$

$$\phi_2 := \phi_{11} = \phi_{33}. \tag{2.20}$$

With these restrictions, the scattering matrix [89] can be written as

$$\mathbf{S}_{3\mathrm{p}} = \begin{pmatrix} \eta_2\, e^{\mathrm{i}\phi_2} & \eta_1\, e^{\mathrm{i}\phi_1} & \eta_0\, e^{\mathrm{i}\phi_0} \\ \eta_1\, e^{\mathrm{i}\phi_1} & \rho_0\, e^{\mathrm{i}\phi_0} & \eta_1\, e^{\mathrm{i}\phi_1} \\ \eta_0\, e^{\mathrm{i}\phi_0} & \eta_1\, e^{\mathrm{i}\phi_1} & \eta_2\, e^{\mathrm{i}\phi_2} \end{pmatrix}. \tag{2.21}$$

From the remaining system one possible set of phases can be calculated to

$$\phi_0 = 0, \tag{2.22}$$

$$\phi_1 = -\frac{1}{2}\arccos\left(\frac{\eta_1^2 - 2\eta_0^2}{2\rho_0\eta_0}\right), \tag{2.23}$$

$$\phi_2 = \arccos\left(\frac{-\eta_1^2}{2\eta_2\eta_0}\right), \tag{2.24}$$

which provides a full description of the loss-less binary-structured 3-port grating device. From Eqs. (2.21-2.24), fundamental characteristics of the grating can be deduced. The phases in Eqs. (2.23) and (2.24) explicitly depend on the diffraction efficiencies. This is in contrast to the phases derived for the 2-port component in the previous section where the phases did not dependent on the amplitude coefficients ρ and τ. When designing a 3-port grating with a certain first-order efficiency η_1 that acts as the coupling efficiency to an optical resonator, $\rho_0^2 + 2\eta_1^2 = 1$ determines the reflectivity at normal incidence ρ_0. Since the arcos in Eqs. (2.23) and (2.24) allow only arguments between -1 and +1, fundamental minimal and maximal boundary values for zeroth-order and second-order diffraction efficiencies $\eta_{0^{\mathrm{min}}_{\mathrm{max}}}$ and $\eta_{2^{\mathrm{min}}_{\mathrm{max}}}$ can be found [89],

$$\frac{1-\rho_0}{2} \leq \eta_0 \leq \frac{1+\rho_0}{2} \quad \text{and} \quad \eta_2^2 = 1 - (\eta_1^2 + \eta_0^2), \tag{2.25}$$

and accordingly

$$\frac{1-\rho_0}{2} \leq \eta_2 \leq \frac{1+\rho_0}{2} \quad \text{and} \quad \eta_0^2 = 1 - (\eta_1^2 + \eta_2^2). \tag{2.26}$$

In Fig. 2.8, the phases of Eqs. (2.19) and (2.20) are shown. The first-order diffraction efficiency is exemplarily chosen to $\eta_1^2 = 5\,\%$ and the other efficiencies and the amplitude reflectivity are correspondingly defined by Eqs. (2.26) and (2.17). The corresponding boundary values are $\eta_{2\mathrm{min}} = 0.02566$ and $\eta_{2\mathrm{max}} = 0.97434$. The phase shift of the first-order diffraction ϕ_1 increases linearly with the second-order diffraction efficiency. Close to the maximal boundary value the phase shift changes drastically. The phase relation of the second diffraction order ϕ_2 is sensitive to very small deviations from the two boundary values $\eta_{2\mathrm{min}}$ and $\eta_{2\mathrm{max}}$, respectively. The steep phase gradients that depend on the diffraction efficiencies have an impact on the input/output as well as on the signal transfer characteristics of a 3-port-grating coupled cavity (see Section 2.3.2). In this case light fields that are coupled out of the cavity interfere with the diffracted parts of the incident field. Hence, the interference of incoming and outgoing light fields depends on their relative phase. Moreover, the phase characteristics

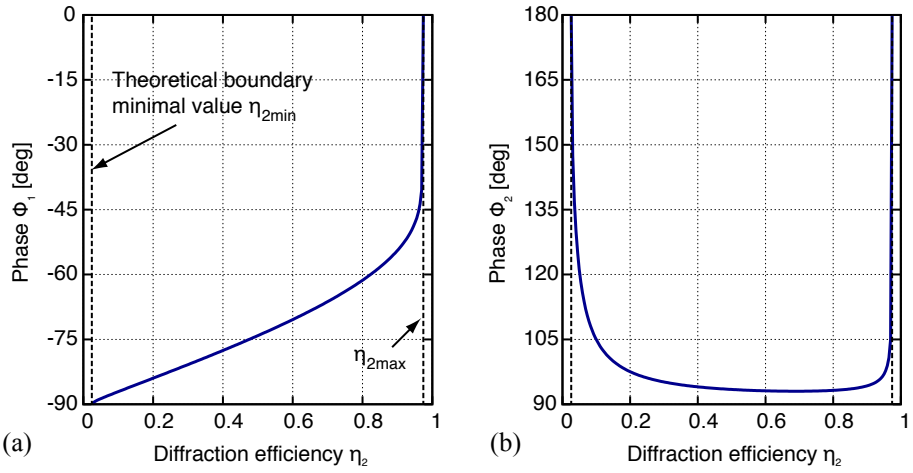

Figure 2.8.: Phases ϕ_1 and ϕ_2 as a function of the second-order amplitude diffraction efficiency η_2. The phase for the zeroth-order is chosen $\phi_0 = 0$. The first-order power efficiency is chosen to $\eta_1^2 = 5\,\%$. The corresponding boundary values are $\eta_{2\mathrm{min}} = 0.02566$ and $\eta_{2\mathrm{max}} = 0.97434$, respectively. (a) First-order phase ϕ_1. (b) Second-order phase ϕ_2.

as a function of η_2 that is shown in Fig. 2.8 (b) illustrates that even small deviations from the boundary values of the diffraction efficiencies have an impact on the optical characteristics of the grating.

2.3. Optical resonators

In the following the scattering matrices derived in the previous section are used to describe the input and output characteristics of optical resonators. The characteristics of a linear Fabry-Pérot cavity and a 3-port-grating coupled cavity are compared. Coupled optical cavities are routinely used in gravitational wave detectors. The theoretical description of two cavities coupled with a 3-port grating is derived and the grating cavity characteristics are exemplarily shown in an experiment.

2.3.1. Linear Fabry-Pérot resonator

The linear Fabry-Pérot resonator is an optical cavity consisting of two mirrors M_i with the corresponding amplitude reflection coefficients ρ_i and transmission coefficients τ_i. The mirrors are placed orthogonal to the optical light path at distance L (being the cavity length) as shown in Fig. 2.9. Note that the geometrical characteristics of the light field are not considered by this approach.

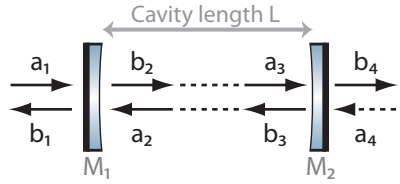

Figure 2.9.: Input and output amplitudes at a transmissively coupled linear Fabry-Pérot resonator having the length L.

The scattering matrix of the mirrors $\mathbf{M}_i$ and the propagation matrix $\mathbf{L}$,

$$\mathbf{M}_i = \begin{pmatrix} \rho_i & \mathrm{i}\tau_i \\ \mathrm{i}\tau_i & \rho_i \end{pmatrix} \quad \text{and} \quad \mathbf{L} = \begin{pmatrix} 0 & e^{\mathrm{i}kL} \\ e^{\mathrm{i}kL} & 0 \end{pmatrix}, \tag{2.27}$$

connect the input and output amplitudes of the light field [88]. The $\mathbf{L}$ describes the propagation of the light field along the cavity length L which affects only the phase

of the propagating light. Here, $k = \omega/c$ holds, with $\omega = 2\pi f$ being the angular frequency of the laser light and c the speed of light. The input and output amplitudes are connected according to

$$\begin{pmatrix} b_1 \\ b_2 \end{pmatrix} = \begin{pmatrix} \rho_1 & \mathrm{i}\tau_1 \\ \mathrm{i}\tau_1 & \rho_1 \end{pmatrix} \begin{pmatrix} a_1 \\ a_2 \end{pmatrix} \tag{2.28}$$

$$\begin{pmatrix} a_2 \\ a_3 \end{pmatrix} = \begin{pmatrix} 0 & e^{\mathrm{i}kL} \\ e^{\mathrm{i}kL} & 0 \end{pmatrix} \begin{pmatrix} b_2 \\ b_3 \end{pmatrix} \tag{2.29}$$

$$\begin{pmatrix} b_3 \\ b_4 \end{pmatrix} = \begin{pmatrix} \rho_2 & \mathrm{i}\tau_2 \\ \mathrm{i}\tau_2 & \rho_2 \end{pmatrix} \begin{pmatrix} a_3 \\ a_4 \end{pmatrix}. \tag{2.30}$$

For the case that light is incident to the system from only one side ($a_4 = 0$, the amplitude of the incoming light field is denoted as a_{in}), the amplitudes of the input and output ports of the optical components are derived as follows:

$$\begin{aligned} a_1 &= a_{\mathrm{in}}, \\ a_2 &= a_{\mathrm{in}}\rho_2\tau_1 e^{2\mathrm{i}kL}d, \\ a_3 &= a_{\mathrm{in}}\mathrm{i}\tau_1 e^{\mathrm{i}kL}d, \\ a_4 &= 0, \\ b_1 &= a_{\mathrm{in}}\left[\rho_1 - \rho_2\left(\rho_1^2 + \tau_1^2\right)e^{2\mathrm{i}kL}\right]d, \\ b_2 &= a_{\mathrm{in}}\mathrm{i}\tau_1 d, \\ b_3 &= a_{\mathrm{in}}\rho_2\tau_1 e^{\mathrm{i}kL}d, \\ b_4 &= -a_{\mathrm{in}}\tau_1\tau_2 e^{\mathrm{i}kL}d. \end{aligned} \tag{2.31}$$

The abbreviation d denotes the resonance factor of the cavity,

$$d = \frac{1}{1 - \rho_1\rho_2 e^{\mathrm{i}2\Phi}}, \tag{2.32}$$

where $\Phi = kL = \omega L/c$ is the detuning parameter of the cavity that describes its optical length. It assumes the minimal value (anti-resonance) for $\Phi = \pi/2$ and the

maximal value on resonance for $\Phi = 0$, respectively. Therewith, the equations for amplitude transmission and reflection coefficient of the linear Fabry-Pérot cavity [90] are given by

$$t_{\mathrm{FP}} = \frac{b_4}{a_{\mathrm{in}}} = \frac{-\tau_1\tau_2 e^{\mathrm{i}\Phi}}{1-\rho_1\rho_2 e^{\mathrm{i}2\Phi}}, \tag{2.33}$$

$$r_{\mathrm{FP}} = \frac{b_1}{a_{\mathrm{in}}} = \frac{\rho_1 - \rho_2\left(\rho_1^2+\tau_1^2\right)e^{\mathrm{i}2\Phi}}{1-\rho_1\rho_2 e^{\mathrm{i}2\Phi}}. \tag{2.34}$$

If the two mirrors have no loss [see Eq. (2.9)] and equal reflectivities, the simplified reflection coefficient of such a linear Fabry-Pérot resonator is given by

$$r_{\mathrm{FP}} = \frac{\rho(1-e^{i\Phi})}{1-\rho^2 e^{i\Phi}}. \tag{2.35}$$

The case where the incoupling efficiency equals the outcoupling efficiency, including roundtrip loss, is called "impedance matched". For a loss-less scenario [see Eq. 2.35], on resonance no light is reflected from the resonator and thus all light is transmitted. Note that in the following a perfect match of the mode of the input field to the eigenmode of the cavity is assumed, in the following referred to as "mode-matching".

Fig. 2.10 shows the power transmittance t_{FP}^2 and power reflectivity r_{FP}^2 of a linear cavity as a function of the transmission τ_2^2 of the second mirror. The input transmission of the first mirror was chosen to be $\tau_1^2 = 3.3\,\%$. For equal mirror transmission values the cavity transmittance reaches unity and the impedance matched case is realized. If the input transmission is higher than the transmission of the end mirror the cavity is called *over-coupled*. The scenario where the input transmission is smaller than the transmission of the end mirror and/or the amount of light power that is lost due to roundtrip loss, is called *under-coupled*.

The amplitude b_2 from Eqs. (2.31) describes the maximal power build-up on resonance. In this case ($\Phi = 0$), the build-up depends on the transmission coefficient of the input mirror and the reflection coefficients of the two mirrors. It can be written as

$$\left|\frac{b_2}{a_{\mathrm{in}}}\right|^2 = \frac{\tau_1^2}{\left(1-\rho_1\rho_2\right)^2}. \tag{2.36}$$

In Fig. 2.10 the intra-cavity field as a function of the end mirror transmission coefficient is shown, too. The intra-cavity power build-up decreases with a decreasing

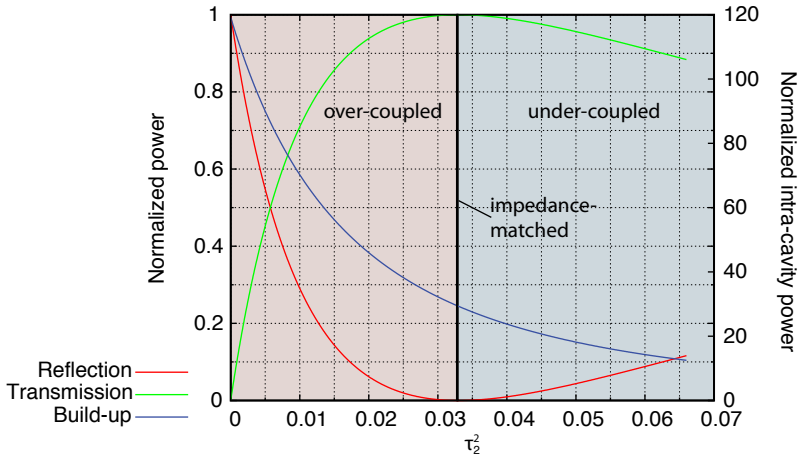

Figure 2.10.: Intra-cavity field, power transmittance and power reflection at a loss-less linear Fabry-Pérot cavity. The input transmissivity of the coupling mirror is chosen to $\tau_1^2 = 3.3\,\%$. If the transmission at the end mirror is smaller than the input, the cavity is called *over-coupled*, a higher transmission is called *under-coupled*, and for the case of equal input and output coefficients (including loss) all light is transmitted through the cavity (impedance matched case).

transmission of the end mirror. Thus, with two mirrors having different transmission and reflection coefficients two different cavities can be realized with respect to the achievable power build-up on resonance. Depending on the configuration of the mirrors these are the over-coupled configuration with high power build-up and the under-coupled cavity with a lower build-up, respectively.

In Fig. 2.11 shows the power transmittance of a loss-less impedance matched optical resonator as a function of the cavity detuning. Two characteristic quantities of such a cavity are illustrated. The so-called *free-spectral-range* (FSR) is defined as the distance between two resonance peaks. The FSR-value depends on the length L of the resonator and is given by

$$\mathrm{FSR} = \frac{c}{2L}. \tag{2.37}$$

The width of the resonance peak at which the intensity has decreased to the half of its maximum is called *full width at half maximum* (FWHM, see Fig. 2.11). The ratio of FSR and FWHM is the so-called finesse as another quantity of an optical resonator,

$$\mathcal{F} = \frac{\mathrm{FSR}}{\mathrm{FWHM}}. \tag{2.38}$$

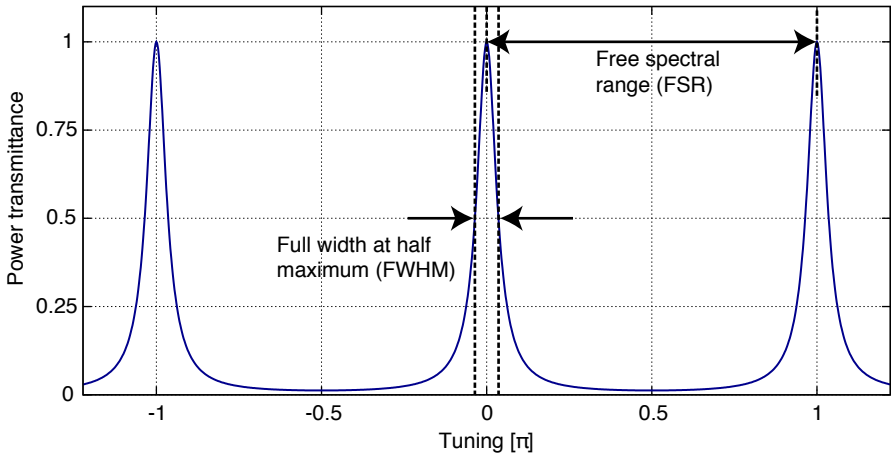

Figure 2.11.: Power transmittance of a linear Fabry-Pérot cavity as a function of the cavity detuning. Characteristic quantities of the resonators are the *free spectral range* (FSR) and the linewidth or *full width at half maximum* (FWHM).

The finesse depends only on the reflection coefficients of the optical components. It can be compared to the Q-factor of mechanical and electrical (LC-)oscillators and is given by

$$\mathcal{F} = \frac{\pi}{2\arcsin\left(\frac{1-\rho_1\rho_2}{2\sqrt{\rho_1\rho_2}}\right)} \approx \frac{\pi\sqrt{\rho_1\rho_2}}{1-\rho_1\rho_2}. \tag{2.39}$$

For the most common cases of rather high reflection coefficients (τ_1, $\tau_2 \ll 1$ and ρ_1, $\rho_2 \approx 1$), the right hand approximation in Eq. (2.39) can be used. For a more detailed analysis of optical resonators, see [88, 90].

2.3.2. 3-port-grating coupled cavity

General description

The dielectric 3-port grating, used in the second-order Littrow configuration, can be employed as the coupling component to an optical cavity as shown in Fig. 2.12. A highly reflective end mirror of the cavity is placed parallel to the grating surface. The intra-cavity power build-up that is maximally achievable is a function of the first-order diffraction efficiency of the grating and of the reflectivity of the end mirror. The

diffraction efficiency η_1 is comparable to the coupling efficiency τ_1 of the coupling mirror of a linear Fabry-Pérot cavity. According to Eq. (2.17) a small input efficiency leads to a high reflectivity and a high finesse value. Furthermore, the three output ports of the cavity – forward-reflection, retro-reflection and transmission at the end mirror – are correlated; firstly, by the detuning of the cavity, secondly, by the diffraction efficiencies of the grating itself [89].

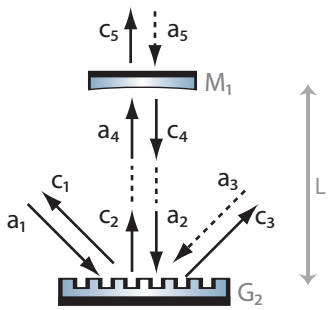

Figure 2.12.: Scheme of the input and output amplitudes of a 3-port-grating coupled cavity of the length L.

In analogy to the linear cavity, this cavity can be described by the scattering matrix of the mirror, the propagation matrix, and the scattering matrix of the grating with the diffraction efficiencies η_0, η_1 and η_2, the reflection coefficient ρ_0 and the phases given in Eqs. (2.22), (2.23) and (2.24):

$$\begin{pmatrix} c_1 \\ c_2 \\ c_3 \end{pmatrix} = \begin{pmatrix} \eta_2\, e^{\mathrm{i}\phi_2} & \eta_1\, e^{\mathrm{i}\phi_1} & \eta_0\, e^{\mathrm{i}\phi_0} \\ \eta_1\, e^{\mathrm{i}\phi_1} & \rho_0\, e^{\mathrm{i}\phi_0} & \eta_1\, e^{\mathrm{i}\phi_1} \\ \eta_0\, e^{\mathrm{i}\phi_0} & \eta_1\, e^{\mathrm{i}\phi_1} & \eta_2\, e^{\mathrm{i}\phi_2} \end{pmatrix} \begin{pmatrix} a_1 \\ a_2 \\ a_3 \end{pmatrix}, \tag{2.40}$$

$$\begin{pmatrix} a_2 \\ a_4 \end{pmatrix} = \begin{pmatrix} 0 & e^{\mathrm{i}kL} \\ e^{\mathrm{i}kL} & 0 \end{pmatrix} \begin{pmatrix} c_2 \\ c_4 \end{pmatrix}, \tag{2.41}$$

$$\begin{pmatrix} c_4 \\ c_5 \end{pmatrix} = \begin{pmatrix} \rho_1 & \mathrm{i}\tau_1 \\ \mathrm{i}\tau_1 & \rho_1 \end{pmatrix} \begin{pmatrix} a_4 \\ a_5 \end{pmatrix}. \tag{2.42}$$

Since light is coupled into the cavity only at port a_1, $a_3 = a_5 = 0$ and $a_1 = a_{\mathrm{in}}$ are valid (see Fig. 2.12). The scattering formalism yields the following amplitudes at the

grating ports:

$$\begin{aligned}
a_1 &= a_{\mathrm{in}}, \\
a_2 &= a_{\mathrm{in}}\rho_1\eta_1 e^{\mathrm{i}(\phi_1+2\Phi)}d, \\
a_3 &= 0, \\
a_4 &= a_{\mathrm{in}}\eta_1 e^{\mathrm{i}(\phi_1+\Phi)}d, \\
a_5 &= 0, \\
c_1 &= a_{\mathrm{in}}(\eta_2 e^{\mathrm{i}\phi_2} + \eta_1^2\rho_1 e^{\mathrm{i}[2(\phi_1+\Phi)]}d), \\
c_2 &= a_{\mathrm{in}}\eta_1 e^{\mathrm{i}\phi_1}d, \\
c_3 &= a_{\mathrm{in}}(\eta_0 + \eta_1^2\rho_1 e^{\mathrm{i}[2(\phi_1+\Phi)]}d), \\
c_4 &= a_{\mathrm{in}}\rho_1\eta_1 e^{\mathrm{i}(\phi_1+\Phi)}d, \\
c_5 &= a_{\mathrm{in}}\mathrm{i}\tau_1\eta_1 e^{\mathrm{i}(\phi_1+\Phi)}d.
\end{aligned} \tag{2.43}$$

For a normalized input field ($a_{\mathrm{in}} = 1$) the amplitude reflection coefficients of the back-reflected field c_1, the forward-reflected field c_3 as well as the amplitudes of the intra-cavity field c_2 and the transmitted field t can be derived to

$$c_1 = \eta_2 e^{\mathrm{i}\phi_2} + \eta_1^2\rho_1 e^{\mathrm{i}[2(\phi_1+\Phi)]}d, \tag{2.44}$$

$$c_2 = \eta_1 e^{\mathrm{i}\phi_1}d, \tag{2.45}$$

$$c_3 = \eta_0 + \eta_1^2\rho_1 e^{\mathrm{i}[2(\phi_1+\Phi)]}d, \tag{2.46}$$

$$t = \mathrm{i}\tau_1 e^{\mathrm{i}\Phi}\, c_2. \tag{2.47}$$

In analogy to the linear cavity the resonance factor is given by

$$d = [1 - \rho_0\rho_1 e^{\mathrm{i}2\Phi}]^{-1} \tag{2.48}$$

with the detuning parameter $\Phi = \omega L/c$.

Light fields at the 3-port-grating coupled cavity

As mentioned above the three output ports C1, C2 and T are correlated – firstly because of the detuning of the resonator, secondly because of the transmission of the end

mirror and any other cavity loss, and thirdly because of the grating parameters, such as its diffraction efficiencies and the grating surface structure. In the following, the output characteristics of 3-port-grating coupled resonators as a function of the grating's diffraction efficiencies, the detuning and the loss are analyzed. The output ports of the resonator are named as shown in Fig. 2.13.

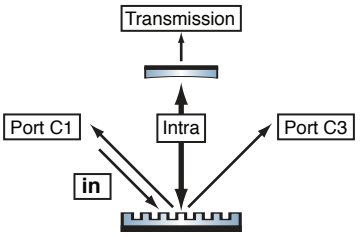

Figure 2.13.: Labeling of the ports of a 3-port-grating coupled cavity. Port C1 denotes the back-reflected port, Port C3 denotes the forward-reflected port, and Port T denotes the transmission at the end mirror. The term Intra denotes the intra-cavity field.

In Fig. 2.14 the output characteristics of a 3-port grating mounted in second-order Littrow for three different gratings are shown as a function of the cavity detuning. The cavity input efficiency is always chosen to be $\eta_1^2 = 10\,\%$, the end mirror is assumed to have a perfect reflectivity ($\rho_1^2 = 1$), and optical loss is neglected. The output at the backward-reflected port C1 consists of two interfering fields which are the fields of the second diffraction order and the light field that is coupled out of the cavity. At the forward-reflected port C3 the two interfering light fields are the incident field that is forward reflected via the zeroth diffraction order and the light that is coupled out of the cavity towards this port. Figure 2.14 shows the borderline cases for a grating design according to Eqs. (2.25) and (2.26), which are the minimal value of the second-order diffraction efficiency (and the maximal zeroth order efficiency, respectively) and the maximal second-order efficiency (and the minimal zeroth order efficiency, respectively). Additionally the case where the two efficiencies are equal ($\eta_0 = \eta_2 = \eta_{0/2\mathrm{mid}}$) is shown.

In the case that the second-order diffraction efficiency is minimal because of the interference effects, the forward-reflected port becomes totally dark while on resonance all light is back-reflected to the laser light source [Fig. 2.14 (a)]. This case can be seen as the opposite of the linear loss-less impedance-matched Fabry-Pérot resonator

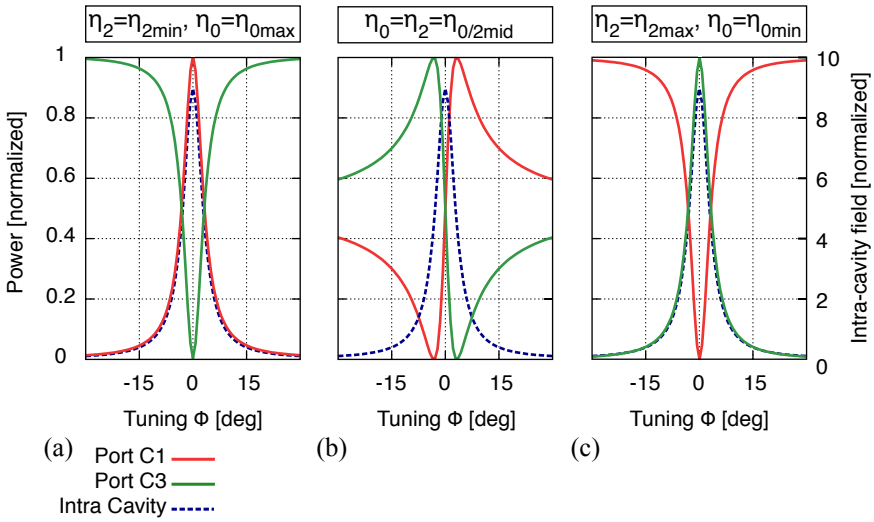

Figure 2.14.: Output at the ports C1 and C3, and the intra-cavity field as a function of the cavity detuning Φ and an input of $\eta_1^2 = 10\,\%$, no loss and an assumably perfect end mirror reflectivity. (a) $\eta_{2\mathrm{min}}$-grating: On resonance all light is back-reflected at port C1 and the forward-reflected port C3 becomes dark. (b) $\eta_{2\mathrm{mid}}$-grating: strongly asymmetric resonance profiles at the two output ports. Their maxima do not match with the maximum power build-up inside the cavity. (c) $\eta_{2\mathrm{max}}$-grating: On resonance the forward-reflected port C3 becomes bright while no resonant light is back-reflected at port C1. The resonance profile of the intra-cavity field is independent from the ratio of the zeroth and second diffraction efficiency.

(see Fig. 2.10), where on resonance the transmission port becomes bright. Thus, this 3-port-grating cavity scenario can be seen as a resonant reflector of the laser light that is coupled to the cavity. The other extremal value of the second diffraction order is its maximal value $\eta_{2\mathrm{max}}$, the characteristics are shown in Fig. 2.14 (c). Here, the forward-reflected port C3 becomes bright on resonance, while no light is back-reflected to the source at port C1. As a third situation, the case where the two diffraction efficiencies are equal is shown in Fig. 2.14 (b). A strong asymmetry in the resonance profiles of the two ports occurs with respect to the symmetrical intra-cavity resonance (blue dashed line in Fig. 2.14).

On resonance, one half of the incoming light is back-reflected at port C1 and the other half is forward-reflected at port C3. Note that independently from the relation of zeroth and second diffraction efficiency the distribution of spectral profile of the intra-

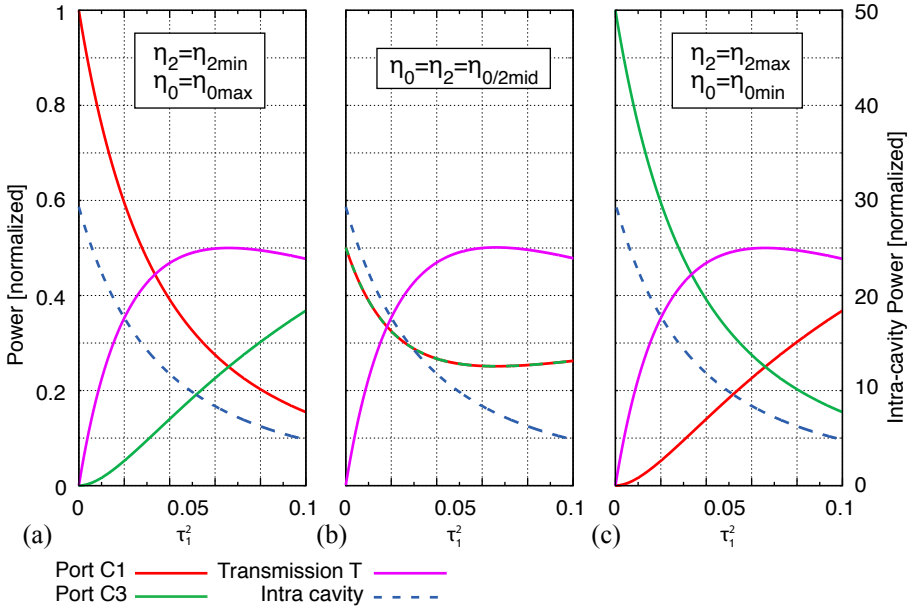

Figure 2.15.: Output fields at the ports C1 and C3, in transmission of the end mirror and the intra-cavity field for three different grating configurations as a function of the end mirror transmission τ_1^2. The input efficiency is chosen to be $\eta_1^2 = 3.3\,\%$. The cavity is on resonance ($\Phi = 0$). In the case of $\tau_1^2 = 2\eta_1^2 = 6.6\,\%$, the maximal transmittance ($t^2 = 0.5$) is realized and the other half of the outcoupled light splits equally into the forward- and backward-reflected port; independently from the grating configuration. (a) Grating with $\eta_{2\mathrm{min}}$. (b) Grating with $\eta_{2\mathrm{mid}}$. The outputs at ports C1 and C3 equal independently from the roundtrip loss. (c) Grating with $\eta_{2\mathrm{max}}$. The characteristics at the ports show exactly the opposite behavior than in the $\eta_{2\mathrm{min}}$-case.

cavity field shows an identical behavior due to the unaffected cavity input efficiency of the first diffraction order. Thus, the three examples in Fig. 2.14 represent three cavities with different output characteristics but identical linewidth, free-spectral-range, and finesse.

The constructive and destructive interference effects at the ports C1 and C3 are significantly affected when the cavity end mirror no longer has perfect reflectivity. This case is illustrated for cavities on resonance in Fig 2.15, again for the three different grating configurations $\eta_{2\mathrm{min}}$, $\eta_{2\mathrm{max}}$, and $\eta_{2\mathrm{mid}}$. The coupling efficiency is chosen to be $\eta_1^2 = 3.3\,\%$. Consequently, the maximal power build-up (and the finesse) are

higher than in Fig. 2.14. As seen in Fig. 2.14 the characteristics of the intra-cavity field is not affected by relation of the grating's zeroth- and second-order diffraction efficiencies. Thus the characteristic of the intra-cavity field and the transmission show equal behavior for all three cases. The case where $\rho_0^2 = \rho_1^2$ (and $2\eta_1^2 = \tau_1^2$) realizes the maximal power transmission of $t^2 = 0.5$ at the end mirror according to Eq. (2.47). At this point independently from the grating's configuration the other half of the resonant light splits equally into the forward- and the backward-reflected ports. Note that the transmission of the end mirror can be regarded just as loss of the grating cavity. Hence, when using a 3-port grating with minimal second-order diffraction efficiency and aiming for an optimal reflectivity on resonance, any roundtrip loss or residual transmissions of the end mirror or the grating will decrease the maximal reflectivity on resonance.

2.3.3. Two cavities coupled with a 3-port grating

In the previous sections, the optical properties of 3-port grating resonators were theoretically derived and investigated. In the following, the theoretical 3-port cavity description discussed in Sec. 2.3.2 is extended for the case of two cavities that are coupled with a 3-port grating. Then, the theory is experimentally verified. The results that were obtained in the investigation presented here are strongly related to the experimental chapters of this thesis. Two coupled cavities can be seen as a Fabry-Pérot arm resonator coupled to the power-recycling resonator of an interferometer. In current interferometer layouts this concept is used to provide very high light power build-ups inside the arms. Figure 2.16 (a) shows such an interferometer layout with transmissively coupled optical cavities [91, 92]. Therefore, the applicability of this technology based on all-reflective optics is an important requirement for advanced all-reflective interferometers. The power-recycling-technique summarized in the following is an important add-on technology for the Michelson-type interferometer with diffractively coupled arm resonators that is discussed in Chap. 3. The second experimental investigation that is presented in Chap. 4 of this thesis is a laser diode with optical feedback from an external 3-port grating coupled cavity. Such a system can be seen as two coupled cavities with the incoupling mirror (or the power-recycling mirror, respectively) replaced by the semiconductor laser diode. The theoretical investigation as well as the

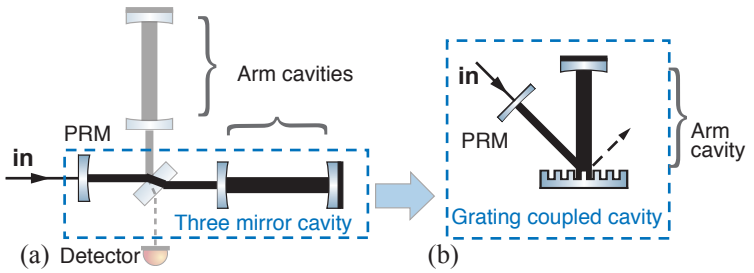

Figure 2.16.: (a) In an interferometric GW detector, the arm cavity and the power-recycling cavity formed by the power-recycling mirror (PRM) and the arm cavity coupling mirror, form two coupled cavities where the partially transmissive arm cavity coupling mirror is exposed to high thermal load. (b) This transmissive coupling mirror can be replaced by an all-reflective 3-port grating. Source: see Ref. [93].

experimental results are part of the PhD thesis by O. Burmeister [51]. Because of their significance in relation to the experiments presented in this work, they are summarized in the following. The detailed theoretical description was presented by Burmeister *et al.* [93]. The experimental results of this section have been published by Britzger *et al.* [94].

In the following, the all-reflective coupling of a Fabry-Pérot resonator with a power-recycling resonator is experimentally demonstrated. The coupling component is a custom-made dielectric low-efficiency 3-port diffraction grating. Based on the theoretical analysis in [93] and the experimentally determined diffraction efficiencies and losses of the grating, the light powers at all three output ports of the coupled cavity system are simulated in dependence of the cavity detunings. The experimental observations show a qualitative agreement with the theoretical model.

Theoretical description

Figure 2.17 (a) shows a 3-port grating mounted in second-order Littrow configuration and a grating cavity with a small first-order diffraction efficiency as the coupling efficiency to the cavity [see Fig. 2.17 (b)]. Independently from the grating's specific diffraction efficiencies the implementation of an additional power-recycling mirror (PRM) with the amplitude coefficients ρ_{PR} and τ_{PR} between the laser source and the grating forms two coupled resonators [see Fig. 2.17 (c)]. In analogy to Michelson-type

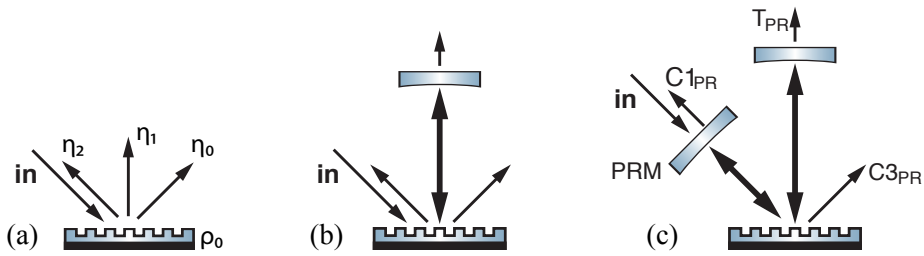

Figure 2.17.: (a) 3-port grating in second-order Littrow mount. The amplitude diffraction efficiencies are denoted η_n and the reflectivity under normal incidence ρ_0, respectively. (b) By inserting a mirror perpendicularly to the grating, a 3-port-grating cavity is created. (c) Inserting the power-recycling mirror PRM in the entrance, a power-recycled 3-port-grating coupled cavity is formed. The output ports are denoted $\mathrm{C1_{PR}}$, $\mathrm{C3_{PR}}$ and $\mathrm{T_{PR}}$.

gravitational wave detectors in the following we will denote the first cavity, formed by the PR mirror and the grating, as the power-recycling cavity (PR cavity), and the second cavity, formed by the grating and the end mirror, as the arm cavity. For such a system the amplitude reflection coefficients for the back-reflected field $c_{1\mathrm{PR}}$, the forward-reflected field $c_{3\mathrm{PR}}$, the intra-cavity field of the arm cavity $c_{2\mathrm{PR}}$ and the transmitted field t_{PR} are

$$c_{1\mathrm{PR}} = [\rho_1 - c_1 \exp(\mathrm{i}2\Phi_1)]d_1, \tag{2.49}$$

$$c_{2\mathrm{PR}} = \mathrm{i}\tau_{\mathrm{PR}} \exp[\mathrm{i}(\Phi_1 + \Phi_2)]c_2 d_1, \tag{2.50}$$

$$c_{3\mathrm{PR}} = \mathrm{i}\tau_{\mathrm{PR}} \exp(\mathrm{i}\Phi_1)c_3 d_1, \tag{2.51}$$

$$t_{\mathrm{PR}} = -\tau_{\mathrm{PR}}\tau_1 \exp[\mathrm{i}(\Phi_1 + \Phi_2)]c_2 d_1, \tag{2.52}$$

where c_n are the amplitude reflection coefficients of the 3-port-grating cavity given in Eqs. (2.44), (2.45), and (2.46) and discussed above. The resonance factor of the PR cavity is given by $d_1 = [1 - \rho_{\mathrm{PR}} c_1 \exp(\mathrm{i}2\Phi_1)]^{-1}$, and the length L_1 of the PR cavity is expressed by the detuning parameter $\Phi_1 = \omega L_1/c$. Correspondingly, the length of the second cavity L_2, which is the 3-port-grating cavity, is expressed by the detuning parameter $\Phi_2 = \omega L_2/c$. A more detailed deduction and the theoretical investigation of the system can be found in [93].

In current gravitational wave detectors the arm cavities are standing-wave cavities with an amplitude reflectivity of the end mirror of $\rho_1 \approx 1$. Such a cavity always

reflects the light back into the PR resonator, independently from the detuning of the cavity. This is different for a 3-port-grating coupled cavity with the additional port C3 as discussed in Section 2.3.2. The light fields that are back-reflected from the grating cavity and thus recoupled to the PR cavity firstly depend on the grating-specific diffraction efficiencies and, secondly, on the detuning of the grating cavity. Note that the light amplitude c_1 [given in Eq. (2.44)] that is reflected from the grating cavity c_1, can be seen as the compound component reflectivity $\rho_{\mathrm{c}}(\Phi_2)$ of the grating and the end mirror [93]. In consequence the overall power build-up inside both cavities finally depends on the detuning of the PR cavity Φ_1 and the detuning of the arm cavity Φ_2. The additional third port C3$_{\mathrm{PR}}$ is a loss channel showing a characteristic behavior that is presented and discussed in the following experiment.

Exemplary experimental configuration

Exemplary setup parameters For the experimental realization presented in [94] a dielectric 3-port grating with close to minimal second-order diffraction efficiency was designed and fabricated in Jena [95]. The grating had a period of 1450 nm. This provided a second-order Littrow angle of $\alpha_{\mathrm{in}} = 47.2^{\circ}$ and a first-order diffraction angle of $\theta_{\mathrm{out}} = 0^{\circ}$ at the laser wavelength of 1064 nm.

The experimental layout was chosen accordingly to the setup that is sketched in Fig. 2.17 (c). The grating cavity had a length of $L_2 = 81.5\,\mathrm{cm}$. The high-reflectivity end mirror had a transmissivity of $\tau_1^2 = 7\,\mathrm{ppm}$ and a radius of curvature of $R_{\mathrm{c}} = 100.0\,\mathrm{cm}$. The PR cavity had a length of $L_1 = 49.5\,\mathrm{cm}$. The (astigmatic) PR mirror had two different radii of curvature in horizontal and vertical direction such that they matched the wavefront curvatures at the mirror's position. The PR mirror had a dielectric multilayer system providing a reflectivity of $\rho_{\mathrm{PR}}^2 = 0.96$. The PR mirror as well as the end mirror were mounted onto piezo-electrical transducers (PZT) to linearly sweep the cavity lengths. Cylindrical lenses were employed to generate the elliptical beam profile that was needed in order to mode-match the incoming beam to the eigenmode of the recycling cavity (see Sec. 3.2.1). Initially, the grating was characterized via a finesse measurement using the setup discussed in [48]. The diffraction efficiencies of the grating for s-polarized light were found to be $\eta_0^2 = 0.927(\pm 0.045)\,\%$, $\eta_1^2 = 0.0591(\pm 0.003)\,\%$ and $\eta_2^2 = 0.0001(\pm 50)\,\mathrm{ppm}$ and the reflectivity of the

grating for normal incidence was $\rho_0^2 = 0.879(\pm 0.003)\,\%$. The total optical loss of the grating due to scattering, absorption and residual transmission was determined to $A = 0.0027(\pm 0.0061)\,\%$. The grating transmission was independently measured and was found to be $\tau_0^2 = 123\,\mathrm{ppm}$. The light transmitted through the grating was used to monitor the power inside the arm cavity with a photodetector ($\mathrm{PD_{GT}}$). To monitor the output characteristics of the system a photodetector was placed in port $\mathrm{C3_{PR}}$. A third photodetector was placed in reflection of the system using a 50:50 beam splitter in the input path for monitoring the reflection port $\mathrm{C1_{PR}}$ [see Fig. 2.17 (c)]. For a more detailed information about the setup, and the obtained results, see Ref. [94].

Power-recycling and cavity detunings The light power inside the arm cavity and at the two output ports of the coupled cavity system was measured versus the detunings of the arm cavity and the PR cavity, respectively. The obtained results are compared with a simulation that is based on the measured grating diffraction efficiencies, the mirror reflectivities and the optical loss of the components obtained in the characterization process [51].

Generally, the state of the coupled optical system depends on the detuning Φ_1 and Φ_2 of the two cavities. Therefore the results of the model are presented as three-dimensional plots showing light powers versus detunings [93]. However, in the measurement the detunings were not stabilized to certain points of the phase space but swept by applying sinusoidal voltages to the PZTs behind the cavity mirrors. One of the cavity detunings was varied slowly with a frequency below 1 Hz, whereas the other was varied fast with a frequency of about 1 kHz. From this procedure two-dimensional plots showing light power versus the one detuning that was varied slowly were derived. These two-dimensional plots therefore correspond to a projection of the three-dimensional plot onto one of the detuning axes, thereby collecting all maxima and minima along the other axis. The theoretical pictures for comparison with the experimental data correspond to 'side-views' onto the plane. in the three-dimensional plot along one or the other detuning axis.

Figure 2.18 presents the simulated values of the intra-cavity power versus detunings and the light power as detected by photo diode $\mathrm{PD_{GT}}$ when varying the detunings in the way described above. The resonance pattern of Fig. 2.18 (a) is periodic in $\Phi_1 \bmod \pi$ and in $\Phi_2 \bmod \pi$. Power enhancement is present around a maximum at

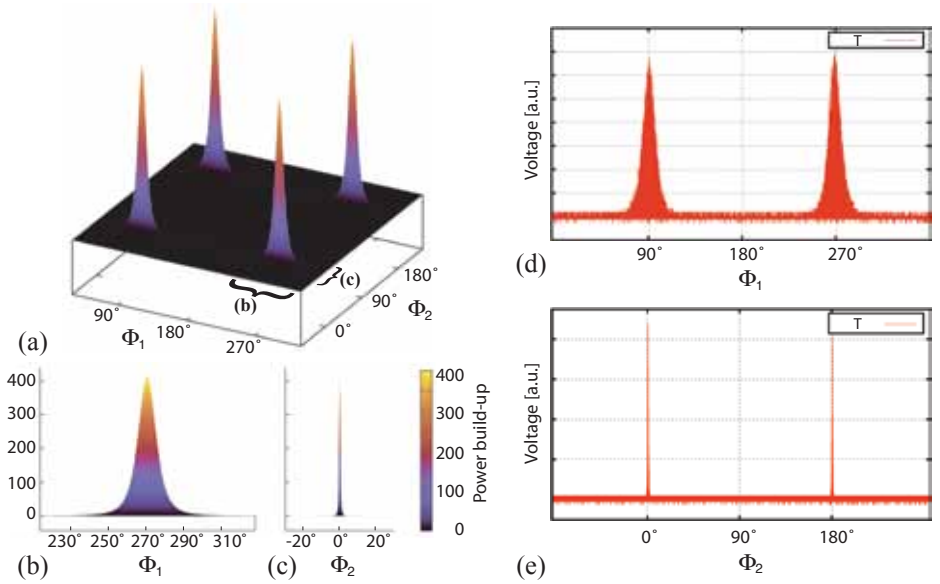

Figure 2.18.: Intra-cavity power build-up in the arm cavity as a function of the detunings Φ_1 and Φ_2 of the PR cavity and the arm cavity, respectively. Plot (a) shows the 3-dimensional simulation. Plots (b) and (c) are projections onto one of the axes, respectively. They well match the experimental data as given in plots (d) and (e). The latter two show the intra-cavity powers transmitted through the grating as detected by photo diode $\mathrm{PD_{GT}}$. For each plot one of the cavity lengths was varied slowly whereas the other was varied fast. Source: [94].

$\Phi_1 = 90°$ and $\Phi_2 = 0°$. These phases are a consequence of the grating phase relations as introduced earlier, and account for 3-port gratings with a (close to) minimal value for the second-order diffraction efficiency η_2^2 [93]. Simulated and experimental data in Fig. 2.18 (b,c) and (d,e), respectively, show a very good qualitative agreement. The existence of isolated equidistant resonances in Figure 2.18 is a special property of the optical cavity system as investigated here, and is in contrast to a conventional three-mirror cavity (confer Refs. [93,96]). It is in fact a direct consequence of the additional port C3. In order to gain a high power build-up in the arm cavity, output at this port has to be avoided. This happens only if the detunings of the subsystem cavities have particular values (modulo π) providing destructive interference between the field from the power-recycling mirror and the field leaking out the arm cavity.

Fig. 2.19 presents the characterization of the additional port $\mathrm{C3_{PR}}$ of the cavity

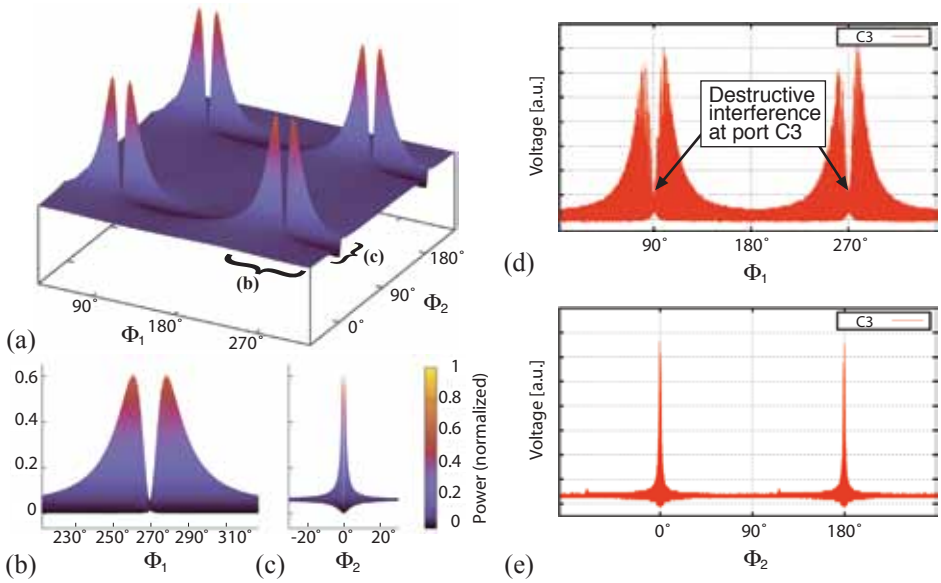

Figure 2.19.: Output power at the additional grating port $C3_{PR}$ as a function of the detunings Φ_1 and Φ_2 of the power-recycling cavity and the arm cavity, respectively. Plot (a) shows the 3-dimensional simulation. Plots (b) and (c) are projections onto one of the axes, respectively. They well reproduce the experimental data as given in plots (d) and (e). The latter two show the output powers as detected by photo diode PD_{C3}. For each plot one of the cavity lengths was varied slowly whereas the other was varied fast. The different peak heights in (d) were due to non-linearities in the PZTs used to vary the cavity lengths. Source: [94].

system. It shows simulated and measured light power at port $C3_{PR}$. Again simulated and measured data show a high degree of agreement. In Fig. 2.19 (a) it can be seen that for the detunings that provide the highest power build-up in the arm cavity a minimum light power is coupled out via port C3. Due to our measurement procedure this minimum is visible only in the projection onto detuning Φ_1. The doublet structure of the resonance in Fig. 2.19 is due to the power-recycling effect. When both cavities are detuned far from resonance, most of the light is back-reflected towards the laser source. If the arm cavity is on resonance, considerable power build-ups occur for a relatively wide range of detunings of the power-recycling cavity. But only for the optimum detuning of the power-recycling cavity ($\Phi_1 = 90°$) destructive interference occurs in port C3, giving rise to the sharp dip as shown in Fig. 2.19 (d).

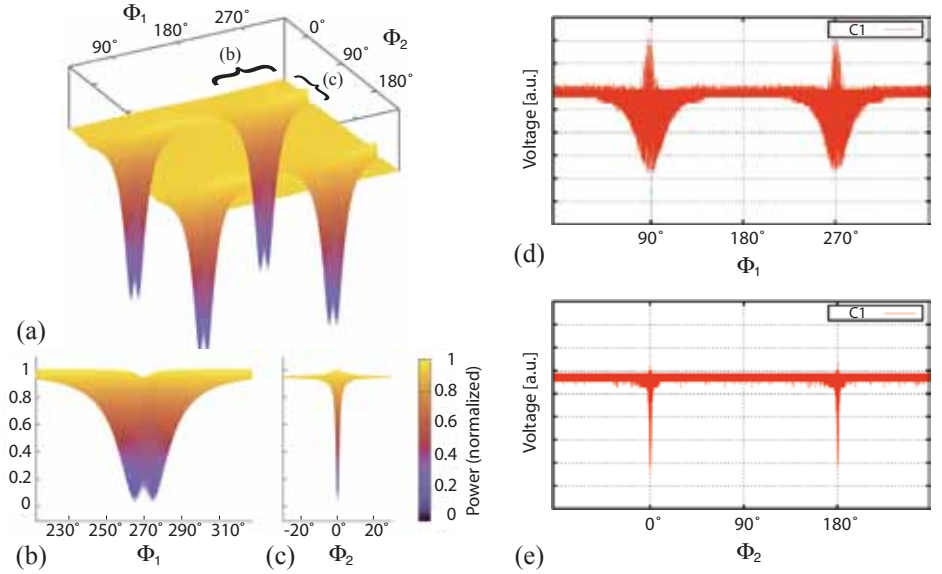

Figure 2.20.: From the coupled system to the laser source back-reflected power at port $C1_{PR}$ as a function of the detunings Φ_1 and Φ_2. (a) Simulation of the output power at port $C1_{PR}$. The traces (b) and (c) show the lateral view of the 3d-plot in (a). (d,e) Power detected at port $C1_{PR}$. The slow ramping frequency $f_{\Phi 1}$ and a significantly larger frequency $f_{\Phi 2}$ allow in (d) the experimental reproduction of (b). By switching the frequencies in (e) the simulated lateral view of (c) can be reproduced. Source: [51].

For completeness, in Fig. 2.20 the characteristics of the port that reflects the laser power back towards its source are presented. The yellow plain in Fig. 2.20 (a) represents the light that is reflected at the PR mirror with ρ_1, independently of any detuning. Close to maximum resonance in the arm cavity ($\Phi_2 \approx 0$) the power at this port shows the same characteristic as the reflection port of an impedance-matched linear two-mirror Fabry-Pérot cavity. On resonance, the residual reflectivity decreases, while in return the transmittance becomes maximal. This is due to the increasing compound reflectivity $\rho_c(\Phi_2)$. On resonance ($\Phi_1 = 90°$ and $\Phi_2 = 0°$) the back reflection barely increases again [see Fig. 2.20 (a-c)]. There, the compound reflectivity is close to one and therefore no impedance matching can be realized. The amplitude peaks in Fig. 2.20 (d) could were back to ringing effects due to high ramping frequencies of the coupled cavities [97].

To summarize one could say that in [94] the diffractive replacement of the transmissive coupling mirror located between a power-recycling cavity and a Fabry-Pérot arm cavity was shown. The findings were in agreement with the theoretical description based on the scattering matrix formalism. Although a 3-port grating used as a coupling component of two resonators opens an additional port, which is the third grating port C3, a significant power-recycling can be achieved. In the experiment presented above, almost no power was lost into the additional port due to destructive interference at this port. Thus it was shown that the power-recycling technology is transferable to 3-port-grating cavities employed as all-reflective arm cavities in an Michelson-type interferometer. Such a topology was investigated in the framework of this thesis and its experimental realization is presented in Chap. 3.

2.4. Signal response of optical resonators

In the previous section the applicability of 3-port gratings as coupling components to optical cavities was discussed. In the following, the signal response of such a grating cavity is derived.

2.4.1. Modulation of light fields - The phasor picture

The laser beam (at the laser frequency $f_0 = \omega_0/2\pi$) can be modulated at a radio frequency $f_{\mathrm{mod}} = \omega_{\mathrm{m}}/2\pi$. This results in either a phase or an amplitude modulation. For weak modulation, the resulting field approximated is a combination of the so-called upper sideband (at the frequency $f_0 = \omega_0 + \omega_{\mathrm{m}}/2\pi$), the lower sideband (at the frequency $f_0 = \omega_0 - \omega_{\mathrm{m}}/2\pi$) and the carrier field. For a more detailed description of modulated light fields see [98].

Phase modulation

The electric field at a certain location in space, being a function of frequency ω_0 and the time t can be desribed by

$$E_{\mathrm{in}}(t) = E_o e^{i\omega_0 t}. \tag{2.53}$$

A periodic modulation of the phase [99] with the modulation frequency ω_{m} and the modulation depth M can be written as

$$E_{\mathrm{in}}(t) = E_o e^{i(\omega_0 t + M \sin \omega_{\mathrm{m}} t)}. \tag{2.54}$$

The electric field of the phase-modulated light field can be described by the fourier series

$$E_{\mathrm{in}}(t) = E_o e^{i\omega_0 t} \sum_{k=-\infty}^{+\infty} J_k(M) e^{ik\omega_{\mathrm{m}} t}, \tag{2.55}$$

where the $J_k(x)$ represent the Bessel functions of the order k [98] and

$$J_{-k}(x) = (-1)^k J_k(x). \tag{2.56}$$

For small modulation indices ($M \ll 1$) and for the three terms of $k = 0, +1, -1$ due to $J_{-1} = -J_1$ the following approximation can be made

$$E_{\mathrm{in}}(t) \approx E_0 \left[J_0(M) e^{i\omega_0 t} + J_1(M) e^{i(\omega_0 + \omega_{\mathrm{m}})t} - J_1(M) e^{i(\omega_0 - \omega_{\mathrm{m}})t} \right]. \tag{2.57}$$

This means that optical fields were generated that have at the time $t = 0$ the phase relation of π due to $J_{-1} = -J_1$.

A commonly used visualization of the field properties is the so-called *phasor diagram* or *phasor picture*. Here, the complex scalar field [Eq. (2.53)] is displayed as a complex vector having the length E_0 and the phase $\omega_0 t$. Generally, this vector rotates around the origin at the frequency f_0. In the stationary picture, the coordinate system rotates with the same frequency and the real and imaginary axis are displayed such that the real axis points upwards [100]. Other light fields at differing frequencies are displayed on a third (z) frequency axis. In Fig. 2.21 the carrier and amplitude modulation sidebands at the modulation frequencies $\pm\omega_{\mathrm{m}}$ are shown at different times. To obtain the resulting sum phasor, the carrier and the sideband phasors are added as usually known from vectors. This is shown in Fig. 2.21 (b) and (d) for phase modulation sidebands. Note that the amplitude of the sidebands is $J_1(M) = M/2$ and that of the carrier $J_0(M) = 1 - M^2/4$. For small modulation indices ($M \ll 1$), almost all power remains in the carrier field.

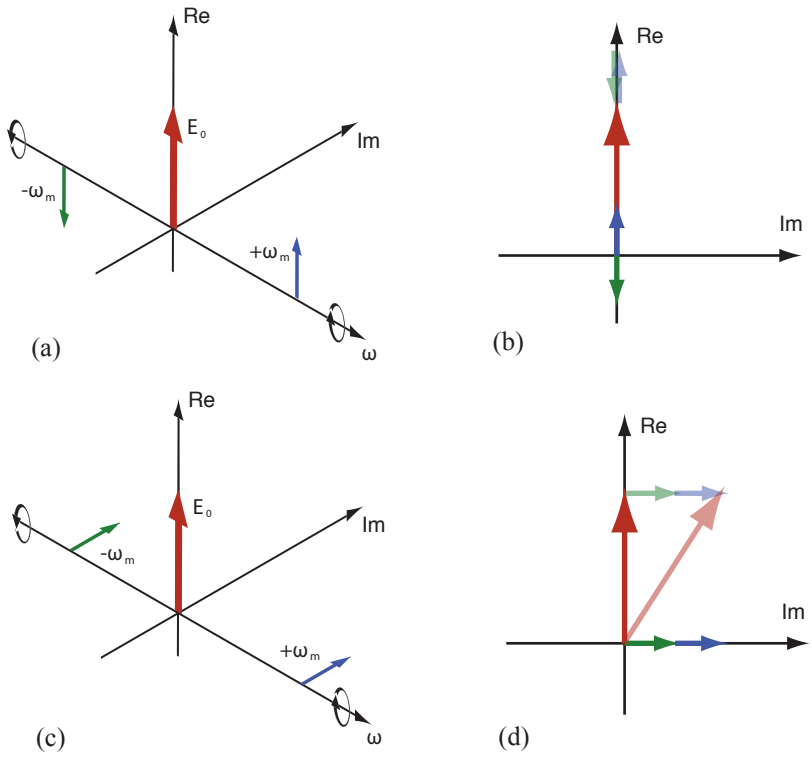

Figure 2.21.: Phasor diagram for phase modulation sidebands at time $t = 0$ (a) and at time $t = 2\pi/4\Omega$ (c) and the respective sum phasors (b,d).

Amplitude modulation

The periodic modulation of the amplitude of an optical field

$$\begin{aligned} E_{\mathrm{in}}(t) &= E_o e^{i\omega_0 t}(1 + M \sin \omega_{\mathrm{m}} t) \\ &= E_o e^{i\omega_0 t}\left[1 + \frac{M}{2i}(e^{i\omega_{\mathrm{m}} t} - e^{-i\omega_{\mathrm{m}} t})\right] \\ &= E_o e^{i\omega_0 t}(1 - i\frac{M}{2}e^{i\omega_{\mathrm{m}} t} + i\frac{M}{2}e^{-i\omega_{\mathrm{m}} t}). \end{aligned} \tag{2.58}$$

At an initial time $t = 0$ the sidebands have a phase relation of π to each other and, additionally, a phase difference of π to the carrier. Figure 2.22 shows the carrier and

the sidebands at two times and the sum phasor of the resulting field [see Fig. 2.22 (b) and (d)].

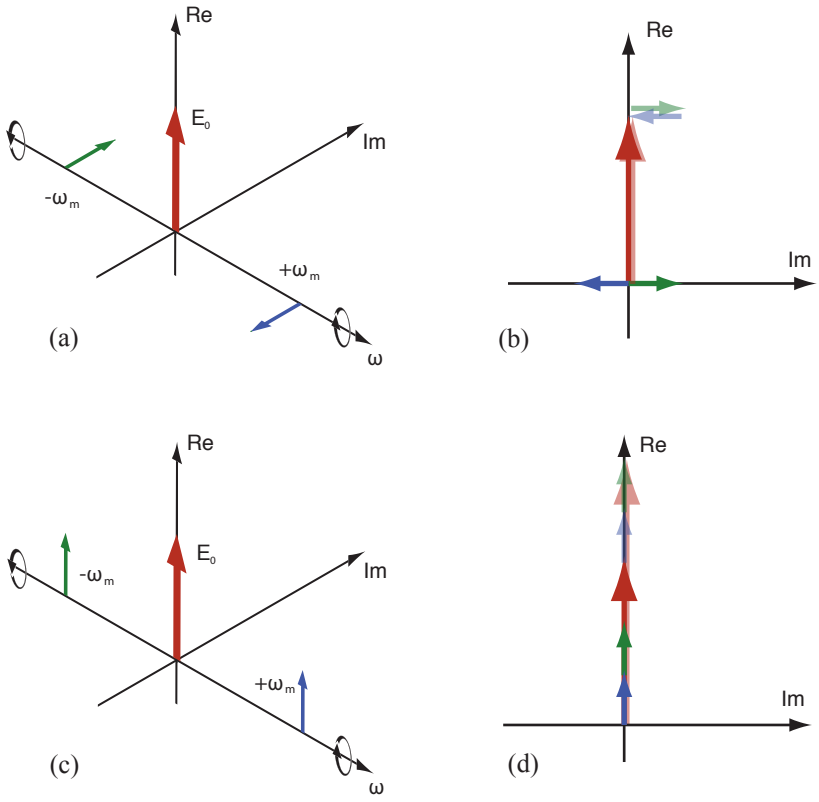

Figure 2.22.: Phasor diagram for amplitude modulation sidebands at time $t = 0$ (a) and at time $t = 2\pi/4\Omega$ (c) and the respective sum phasors (b, d).

2.4.2. Signal response of optical resonators in the phasor picture

Laser GW interferometers are operated close to their *dark fringe*, which means that due to destructive interference almost no light leaves the signal port and all optical power is reflected back to the laser. If a gravitational wave interacts with the light fields in the Fabry-Pérot arm cavities, phase modulation sidebands are generated. In the case of a conventional (transmissively coupled) arm cavity, the *full* signal interferes constructively at the interferometer's signal port, manifesting itself as an amplitude modulation. A single detector in the signal port is therefore sufficient to gather the full information available, as illustrated in Fig. 2.23 (a). This is different for a diffractively-coupled arm cavity in a second-order Littrow configuration [Fig. 2.23 (b)]. If the second-order diffraction efficiency is minimal, the carrier field still interferes constructively at the input port [C1 in Figure 2.23 (b)], while the additional forward-reflection port C3 remains dark (see Section 2.3.2). The phase modulation signal generated inside the cavity is split equally into the back-reflected port C1 and the forward-reflected port C3 because of the symmetric binary grating structure [51]. Hence, two signal ports instead of only one have to be considered for the derivation of the signal response of a grating cavity in second-order Littrow.

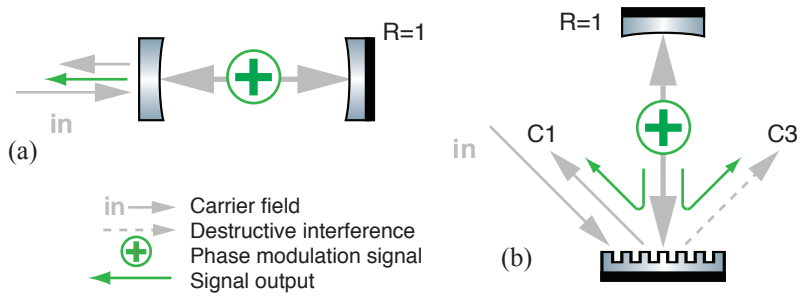

Figure 2.23.: (a) Signal response of a linear standing-wave Fabry-Pérot (FP) cavity. Both, signal and carrier are back-reflected towards the laser source. (b) Signal response of a single-ended 3-port-grating cavity with reflection ports C1 and C3. While the carrier interferes destructively at C3, the signal is distributed equally among the two ports.

In the following, optical cavities are analyzed with respect to their signal response to a phase modulation signal. Experimentally this can be realized by an electro-optical modulator where the index of refraction is a function of the voltage applied. If a

sinusoidal voltage is applied, phase modulation sidebands are generated. Another option is to longitudinally sweep the end mirror of a cavity.

2.4.3. Linear Fabry-Pérot cavity in the phasor picture

In Fig. 2.24 the input and output phasors of a linear impedance-matched Fabry-Pérot resonator on resonance are shown. Inside the cavity, a phase modulation signal is applied to the carrier. The reference system is defined by the incoming vector depicted in red [see Fig. 2.24 (a)]. Like shown in Eq. (2.14) the carrier picks up a phase shift of $\pi/2$ when being transmitted through a coupling mirror [Fig. 2.24 (b)]. Phase modulated signals (green) are depicted perpendicular to the carrier. For simplicity, the two sidebands in Fig. 2.21 (d) are depicted as one single vector. Although on resonance

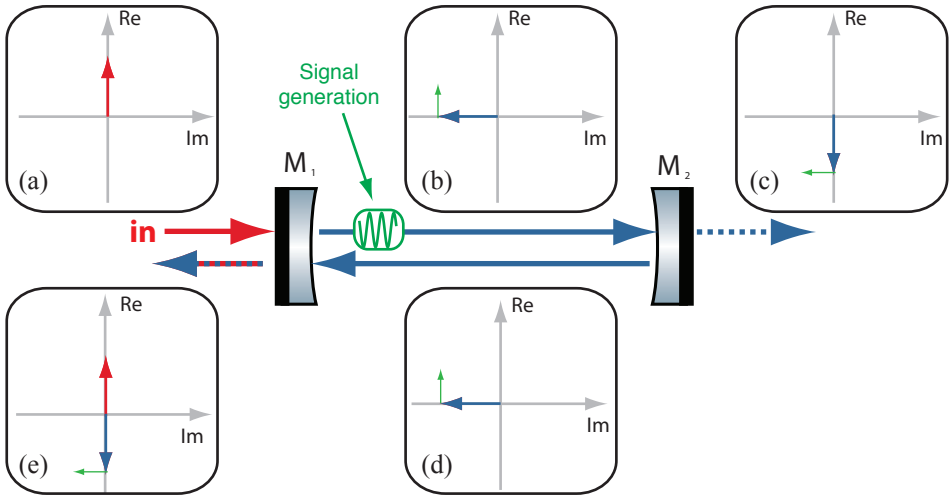

Figure 2.24.: Phasor diagram of a linear impedance-matched Fabry-Pérot cavity on resonance. The phase relations are chosen according to scattering matrix of Eq. (2.14). (a) The incoming reference light field. (b) Due to transmission, a phase of $\pi/2$ is added to the carrier. The phase modulation signal (green phasor) is perpendicular to the carrier. (c) The cavity outcoupling generates a constructive interference at the transmission port with a phase modulation signal. (d) Due to the resonance condition the phasor of the reflected beam points into the same direction as in (b). (e) The carrier field reflected at the cavity interferes destructively with the carrier coupled out of the cavity, while the signal remains.

all light is transmitted and, consequently, the reflection port becomes dark, a phase modulation signal remains at the two ports [Fig. 2.24 (c) and (e)]. In other words, the magnitude of the signal that is generated inside the cavity and then transmitted through the two outcoupling mirrors scales with the transmission coefficient of the mirrors. In the loss-less and impedance-matched case those are the same ($\tau_1^2 = \tau_2^2$) and one half of the signal is sent to the transmission port and to the reflection port, respectively. If a signal is generated inside a single-ended cavity (e.g. inside the arm cavity of a gravitational wave interferometer) no signal is transmitted through the end mirror, but the complete signal is sent back (via transmission at the *incoupling* mirror) to the source of the carrier.

2.4.4. 3-port-grating cavity in the phasor picture

Introduction

In section 2.3.2 it was shown that the output characteristics at the two reflection ports of the 3-port-grating coupled cavity depend on the ratio of the second- and zeroth-order diffraction efficiency. On resonance, maximal and minimal values for the destructive and constructive interference at the two reflection ports are realized at maximal and minimal second-order diffraction efficiencies. The resulting phase shifts (ϕ_0, ϕ_1 and ϕ_2) for the respective diffraction-order are given in Eqs. (2.18–2.20) and graphically displayed in Fig. 2.8 as a function of η_2. The phase shift ϕ_2 of the second diffraction order has a considerably steep characteristic close to the minimal and maximal boundary value [see Fig. 2.8 (b)], and the characteristic of the phase shift ϕ_1 of first diffraction order is considerably steep towards the maximal η_2-value [see Fig. 2.8 (a)]. Their steep phase dependence might suggest a rather sensitive dependence of the cavity outputs, since the complete constructive interference at port C3 (and the a complete destructive interference at port C1, respectively) occur *at* the boundary value for $\eta_{2\mathrm{min}}$. In analogy the complete constructive interference at port C1 (and the a complete destructive interference at port C3, respectively) occur *at* the boundary value for $\eta_{2\mathrm{max}}$. Thus, a small deviation from the minimal/maximal value of η_2 causes a large change of the phase shift. These large changings of phases as a function of η_2 have, however, a rather weak impact on the interference characteristics at the two ouput ports. The characteristics show a rather smooth gradient from com-

pletely constructive to completely destructive interference (and vice versa at the other port) as a function of η_2 and the cavity detuning Φ as shown in Fig. 2.25. The power outputs at the ports C1 and C3 are displayed according to Eqs. (2.44) and (2.46) for a loss-less and single-ended ($\rho_1^2 = 1$) 3-port-grating coupled cavity and for a constant cavity input efficiency of $\eta_1^2 = 5\,\%$. Note that according to Eq. 2.26 this also defines the zeroth order diffraction efficiency. Consequently, the three cases $\eta_2 = \eta_{2\mathrm{min}}$, $\eta_2 = \eta_{2\mathrm{max}}$, and $\eta_2 \neq \eta_{2\mathrm{max/min}}$ are considered in the following.

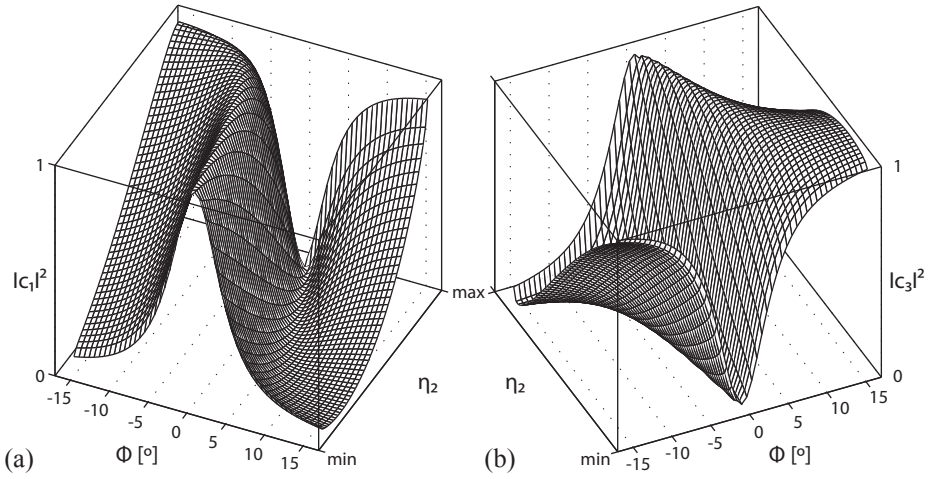

Figure 2.25.: Power outputs of a single-ended 3-port-grating cavity at the two reflection ports C1 and C3 as a function of η_2 and the cavity detuning Φ for an input efficiency of $\eta_1^2 = 5\,\%$. (a) Backward-reflected port C1. (b) Forward-reflected port C3. Depending on the efficiency the output changes from a completely constructive to a completely destructive interference (and vice versa).

3-port grating with $\eta_2 = \eta_{2\mathrm{min}}$

For a grating in $\eta_{2\mathrm{min}}$-configuration the ports C1 and C3 behave just like the transmission and reflection ports of an impedance-matched linear Fabry-Pérot cavity (see Fig. 2.25). In Fig. 2.26 this case is depicted in the phasor picture for phase modulation signal sidebands generated inside the grating cavity and depicted as the green phasor. The input field [Fig. 2.26 (a)] defines the reference for the co-rotating phasor system. When being diffracted at the grating, the light receives a phase shift of $\phi_1 = \pi/2$ according to Eq. (2.19). The resonant light is coupled out of the cavity in (plus and minus) first-order diffraction ($\eta_{\pm 1}$) towards the ports C1 and C3. Since the second diffraction order receives a phase shift of $\phi_1 = \pi$ [Eq. (2.19)], the carrier light that is coupled out of the cavity interferes constructively at the backward reflected port C1 [Fig. 2.26 (e)]. By contrast the forward-reflected port becomes dark for the carrier [Fig. 2.26 (d)]. The signal, on the other hand, splits equally into the two grating ports.

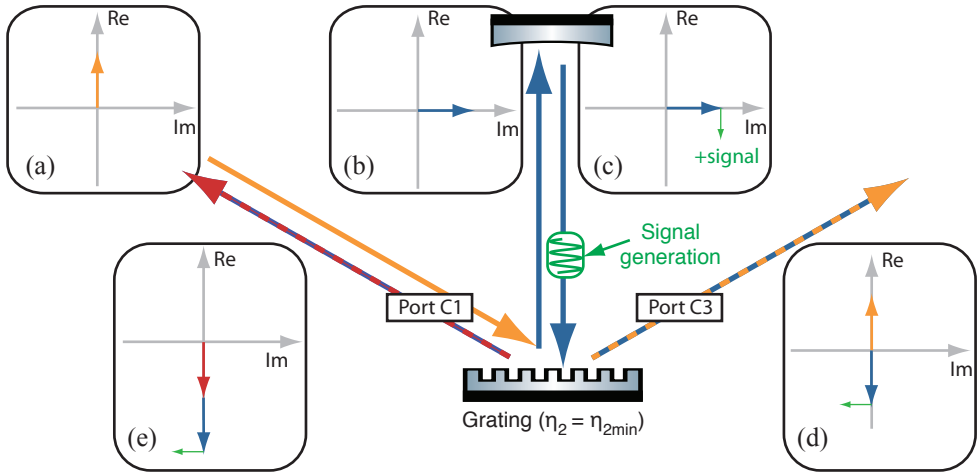

Figure 2.26.: Phasor diagram for a 3-port-grating cavity with $\eta_2 = \eta_{2\mathrm{min}}$ on resonance. (a) The incoming reference light field. (b) Because of the first-order diffraction, the phase of $\phi_1 = \pi/2$ is added to the carrier, see Eq. (2.19). (c) The phase modulation signal is perpendicular to the carrier. (d,e) The resonant light is coupled out of the cavity via (plus and minus) first-order diffraction towards the ports C1 and C3. Again a phase shift of $\phi_1 = \pi/2$ is added. (d) The outcoupled light field and the field in the zeroth diffraction order interfere destructively at port C3. (e) The beam that is reflected at the cavity via the second diffraction order and the light field that is coupled out of from the cavity interfere constructively.

3-port grating with $\eta_2 = \eta_{2max}$

If the 3-port grating is designed with a maximal η_2-value and, correspondingly, a minimal η_0-value, the outputs at the reflection ports switch with respect to the $\eta_{2\min}$-configuration (see Fig. 2.25). In this configuration, not only the phase ϕ_2 of the second diffraction order, but also the phase shift ϕ_1 that is added to the carrier when being diffracted in the first diffraction order, show a rather steep characteristic towards their boundary value, which can be seen in Fig. 2.8. In contrast to previous case with $\eta_{2\min}$, no phase shift is added to the carrier [$\phi_1 = 0$, see Eq. (2.19), see Fig. 2.27 (b)]. Now, the forward-reflected port C3 becomes bright on resonance because the light field that is forward reflected at this port and the field coupled out of the cavity interfere constructively [see Fig. 2.27 (d)]. By contrast the backward-reflected port now behaves similarly to the reflection port of a linear impedance-matched FP-cavity [Fig. 2.27 (e)]. The signal, independently of the η_2-value, splits equally into the forward-reflected and

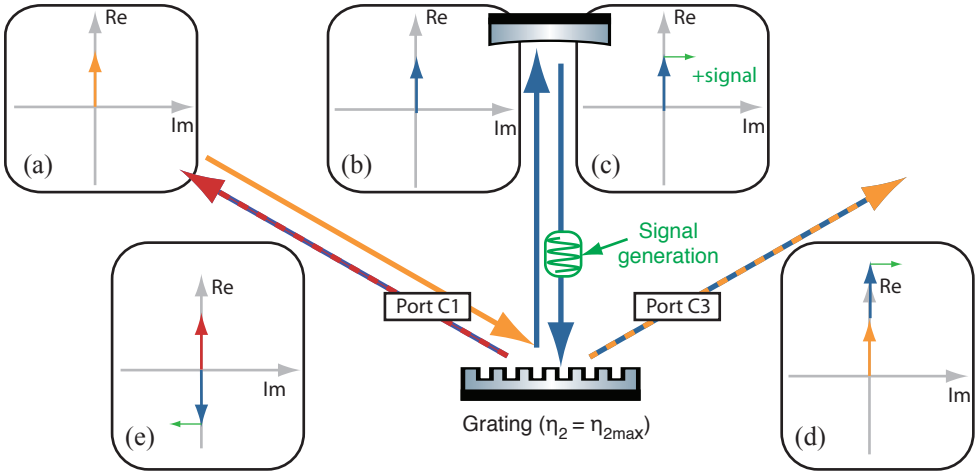

Figure 2.27.: Phasor diagram for a 3-port-grating cavity with $\eta_2 = \eta_{2\max}$ on resonance. (a) The incoming reference light field. (b) Because of the maximal second-order diffraction efficiency no phase shift is added to the incoupled field ($\phi_1 = 0$). (c) The phase modulation signal is perpendicular to the carrier. (d,e) The resonant light is coupled out of the cavity in (plus and minus) first-order diffraction towards the ports C1 and C3. Again, no phase shift appears and thus the outcoupled light field and the field of the zeroth diffraction order interfere constructively at port C3. (e) In return the beam that is reflected at the cavity via the second diffraction order and the light field that is coupled out of from the cavity interfere destructively at port C1.

the backward-reflected port of the grating cavity.

3-port grating with $\eta_2 = \eta_{2\mathrm{mid}}$

Only for the two configurations that implement a 3-port grating with the minimal or the maximal η_2-value, the phase shifts that are functions of this diffraction efficiency lead to fully destructive and constructive interferences at the two reflection ports. In reality, the diffraction values always slightly differ from the extremal values since they are boundary values that cannot be reached with 'real' gratings. Consequently, the phases in Eqs. (2.19) and (2.20) differ from the cases for $\eta_{2\mathrm{min}}$ and $\eta_{2\mathrm{max}}$ discussed above (see Fig. 2.8). The light fields as shown in Fig. 2.28 do not interfere perfectly destructively and constructively. In analogy to the previous cases, no phase shift is added to the field that is forward reflected via the zeroth diffraction order [$\phi_0 = 0°$, see Fig. 2.28 (a, d)]. The phases added to the light field when being diffracted in the first and second diffraction, lead to a differing orientation with respect to the incoming field Fig. 2.28 (e, b) as seen in the two earlier cases. However, the generated phase modulation signals are still perpendicular to the intra-cavity phasor [Fig. 2.28 (c)]. The resulting output at the ports is therefore only a partially destructive and constructive interference [Fig. 2.28 (d, e)]. As a further consequence, the phase modulation partially transforms into an amplitude modulation as shown in Fig. 2.29. There, the sum vector of zeroth (Port C3) and second (Port C1) diffracted order and the phasor representing the light that is coupled out of the cavity (blue) are shown together with the respective carrier field. The resulting amplitude modulations at the ports C1 and C3 have a phase difference of π.

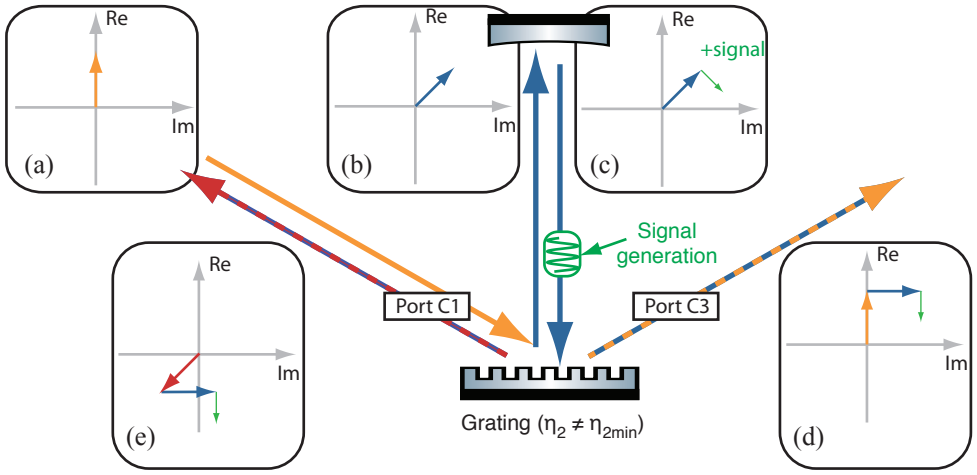

Figure 2.28.: Phasor diagram for a 3-port-grating cavity with $\eta_2 = \eta_{2\mathrm{mid}}$ on resonance. (a) The incoming reference light field. (b) A η_2-value clearly apart from the upper or the lower boundary value leads to phase shifts Φ_1 and Φ_2 that lead to a differing orientation of the phasor as seen for diffraction values that meet the extremal value $\eta_{2\mathrm{min/max}}$. (c) The phase modulation signals are still perpendicular to the intra-cavity phasor. (d, e) The resulting output at the reflection ports C1 and C3 is therefore only a partially destructive and constructive interference and the phase modulation partially transforms into an amplitude modulation.

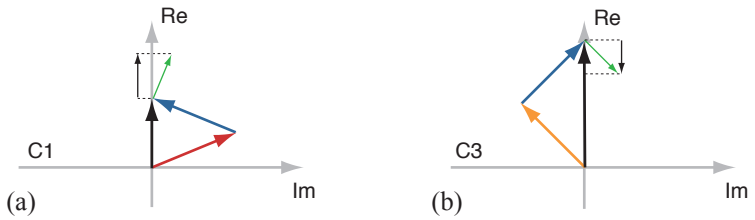

Figure 2.29.: Phasor diagram for the reflection ports C1 (a) and C3 (b) of a 3-port-grating cavity with $\eta_2 \neq \eta_{2\mathrm{min}}$ on resonance. The phase modulation signals generated inside the cavity transform into a partial amplitude modulation at each of the two ports. The modulations finally detectable at the two ports have a phase difference of π with respect to each other.

2.5. Transfer functions

The interaction of a a gravitational wave with the arm cavity of an interferometric gravitational wave detector can be interpreted as the generation of phase modulation signal sidebands inside the arm cavity. In this section the signal transfer functions for phase modulation induced sidebands of 3-port-grating coupled cavities are compared to the signal transfer function of a linear Fabry-Pérot cavity. According to Eq. (2.57), the normalized signal transfer function for the maximum phase quadrature readout is given by

$$\mathbf{G}(\Omega) \quad = \quad \mathrm{g}(+\Omega) - \mathrm{g}^*(-\Omega), \tag{2.59}$$

assuming the normalized carrier to be real and positive [98], where $\mathrm{g}(\pm\Omega)$ is the frequency-dependent enhancement of upper and lower sidebands inside the cavity. The maximum amplitude quadrature readout is given by (see Eq. (2.58))

$$\mathbf{G}(\Omega) \quad = \quad \mathrm{i}[\mathrm{g}(+\Omega) - \mathrm{g}^*(-\Omega)]. \tag{2.60}$$

For the reflection port of the linear Fabry-Pérot cavity (as well as for a grating cavity coupled in first-order Littrow) this signal transfer is given by

$$\mathrm{g}_{\mathrm{FP}}(\pm\Omega) = \frac{\mathrm{i}\tau_1 e^{\mathrm{i}(\Phi \pm \Omega L/\mathrm{c})}}{1 - \rho_1\rho_2 e^{2\mathrm{i}(\Phi \pm \Omega L/\mathrm{c})}} \tag{2.61}$$

with the parameters of the grating ($\tau_{1,2}$ and $\rho_{1,2}$) and the cavity (Ω and L) discussed above. Note that the signals are generated inside the cavity and then transmitted through the coupling mirror towards the detection port. Therefore the signal transfer function can be deduced from the equation for the transmission of the linear FP-cavity given in Eq. (2.33) taking into account that only the amplitude transmittance τ_1 needs to be considered [90].

In Fig. 2.30, the transfer functions for phase modulation induced signal sidebands in a standing-wave linear Fabry-Pérot cavity are shown. The length of the cavity is chosen to be 1 km and the input transmission is $\tau_1^2 = 2\,\%$, the reflectivity of the coupling mirror is $\rho_1^2 = 98\,\%$, respectively. Figures 2.30 (a, b) show the magnitude and the phase characteristics of the upper (red) and lower (green) sidebands in the resonant case. If the cavity is detuned the resonance frequency can be shifted. Figures 2.30 (c,

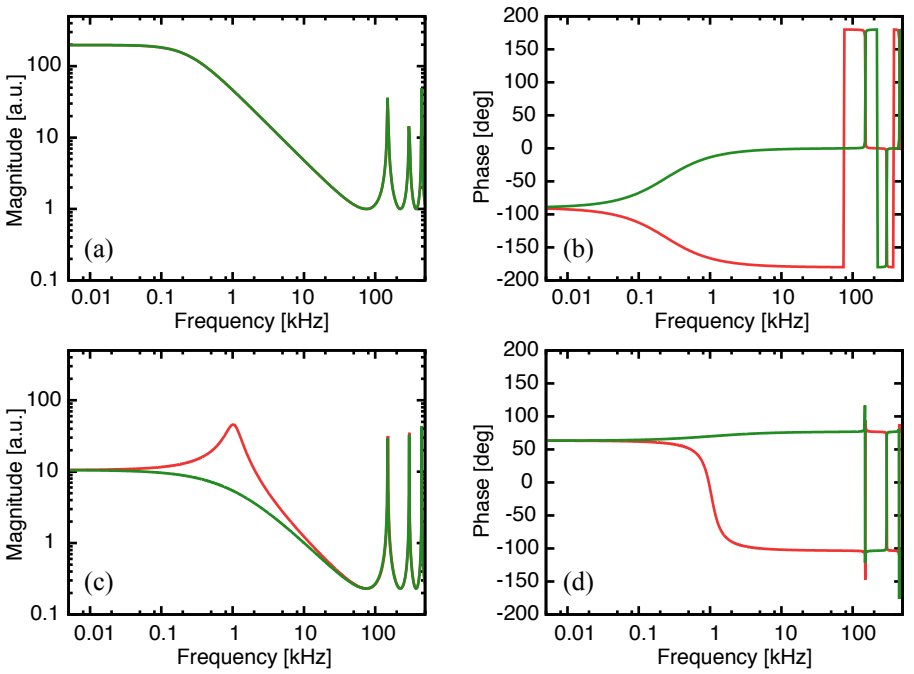

Figure 2.30.: Transfer functions for phase modulation induced sidebands for single-ended linearly coupled Fabry-Pérot cavity with $L = 1\,\mathrm{km}$ and an input transmission of $\tau_1^2 = 2\,\%$. (a, b) Magnitude and phase characteristics of upper (red) and lower (green) sideband for the tuned case ($\Phi = 0$). (c, d) Magnitude and phase for a detuned scenario. The resonance for the upper sideband is shifted by 1 kHz.

d) show the characteristics for the detuned case but the equal input power. The resonance for the upper sideband is shifted to 1 kHz. For the simulations presented in this section the simulation tool FINESSE was used [101].

As discussed in the previous section, in the case of a 3-port grating coupled arm cavity, the signal transfer functions are identical for the two output ports C1 and C3 because of the symmetrical structure of a 3-port grating. They read as

$$\mathrm{g_{C1}}(\pm\Omega) = \mathrm{g_{C3}}(\pm\Omega) = \frac{\eta_1 e^{\mathrm{i}(\phi_1+\Phi\pm\frac{\Omega L}{\mathrm{c}})}}{1-\rho_0\rho_2 e^{2\mathrm{i}(\Phi\pm\frac{\Omega L}{\mathrm{c}})}}, \tag{2.62}$$

with the parameters of the grating (η_1, ϕ_1, and ρ_0) and of the end mirror (ρ_2). Similar to the linearly coupled resonator this equation can be deduced from the amplitude

reflection coefficients for the two reflection ports of the 3-port-grating cavity given in Eqs. (2.44) and (2.46).

In Fig. 2.31 the transfer functions for phase modulation induced signal sidebands for 3-port-grating coupled cavity according to Eq. (2.62) are shown for the two similarly behaving reflection ports C1 and C3. In analogy to the linear FP-cavity and to keep the cavity parameters comparable, the length is chosen to $L = 1\,\mathrm{km}$ and the reflectivity of the grating is $\rho_0^2 = 98\,\%$. Thus, according to Eq. (2.17) the input efficiency is $\eta_1^2 = 1\,\%$. Consequently, the power build-up inside the cavity and the corresponding signal magnitude are smaller by a factor of two when compared to a linear cavity. The magnitude is reduced by an additional factor of two because of the fact that the signal is split in two at the grating. Figure 2.31 shows only one of the two reflection ports of the grating cavity. The other diffraction efficiencies of the grating are chosen such that $\eta_{2\mathrm{min}}$ is minimal. This configuration is the most reasonable for potential interferometric applications because of the potential power-recycling topologies as exemplarily shown in section 2.3.3 . In Fig. 2.31 (a, b), the magnitude and the phase characteristics for the tuned case are shown.

Figure 2.31 (c, d) presents the detuned case with the cavity detuned by 1 kHz but the equal input power. The magnitude and the phase for the upper (red) and lower (green) sideband show a behavior similar to that of a linear cavity shown in Fig. 2.30. Apart from the first-order efficiency, the magnitude of the signal transfer function does not depend on the grating's diffraction efficiencies. The only parameter depending on the diffraction efficiencies [Eq. (2.17)] is the first-order phase ϕ_1. Thus, the same signal strength can be achieved even with gratings having a second-order diffraction efficiency that significantly differs from the minimal boundary value, when assuming a detection at an optimized angle and an optimized readout quadrature.

On resonance, for either of the two resonator types shown in Fig. 2.30 and Fig. 2.31 (grating in $\eta_{2\mathrm{min}}$-configuration) the maximum signal detection for the case of phase modulation signal sidebands can be realized in the carrier light's phase quadrature [see Eq. (2.59)]. Thus, two factors have to be taken into account to achieve a similar signal level for both, the grating cavity and the linear resonator. Firstly, the power input has to be a factor of two higher to achieve the same intra-cavity power level and the corresponding enhancement of the signal sidebands. Secondly a signal readout has to be carried out at the two reflection ports of the 3-port-grating cavity to gain the full

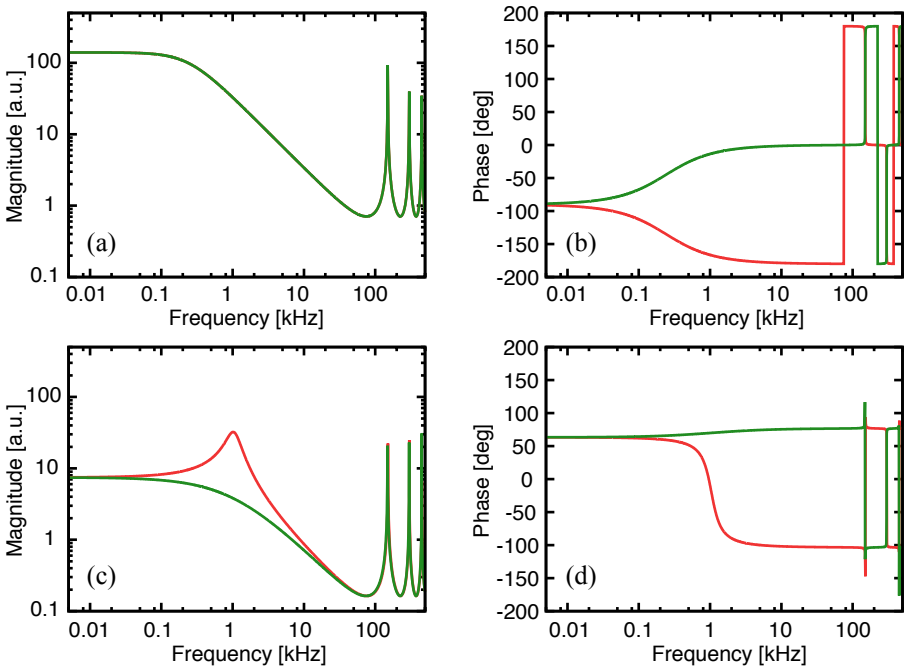

Figure 2.31.: Transfer functions for phase modulation induced sidebands for the two reflection ports C1 *or* C3 of the 3-port-grating coupled cavity. A grating with $\eta_{2\mathrm{min}}$-configuration, no loss and a perfect end mirror are assumed. The length $L = 1\,\mathrm{km}$ and a grating reflectivity of $\rho_0^2 = 98\,\%$ are chosen. (a, b) Magnitude and phase characteristics of upper (red) and lower (green) sideband for the tuned case ($\Phi = 0$). (c, d) Magnitude and phase for a detuned scenario. The resonance for the upper sideband is shifted by 1 kHz.

signal strength.

In Fig. 2.32 the phase quadrature readouts for the two resonators discussed above are shown. The readouts are calculated according to Eq. (2.59). The two resonators have the same intra-cavity power, which means that the input power to the grating cavity has to be twice that required for the linear cavity. The readouts at the two ports C1 and C3 of the grating cavity are smaller by a factor of two. The sum of the two signals has, however, the same magnitude as the reference linear Fabry-Pérot cavity. Thus, when implementing a 3-port grating in an all-reflective interferometer setup, an alternative signal detection scheme is necessary to gain the full signal information. This means that a readout has to be carried out at the forward-reflected port. For

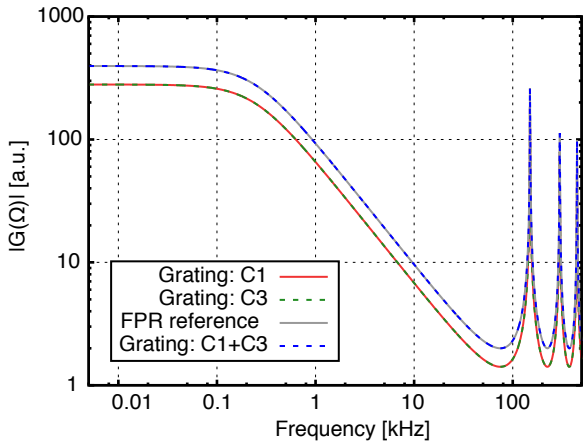

Figure 2.32.: Phase quadrature readout for the reflection port of the linear cavity and the the two output ports of the grating coupled cavity for phase modulation signal sidebands. The signals of the forward-reflected port C3 (dashed green) and the backward reflected port C1 (red) sum up to equal strength of the reference signal of the linear FP-cavity (grey). Note that the laser input to the grating cavity needs to be a factor of two higher to achieve the same power build up.

this, a homodyne readout scheme as known from squeezed light experiments can be used [102, 103]. This detection scheme comprises the advantage of tunable quadrature angles for the case that a 3-port grating with second-order diffraction efficiency significantly differing from the minimal boundary value is used. For an interferometer with 3-port-grating coupled arm cavities this need for a signal detection at the forward-reflected ports leads to the creation of a second interferometric detection port where the light fields from the forward-reflected ports of the two arm cavities are brought to interference.

2.6. Chapter summary

In this chapter, an introduction to diffractive optics was provided and the properties of 3-port-grating coupled cavities were discussed. The outputs at the forward- and the backward reflected ports of such a grating cavity are functions of the end mirror transmission, the cavity detuning and on the concrete diffraction efficiencies of zeroth and second-order. The theoretical predictions were verified by an earlier experimen-

tal realization of a 3-port-grating cavity with power recycling presented in [94] and summarized in this chapter. Grating cavities were investigated with respect to phase modulation signals. The transfer functions and the phasor picture as a more intuitive approach were provided. It was shown that a proper signal read-out at a 3-port-grating cavity has to be carried out at both output ports to gain the full signal strength.

In the following the experimental investigations and the results achieved in the framework of this thesis are presented. In the next Chap. 3 the realization of an Michelson-type interferometer with diffractively coupled arm resonators and the resulting second detection port is presented. The second application of 3-port-grating coupled cavities, presented in this work, is the use of such a cavity for optical feedback to a semiconductor laser diode. The results of this investigation are shown in Chap. 4.

Chapter 3

A Michelson interferometer with grating arm cavities

In this chapter, the experimental realization of a Michelson-type interferometer with 3-port-grating coupled arm cavities is presented. As mentioned in the previous chapter the 3-port grating provides an additional port where a signal has to be detected to gain the same signal strength as known from Michelson-type interferometers with transmissively coupled arm resonators. Consequently, a second detection port to collect the signal from the additional port is required. The resulting topology is shown in Fig. 3.1. In the following the experimental setup, the characterization of the dielectric grating used in the experiment, the obtained results as well as the experimental restrictions and limitations are presented. The results of this experiment have been published in [104].

3.1. Grating characterization

The two diffractive cavity couplers used in the experiment were cut from one initial substrate designed and manufactured by our project partners in Jena [see Fig. 3.2 (a)]. The binary grating structure, having a grating period of 1450 nm, was etched in the topmost layer of a highly reflective multilayer coating consisting of tantala (Ta_2O_5) and fused silica (SiO_2). Initially, the grating was characterized with respect to its diffraction efficiencies. Figure 3.2 shows the grating and the measured diffraction effi-

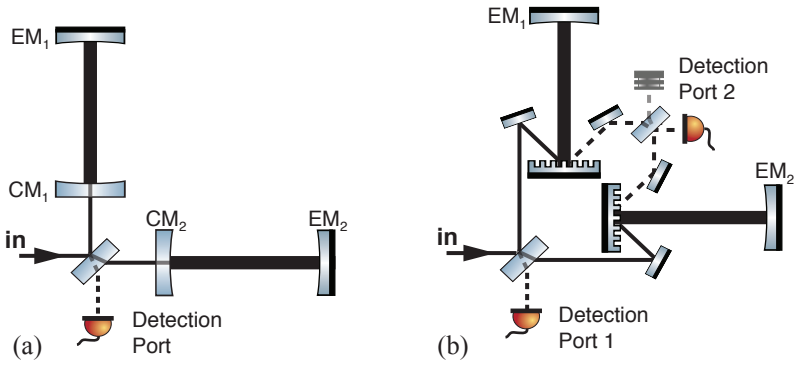

Figure 3.1.: (a) Michelson-type laser interferometer with conventional arm cavities, consisting of the (partially transmissive) coupling mirrors $CM_{1,2}$ and the highly reflective end mirrors $EM_{1,2}$. (b) Interferometer with diffractively-coupled arm cavities. Because of the second-order Littrow configuration, the signal is distributed into two ports that both need to be monitored to obtain the full signal strength.

ciencies of interest at normal incidence and at second-order Littrow incidence, respectively. The obtained results are presented in Table 3.1. Since the grating is mounted in second-order Littrow configuration the measurement of the diffraction efficiencies is carried out at the corresponding input angle of $\alpha_{\text{in}} = 47.2\,^\circ$ [see Fig. 3.2 (b)]. To check the grating's symmetry with respect to the ridges and grooves as well as the correspondingly related diffraction efficiencies $\eta_{\pm 1}$, measurement at normal incidence was carried out [see Fig. 3.2 (c)]. Usually, in the design process grating structure and multilayer coating are optimized for s-polarized light (TE polarization). Thus, the

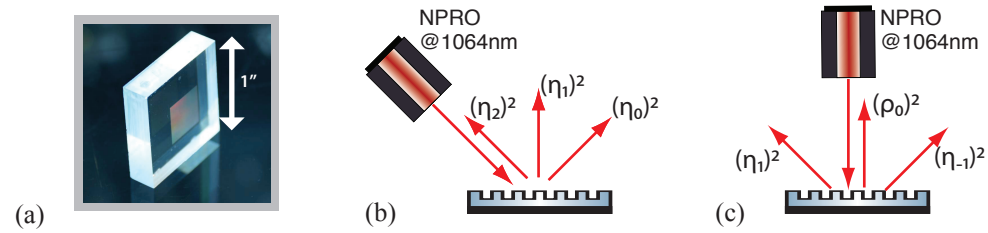

Figure 3.2.: (a) Optical substrate with a grating structure on top of the HR-mulitlayer coating. (b) Measurement of the diffraction efficiencies at a second-order Littrow angle of 47.2°. (c) Measurement at normal incidence.

characterization was carried out using a 1064 nm beam in s-polarization provided by a single-mode Nd:YAG laser (non-planar ring oscillator, NPRO). Note that several gratings were manufactured and characterized (see App. A). The grating chosen for the experiment was the one providing the lowest transmission, similar values for the first-order diffraction efficiencies $\eta_{\pm 1}$ at normal incidence, and a second-order diffraction efficiency very close to the theoretical minimal value $\eta_{2\mathrm{min}}$. The latter suggests low influence of the applied grating structure on the reflectivity of the multilayer coating.

Table 3.1 presents the parameter of the 3-port grating chosen for the experiment. The grating had a first-order diffraction efficiency of $\eta_1^2 = 3.30\,(\pm 0.23)\,\%$ and a correspondingly small second-order efficiency of $\eta_1^2 = 0.04\,(\pm 0.02)\,\%$. The normal incidence measurement revealed almost perfectly symmetrical values for η_{-1}^2 and η_{+1}^2 and a very low transmission of $\tau_0^2 = 21\,(\pm 3)\,\mathrm{ppm}$ [105], which is clearly lower than the transmission values of gratings from earlier fabrication runs [50].

Table 3.1.: Parameters obtained in the characterization procedure.

incident light	**parameter**	**measured value**
2nd order Littrow	0th diffraction order (η_0^2)	$96.41\,(\pm 2.30)\,\%$
	1st diffraction order (η_1^2)	$3.30\,(\pm 0.23)\,\%$
	2nd diffraction order (η_2^2)	$0.04\,(\pm 0.02)\,\%$
normal incidence	-1st diffraction order (η_{-1}^2)	$3.53\,(\pm 0.26)\,\%$
	$+1$st diffraction order (η_{+1}^2)	$3.52\,(\pm 0.26)\,\%$
	transmission (τ_0^2)	$21\,(\pm 3)\,\mathrm{ppm}$

In Fig. 3.3, a simulation of the characteristics of the reflected ports (C1,C3), the transmission at the end mirror (T), and the intra-cavity field of a grating cavity are shown. The simulation is based on the grating parameters summarized in Table 3.1. For a loss-less and single-ended resonator, a maximal power build-up by a factor of 29 can be achieved. Since every optical device (grating, electro-optical modulators, mirrors) leads to a certain loss (by scattering or absorption), Fig. 3.3 illustrates the output characteristics at the grating ports C1, C3 and the intra cavity field as a function of the power transmissivity of the end mirror. This transmissivity can be seen as optical loss that occurs inside the cavity.

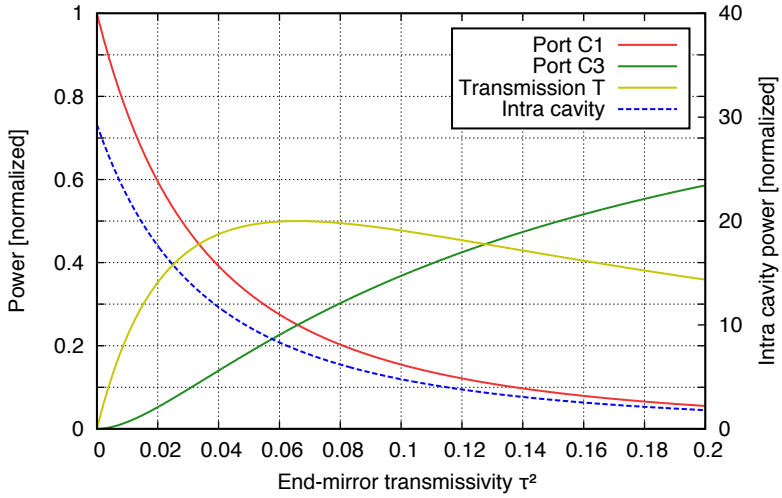

Figure 3.3.: Output characteristics of a 3-port-grating cavity with the grating characterized above as a function of the end mirror transmissivity.

3.2. Experimental setup

3.2.1. General layout

Laser preparation

The laser source was a single-mode Nd:YAG laser (non-planar ring oscillator, NPRO) operating at 1064 nm. A Faraday isolator behind the laser was implemented to protect the laser from unwanted reflections that might influence the laser performance. The laser output was transmitted through a ring mode-cleaner cavity to provide a spectrally and spatially filtered beam in the TEM_{00} mode [70]. The mode-cleaner was locked with a standard Pound-Derver-Hall locking scheme [106, 107]. Figure 3.4 shows the layout of the experiment.

Elliptical mode matching

For a given wavelength a Gaussian beam can be fully described by the size w_0 and the position z_0 of its waist. A propagating beam with the wavelength λ, the beam radius $w(z)$ with z being the distance from the waist, and the radius of curvature of

the wavefront $R(z)$ is fully described by

$$w^2(z) = w_0^2\left[1+\left(\frac{\lambda z}{\pi w_0^2}\right)^2\right], \tag{3.1}$$

$$R(z) = z\left[1+\left(\frac{\pi w_0^2}{\lambda z}\right)^2\right]. \tag{3.2}$$

Note that the beam radius is per definition the distance to the optical axis at which the amplitude of the electrical field decreases by a factor of $1/e^2$.

The eigenmode of an optical resonator is defined by the radii of curvature R_1 and R_2 of its mirrors, by the resonator length and by the wavelength used. In the mode matching procedure the beam parameters of the input beam are changed such that the wave front of the incoming beam matches the mirrors' radii of curvature. To change the beam paramters, commonly lenses are employed.

Another cavity parameter defined by the length and the mirror's curvature is the so-called g-parameter [108]. It is given by

$$g_1 = 1-\frac{L}{R_1} \quad \text{und} \quad g_2 = 1-\frac{L}{R_2}. \tag{3.3}$$

Thus the waist size of the resonator's eigenmode at the position $z=0$ is given as

$$w_0^2 = \frac{L\lambda}{\pi}\sqrt{\frac{g_1g_2(1-g_1g_2)}{(g_1+g_2-2g_1g_2)^2}} \tag{3.4}$$

The g-parameter describes the stability criterion of an optical resonator:

$$0 \le g_1g_2 \le 1. \tag{3.5}$$

A resonator fulfills the stability criterion and is *optically stable* if a paraxial beam does not leave the resonator after an arbitrary number of internal reflections [109].

The 3-port-grating cavity is a so-called half-symmetric resonator since the grating itself is flat. Consequently, the g-parameter of the grating is unity ($g_0 = 1$) and the possible length of a stable resonator is defined by the curvature of the end mirror. The position of the waist of the eigenmode is directly on the grating. The waist radius is given by

$$w_0^2 = \frac{L\lambda}{\pi}\sqrt{\frac{g_1}{1-g_1}}. \tag{3.6}$$

according to Eq. (3.4).

Diffraction at a grating at differing input and output angles leads to an elliptical shape of the diffracted beam. The grating used for the experiment has a second-order Littrow angle of $\alpha = 47.2°$ and a first diffraction order of $\beta_1 = 0°$ (for a laser wavelength of $\lambda = 1064\,\mathrm{nm}$). If a spherical cavity eigenmode is desired, the input beam needs to compensate the diffraction-induced ellipticity. Generally, for the beam radius in the x-plane/axis is "squeezed" according to

$$w_{0\mathrm{x}} = \cos(47.2°) \cdot w_{0\mathrm{y}}, \tag{3.7}$$

while the y-axis waist size $w_{0\mathrm{y}}$ is not affected. Here, $w_{0\mathrm{y}}$ is the waist size defined by the cavity parameters according to Eq. 3.6.

Setup

In Fig. 3.4 the general layout of the experiment is shown. An electro-optical modulator generated phase modulation sidebands at a frequency of 15 MHz for the Pound-Drever-Hall locking scheme used to stabilize the 3-port-grating coupled arm-cavities [99, 110]. Four cylindrical lenses were used for the mode matching procedure. The main beam splitter (BS1) had a splitting ratio of 50:50. The diffractive couplers for the arm cavities were cut from the single 3-port grating discussed in Sec. 3.1. At an identical distance to the respective forward-reflected port of each cavity, a second detection port was set up using another 50:50 beam splitter (BS2). For the detection of the arm-cavity's control signal, steering mirrors with a power transmission of $\tau^2 = 8\,\%$ were implemented in the forward-reflected ports of each cavity. The AC-gains of the two photo detectors PD1 and PD2 were carefully matched and sent to a spectrum analyzer (Type: R&S®FSP).

3.2.2. Arm cavities

The 3-port grating characterized above was split into two parts at the IAP in Jena. After the splitting the two parts where characterized again. The results are given in Table 3.2. The cavities were set up in second-order Littrow mount, the cavity length was $L = 81.5\,\mathrm{cm}$. The highly reflective end mirrors where mounted on a piezo-electric transducer (PZT) to linearly sweep the cavity length.

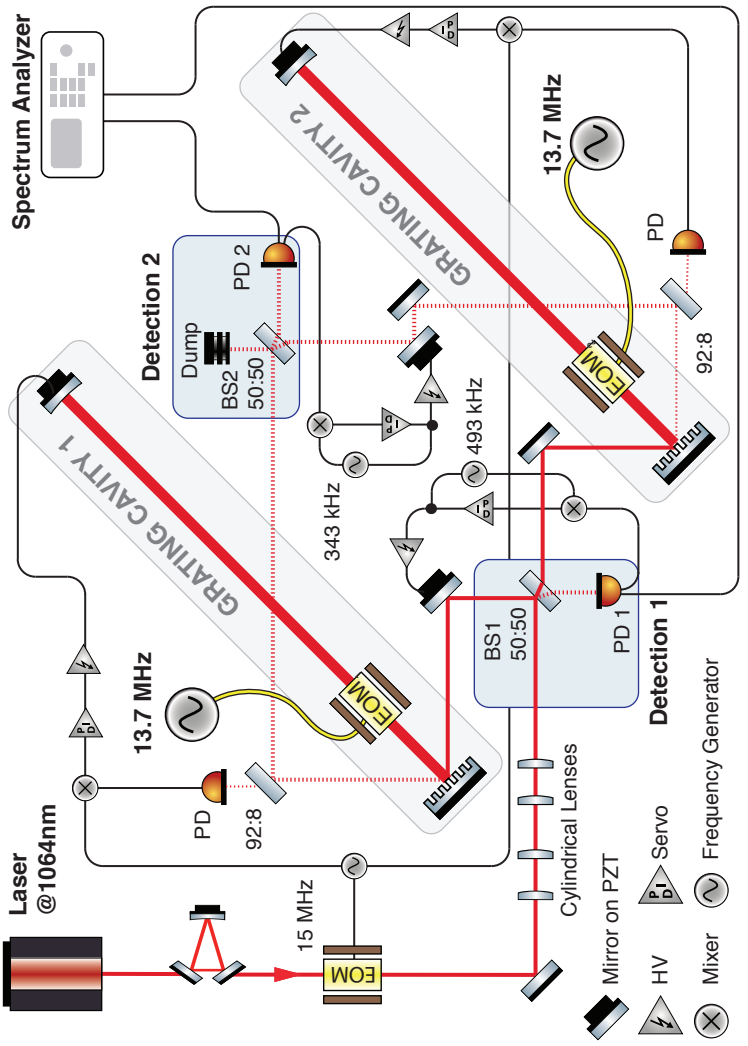

Figure 3.4.: Schematic of the experiment. The main interferometer was stabilized such that almost all carrier light was back-reflected to the laser. Thus, the main output port at PD 1was stabilized close to dark fringe. To generate phase-modulation signals in the arm cavities, two electro-optical modulators (EOMs) were used. The EOMs were driven by phase-locked frequency generators at the signal frequency of 13.7 MHz. The signals were brought to interference at the beam splitters BS1 and BS2 and recorded at the photo detectors *signal 1* and *signal 2*, respectively. The photo detector output was analyzed with a R&S®FSP spectrum analyzer.

Grating cavity characterization

When appropriately adjusting the demodulation phase of the PDH error signal, a calibration signal can be generated to determine the cavities' linewidths (FWHM) with an estimated error of $\pm 3\,\%$ [48, 78]. This is exemplarily shown for cavity 2 in Fig. 3.5. With the 15 MHz PDH-signal a cavity linewidth of 2.03 MHz was derived.

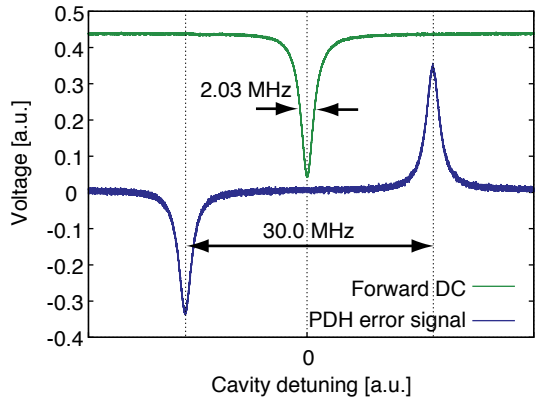

Figure 3.5.: Measurement of the cavity line width of the interferometer's arm cavity 2. The 15 MHz PDH absorption signal provides a calibration for the x-axis.

The length of the cavity can be measured with a conservatively estimated error of ± 1 mm and thus the finesse of the cavity can be calculated according to Eq. (2.38) when using the cavity linewidth derived above. For cavity 1 a finesse value of $\mathcal{F}_1 = 97.7$ and for cavity 2 a cavity finesse of $\mathcal{F}_2 = 90.8$ was derived. If the reflectivity of the end-mirror is known precisely (the HR mirror used had a specified reflectivity above $\rho_1^2 > 99.997\,\%$), the amplitude reflectivity of the grating can be determined to

$$\rho_0 = \frac{2\mathcal{F}^2 + \pi^2 - \pi\sqrt{\pi^2 + 4\mathcal{F}^2}}{2\mathcal{F}^2\rho_1}, \tag{3.8}$$

using Eq. (2.39). From this, the loss of the grating device at normal incidence can be calculated according to

$$A = 1 - (\rho_0^2 + 2\eta_1^2). \tag{3.9}$$

This measurement is preferable to a direct measurement of the grating's amplitude reflectivity, since the latter is a large value and thus will result in a *large* measurement

error. The first-order diffraction efficiency is, in contrast, a *small* value, so that the error can be significantly reduced.

Table 3.2 shows the results of the characterization of the two arm cavities. The input efficiency of cavity 2 $\eta_1^2 = 3.04\,\%$ is smaller than for cavity 1 $\eta_1^2 = 3.30\,\%$. As a consequence the linewidths and the finesse determined differ for the two arm cavities. All values agree with the measured data and the corresponding error bars of the initial substrate (see Table 3.1). Presumably, slight deviation of the diffraction characteristics is a result of the cutting process in the course of which the substrate was exposed to an increased mechanical stress [111]. Note that the homogeneity of dielectric 3-port gratings with respect to wave front distortion and diffraction characteristics is part of current investigations.

Table 3.2.: Parameters of the two grating arm cavities.

parameter	**cavity 1**	**cavity 2**
0th diffraction order (η_0^2)	96.01 ($\pm$2.30) %	96.24 ($\pm$2.30) %
1st diffraction order (η_1^2)	3.30 ($\pm$0.23) %	3.04 ($\pm$0.23) %
2nd diffraction order (η_2^2)	0.04 ($\pm$0.02) %	0.04 ($\pm$0.02) %
Grating power reflectivity (ρ_0^2)	93.20 ($\pm$0.13) %	93.67 ($\pm$0.12) %
Grating loss at normal incidence	0.20 ($\pm$0.15) %	0.25 ($\pm$0.16) %
free spectral range	183.9 ($\pm$0.3) MHz	183.9 ($\pm$0.3) MHz
FWHM (w/o EOM)	2.03 ($\pm$0.2) MHz	1.88 ($\pm$0.2) MHz
finesse (w/o EOM)	90.8 ($\pm$2.9)	97.7 ($\pm$3.0)
finesse (with EOM)	80.5 ($\pm$2.5)	86.7 ($\pm$2.8)
EOM induced loss (multipass)	0.85 ($\pm$0.23) %	0.79 ($\pm$0.21) %

EOM-induced loss

In each cavity, a broadband electro-optical-modulator was used to generate the phase modulation signal sidebands as depicted in Fig 3.4. One surface of the EOMs crystals has a wedge of 0.5° to avoid undesired reflections and subsequent parasitic cavity effects. However, the anti-reflection coatings of the EOM crystal surfaces induced

additional losses that significantly reduced the cavity finesse. The EOM-induced loss can be determined via the finesse measurement discussed in Sec. 3.2.2. Therefore, the finesse of each cavity is determined with and without EOM [105]. The obtained finesse values and the resulting EOM-induced losses are shown in Table 3.2.

Figure 3.6 summarizes the results of the characterization procedure for the two grating coupled arm cavities. As also intelligible from Fig. 3.3 the output characteristics at the two cavity ports, as well as the internal power build-up, significantly change when loss is induced. Here it does not matter wether the loss originates from an increase of the end mirror transmission or from lossy optics. For the arm cavity 1 the losses of EOM and grating sum up to $A_{\mathrm{Cav1}} = 1.10(\pm 0.39)\,\%$. Consequently, the power reflectivity that can be achieved at port C3 when taking the total loss into account is reduced to $0.74(\pm 0.07)\,\%$ [see red line in Fig. 3.6 (a)]. In analogy, the power reflectivity achievable on resonance with the second grating in cavity 2 is reduced to $0.74(\pm 0.07)\,\%$ due to the losses of $A_{\mathrm{Cav2}} = 0.99(\pm 0.35)\,\%$ as shown in Fig. 3.3 (b). Although the values of the achievable power reflectivity are similar for the two cav-

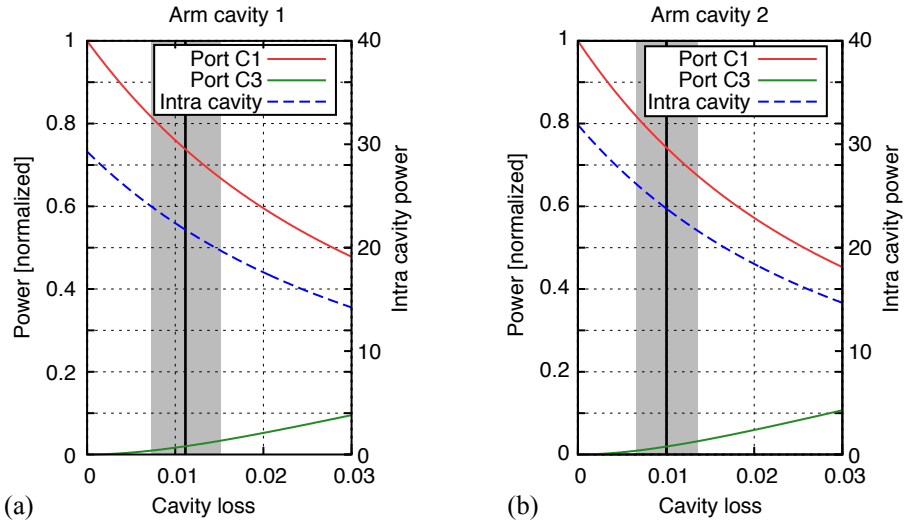

Figure 3.6.: Output characteristics and intra cavity fields of the two arm cavities depending on the optical loss induced by the grating devices and the EOMs. (a) Arm cavity 1 with an overall loss of $A_{\mathrm{Cav1}} = 1.10(\pm 0.39)\,\%$ (indicated by the horizontal black line, the error bar is given as a grey area). (b) Arm cavity 2 with overall losses of $A_{\mathrm{Cav2}} = 0.99(\pm 0.35)\,\%$

ities, the intra-cavity fields around these values of the two cavities differ due to the different input efficiencies and the resulting different power build-ups (see Fig. 3.3). Note that for all values a perfect mode matching was assumed.

Cavity mode matching and stabilization

The radii of curvature of the end mirrors $R_{\mathrm{c}} = 100\,\mathrm{cm}$ led to a targeted waist size for the vertical dimension of $w_{0\mathrm{y}} = 362.8\,\mu\mathrm{m}$ according to Eq. (3.6). This resulted in a value for the waist size of the horizontal dimension of $w_{0\mathrm{x}} = 246.5\,\mu\mathrm{m}$. A helpful tool for the mode matching procedure is the mode matching programm 'JamMt' that was developed at the AEI in Hannover [112]. For each dimension two cylindrical lenses were used that were implemented in front of the main beam splitter as depicted in Fig. 3.4.

Figures 3.7(a,b) and 3.8(a,b) present the powers that were measured at the forward and backward-reflected ports of the two grating cavities as a function of the cavity detuning Φ. For the backward-reflected port C1 the signal was detected at the main detection port of the interferometer (see Fig. 3.4). For both cavities a mode matching with a comparable quality was realized, which provided comparable power reflection values for the two cavities stabilized to resonance. Therewith a good contrasts at the detection ports was realized (see Sec. 3.2.3). Figures 3.7 (c) and 3.8 (c) show the PDH error signals detected at the forward-reflected port of each cavity using a 92:8 beam splitter (see Fig. 3.4.). The signals were fed back to the piezo-mounted end-mirror of each cavity as depicted in Fig. 3.4.

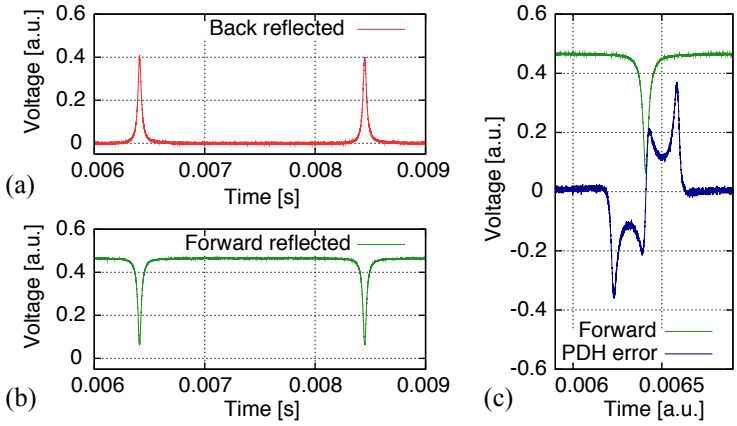

Figure 3.7.: Arm cavity 1: Outputs scanned over one FSR at the backward-reflected port (a) and forward-reflected port (b) and the PDH error signal for cavity stabilization that was detected and generated at the forward-reflected port.

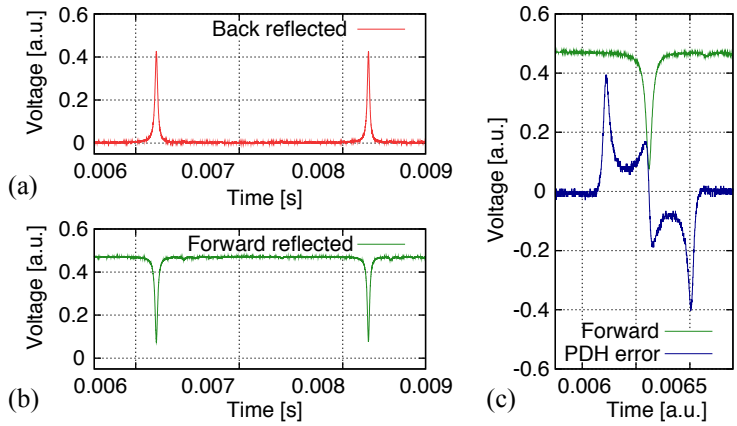

Figure 3.8.: Arm cavity 2: Outputs scanned over one FSR at the backward-reflected port (a) and forward-reflected port (b) and the PDH error signal for cavity stabilization that was detected and generated at the forward-reflected port.

3.2.3. Interferometer control

The two detection ports of the interferometer were stabilized to their operation points by using an internal modulation control scheme. For this, phase-modulation RF-sidebands were generated using a tilted mirror located in the respective detection path. The mirror was mounted on a PZT. Thus, sidebands were generated by a macroscopic displacement of the steering mirror at the frequency used. The AC-signals used were demodulated at the modulation frequency, low pass filtered and fed back to the mirror's PZTs via PID controllers (see Fig. 3.4). In this way signals were generated to stabilize the detection ports at (or close to) dark fringe. To realize a significant movement of the mirrors, sideband frequencies were chosen such that they met one of the PZT's resonance frequencies. For the detection port 1 a resonance of the PZT was found at 493 kHz and the mirror-PZT in the detection path towards detection port 2 had an appropriate resonance at 343 kHz (see Fig. 3.4). For more information on internal modulation schemes and other interferometer control schemes see Refs. [8, 113].

For a perfect contrast (equal to unity) at the main beam splitter, several conditions need to be fulfilled. The incoming beam has to be split at a perfect 50/50 ratio at the (loss-less) main beam splitter (BS1) and the reflectivity of the arm cavities has to be exactly one, which corresponds to a loss-less cavity, and additionally, to a perfect grating in $\eta_{2\mathrm{min}}$-configuration and perfect mode matching. These theoretical assumptions cannot be completely achieved in a *real* experiment. In Fig. 3.9 the contrast realized in the experiment at the main detection port is shown. Additionally the error signal generated with the internal modulation scheme at 493 kHz is depicted. A maximal visibilty of 98.7 % was achieved and the generated error signal (dark blue path in Fig. 3.9) was used to stabilize this detection port on dark fringe. Note that for a 3-port-grating cavity in second-order Littrow mount the complexity of the contrast matching procedure is automatically reduced due to the fact that the grating cavity on resonance is a mode cleaning optical device. This means that even for non-optimal mode matchings always the TEM_{00}-modes are reflected towards the beam splitter. In addition the Littrow configuration itself implies a perfect overlapping of incoming and reflected beam. Consequently, the deviations of the contrast from its optimum is due to the differing power levels that are reflected from the two resonant arm cavities.

Figure 3.10 shows the internal modulation scheme generating error signals at a side-

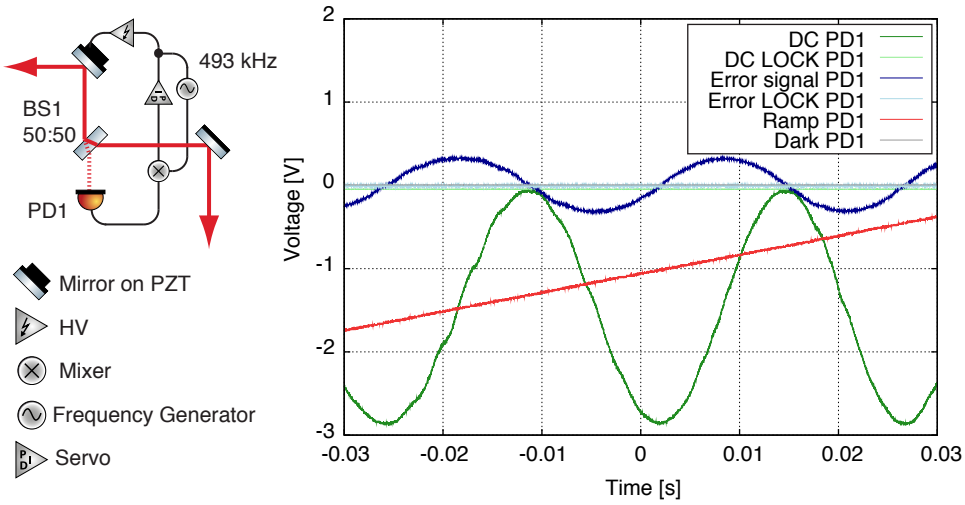

Figure 3.9.: Left: Control scheme of detection port 1 using an internal modulation scheme at 493 kHz. Right: DC signal (green) and generated error signal (blue) detected with the photo diode PD1 at detection port 1. When sweeping the interference fringes (the ramping signal is displayed in red color) a contrast of 98.7 % was measured with respect to the dark noise of the detection port (grey path). The detection port was stabilized (DC LOCK and error LOCK) on dark fringe.

band frequency of 343 kHz and signals detected at the second detection port of the interferometer. At the second beam splitter (BS2) the light fields from the forward-reflected ports of the two grating arm cavities are brought to interference (see Fig. 3.4). Thus, the light paths do not automatically match by means of beam alignment as seen in the upper case. The DC (green) and AC-signals (blue) were measured with the photodiode PD2. When scanning the relative phase at this port, a contrast of 93.7 % was measured with respect to the dark noise (grey path in Fig. 3.9). The port was stabilized on dark fringe (DC LOCK and error LOCK). Note that the contrast at this port was limited by air fluctuations as well as by the differing mode matchings of the two cavities and the subsequently differing higher order modes that are forward-reflected at port C3.

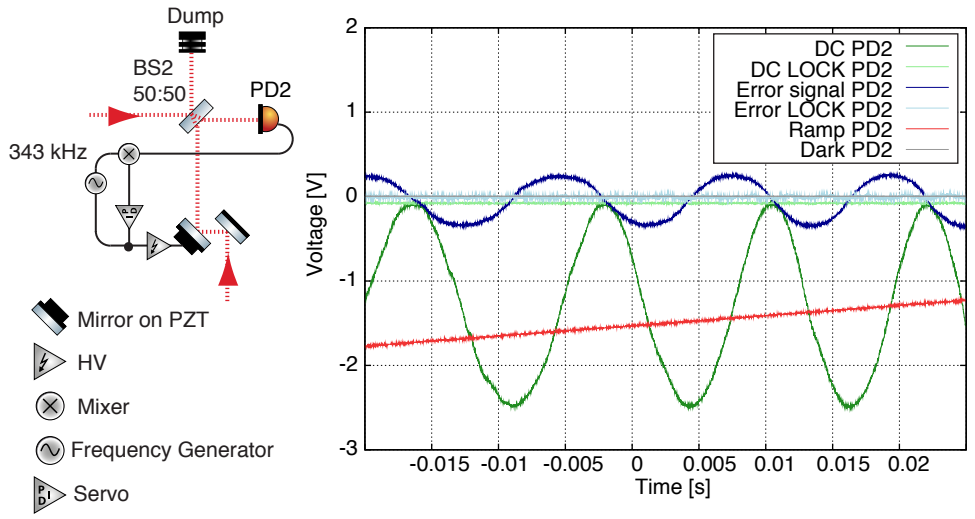

Figure 3.10.: Left: Control scheme of detection port 2 using an internal modulation scheme at 343 kHz. Right: DC signal (green) and generated error signal (blue) detected with the photo diode PD2 at detection port 2. When sweeping the interference fringes (the ramping signal is displayed in red color) a contrast of 93.7 % was measured with respect to the dark noise of the detection port (grey path). The detection port was stabilized (DC LOCK and error LOCK) on dark fringe.

3.3. Measurement procedure and discussion

For the measurement procedure the two arm cavities were stabilized to their resonance. The two detection ports were stabilized close to dark fringe so that a local oscillator beam for a self-homodyne readout scheme was available. The EOMs in the arm cavities were driven by two phase-locked signal generators, applying a modulation at 13.7 MHz.

Figure 3.11 shows the results obtained at the two signal output ports. Trace (a) shows the signal that was measured by PD1 if only EOM_1 in the grating cavity 1 was actuated. The modulation depth was adjusted to generate a signal with a peak power of -60 dBm for a resolution bandwidth of 3 Hz. An equally strong signal was produced in grating cavity 2 using EOM_2 as shown in Fig. 3.11 (b). If the EOMs were now actuated simultaneously, the phase relation of the EOM's signal generators determined the interference of the signals leaving the two arm cavities and combined

at BS1. The maximal destructive interference is realized if the two EOMs are driven in phase. The residual signal of -94 dBm is shown in trace (c). The phase relations of the signal generators were adjusted such that the differences in the electrical signal paths (cabling) were compensated.

When a phase shift of 180° was applied to one of the EOMs, the maximal constructive interference of the two signals was achieved, the results are shown in Figure 3.11 (d). As expected, the signal increased by 6 dB or a factor of four to -54 dBm. The factor of *four* is due to the fact that the two signal *amplitudes* add up coherently when the two EOMs are operated in differential mode. The signal power that is proportional to the square of the sum amplitude thus increases by a factor of 2^2.

The lower part of Figure 3.11 shows the signals measured in detection port 2. The signals generated by EOM_1 and EOM_2 were -62.4 dBm and -65.4 dBm, respectively [Fig. 3.11 (e,f)]. The signal loss with respect to port 1 was due to a combination of propagation loss and unequal electronic stabilization loops. For EOM_1 the total signal loss was 43 %, and 71 % for EOM_2. The optical propagation loss was due to the partially transmissive steering mirror required for error signal generation as well as to absorption by optical components. Furthermore, the optical path to port 2 considerably exceeded the path length to port 1, so that air perturbations had a stronger effect in terms of beam pointing fluctuations and thus manifested themselves as a fluctuating fringe visibility. The stronger loss for EOM_2 was mainly due to the PZT-mounted steering mirror in this path that led to beam pointing fluctuations. In addition, the length stabilization loop of grating cavity 2 had a lower stability than that for cavity 1.

The constructive interference of the two EOM signals in port 2 is shown in Figure 3.11 (h). The signal strength was -57.5 dBm and thus corresponded to the measurements of the single EOM signal levels [Fig. 3.11 (e,f)]. For all measurements, the shot noise level was with a value of about -125 dBm similar in the two ports, as was the dark noise with -129 dBm. The signal-to-noise ratio was limited by quantum shot noise, no technical laser noise was present at the frequencies of interest. The sum of the signals recorded in port 1 and port 2 [Figure 3.11 (d) and (h)] is by 26 % smaller than the value theoretically expected for the topology in the case that no signal loss is present. It is, however, still by 46 % larger than the signal from the signal port 1.

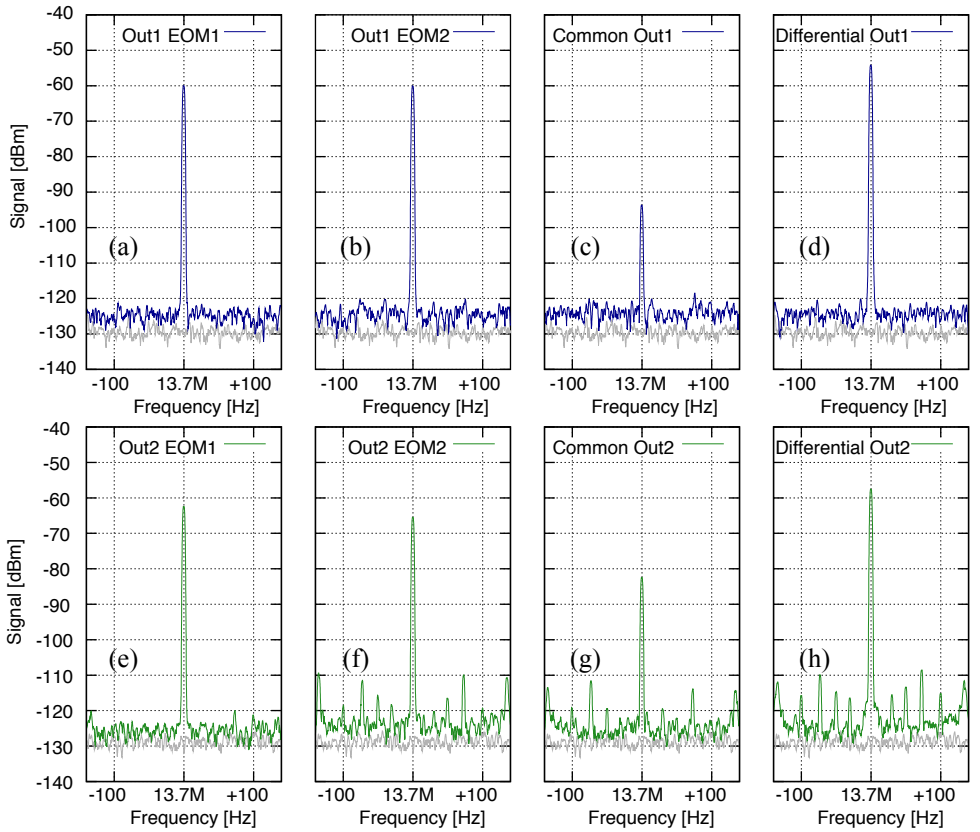

Figure 3.11.: (a,b) 13.7 MHz signal generated by $EOM_{1,2}$ and detected by PD_1. In these measurements, no signal was generated simultaneously by the second EOM. The modulation depth was adjusted to generate -60 dBm-signals. (c) EOM_1 and EOM_2 were operated simultaneously, the relative phase between the driving electric field was adjusted for maximally destructive interference. (d) same, the relative phase was shifted by $\pi/2$ to obtain maximally constructive interference. The signal amplitudes add up coherently, leading to a signal power increase by 6 dB. The grey trace shows the dark noise level. (e-h) same as (a-d), but detected by PD_2. For a discussion of signal strengths and loss see text.

3.4. Chapter summary

A Michelson-type laser interferometer with diffractively-coupled arm resonators was experimentally demonstrated. A proof-of-concept table-top experiment was set up using dielectric binary-structured three-port gratings with minimal second-order diffraction efficiency in a second-order Littrow configuration. This topology introduces a second signal output port in addition to the one in a conventional Michelson-type interferometer. The signal generated inside the arm cavities splits equally into the two ports. At the two detection ports contrast values of 98.7 % and 93.7 % were realized. The signal power was only slightly degraded by optical loss and imperfect electronic control loops. The result experimentally confirms the theoretical concept (see Sec. 2.5) of the proposed topology and its property of having the same measurement sensitivity as a single-output-port Michelson interferometer with transmissively-coupled FP arm cavities that have the same intra-cavity power.

Chapter 4

3-port gratings for optical feedback to laser diodes

This chapter presents a scheme for optical feedback to semiconductor laser diodes that is based on dielectric 3-port gratings as the coupling component to an external resonator. Such a resonator combines the frequency selectivity of an optical grating with the linewidth narrowing and the spatial mode filtering of an external cavity. Moreover, it can provide strong optical feedback to improve the optical properties of the laser diode. An introduction to the classical concepts of optical feedbacks and to the feedback regimes is given. The 3-port grating scheme is discussed. For the experimental proof of concept a high-finesse grating-cavity was setup. With optical feedback the laser threshold was decraesd. The enhancements of the output characteristics of the system that were achieved with optical feedback are presented.

4.1. Introduction

4.1.1. Optical feedback to semiconductor laser diodes

Albert Einstein's publication of the General Theory of Relativity can be seen as the starter's pistol for the race to the first direct detection of gravitational waves and the subsequently evolving gravitational wave astronomy. However, even more groundbreaking with respect to its impact on modern life is Einstein's manuscript "Zur Quan-

tentheorie der Strahlung" ("On the quantum theory of radiation") published in 1916 [1]. In this text he developed his derivation of Planck's law and the theoretical basis of the laser by describing the process of the stimulated emission as the reverse process to absorption. It took more than 40 years until Theodore Maiman opened the new era of laser phsyics by realizing the first ruby laser in 1960 [114]. Already two years later, the first diode laser was reported by Hall *et al.* [115]. Since then diode lasers have found a broad field of applications in scientific research as well as in everyday life [116]. These applications cover various fields such as telecommunications, spectroscopy or quantum information protocols [117]. Many applications require a high performance in terms of stability, spectral linewidth narrowing or tunability. For some, e. g. for experiments aiming at the reduction of quantum noise, a high purity of the longitudinal and transversal mode profile is essential. Other, more prosaic demands on the laser systems often are low cost, hand in hand with low complexity.

Optical feedback is a technique widely used to enhance the performance of laser diode systems. In this process, a part of the emitted light field is spectrally filtered by an external device and then sent back to the laser diode. First configurations implementing a compound resonator to improve the spectral characteristics of GaAs semiconductor lasers where presented in 1969 [118]. A detailed and fundamental investigation on the influence of the optical feedback on semiconductor laser properties was published in 1980 by Lang and Kobayashi [65]. In general, the optical feedback may improve the narrowing of the spectral linewidth, decrease the laser threshold, increase the stability and/or allow the tunability of the emitted laser wavelength when creating appropriate topologies.

Semiconductor diodes are suited for employment in an optical feedback scheme due to their susceptibility to optical feedback effects. They are often provided with a highly reflective coating at their back facet (R > 99 %), while the front facet has an anti-reflection (AR) coating to avoid undesired parasitic cavities that disturb the lasing process. The most obvious effects of the AR-coating is the shift of the laser threshold to much higher current values. The front facet reflectivity of uncoated diodes depends on the material used, being a function of the difference of the index of refraction of the semiconductor material and air [109]. For instance the AlGaAs semiconductors have an index of refraction of $n = 3.6$ which leads to a reflectivity of R = 32 %. Because of the high conversion efficiencies of modern semiconductor materials these reflectivities

are already sufficient to reach laser activity [116]. The broad applications and the industrial development of different types of semiconductor laser diodes has meanwhile led to the fact that diodes and subsequent laser systems are nowadays available at almost any wavelength in the VIS and near-IR band. For a well-founded introduction to semiconductor laser diodes, please see Refs. [88, 109, 119]. For a more detailed description the author refers to [120] and for a broader view on laser science itself to [121].

4.1.2. Regimes of optical feedback

Being similar to the reflectivity of the front facet, the amount of light emitted by the laser diode and then sent back by the external optical device in the optical feedback process has a severe impact on the properties of the laser system. In [122], a detailed analysis of the effect of different amounts of optical feedback was carried out. The investigation was performed with distributed feedback lasers (DFB) over a feedback range of eight orders of magnitude (–80 dB up to –8 dB). For DFB lasers, the entire resonator with the gain medium consists of a periodic structure, which favors one mode in terms of optical loss and thus leads to a single-mode emission. Other edge-emitting lasers like the ridge waveguide diodes used for this experiment have quite similar rate equations [88, 120, 123].

Regime I: Feedback below 0.01 %. Minimal effects on the emission line in terms of broadening and narrowing depending on the phase of the feedback.

Regime II: Small effects due to feedback that is still below 0.1 %. Potential multi-mode operation. Increased sensitivity to the feedback phase and to the distance to the external feedback device which induces mode hops [124].

Regime III: Strong varying of the laser threshold at feedback values around 0.1 %. Linewidth narrowing and increased stability is observable. Laser operation remains sensitive to other retro-reflections of comparable or greater magnitude.

Regime IV: At a feedback level of about 1 % satellite modes appear. This instability grows with increasing feedback factors. A broadening of the linewidth up to 50 GHz including increasing intensity noise may occur.

Regime V: Clearly stabilizing effects for a feedback factor above 10 %. The extended resonator dominates the laser operation. To reach the feedback coupling an AR-coating of the front facet is necessary. This feedback level provides stable operations on a single longitudinal mode and a narrowing of the emission linewidth that depend on the resonator characteristics.

Many of today's standardly used feedback systems utilize optical feedback levels in regime V as shown in the next section. The concept presented in this chapter provides an exceptionally strong optical feedback and can therefore clearly be attributed to regime V.

4.1.3. Classical configurations for optical feedback

The high susceptibility of laser diodes to optical feedback has led to a variety of schemes that benefit from that characteristic. Depending on the targeted application a diversity of external devices that make use of optical feedback have been developed. In general the feedback can be provided by one or several optical devices placed in front of the AR-coated front facet of the laser diode. Wicht *et al.* have given a definition of two fundamental concepts [69]. They distinguish between the term *extended resonator*, which is the extension of the optical resonator with an external and frequency selective element, and the term *external resonator*, which is an independent external optical resonator system to provide the optical feedback. This concept is commonly referred to as *diode laser with resonant optical feedback*.

Extended resonators

The principle of an extended resonator is to increase the optical path of the resonant light by introducing a reflecting device in front of the AR-coated front facet. The longer resonator increases the damping time of the intra-cavity light and thus allows for lower phase noise and a smaller emission linewidth according to Eqs. (2.38) and (2.39). An additional spectral filter inside the cavity (e.g. a diffraction grating of a rotatable etalon) further reduce the linewidth and/or act as an adjustable element to tune the emitted laser wavelength. Typical linewidths of external-cavity diode lasers are below 1 MHz [69, 88, 125].

Mode-selective etalon A widely used enhancement of the single extension of the laser diode resonator with an external mirror is the implementation of one or several etalons inside the cavity as shown in Fig. 4.1. The narrowband frequency transmission of the etalon allows a tuning of the laser frequency. The frequency range offered by of such an etalon can be varied by changing the angle of the etalon, the temperature or sometimes the gas pressure [88, 126].

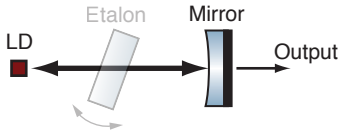

Figure 4.1.: Laser diode (LD) in an extended resonator configuration using a partially transmissive mirror in front of the AR-coated front facet of the LD. As an additional frequency-selective device, a tilted intra-cavity etalon is implemented. The narrowband transmission of the etalon provides the possibility for frequency tuning.

Littrow configuration In this concept a diffraction grating in first-order Littrow mount is used as the external device (see Fig. 4.2). The grating combines the extended cavity and the spectral selectivity in one optical device [66]. The first-order diffracted beam provides optical feedback to the laser diode while the emission wavelength can be tuned by rotating the diffraction grating. With this configuration a tunability over several tens of nanometers and a narrow linewidth of several hundreds of kHz is routinely achieved [69]. A disadvantage is that this also changes the direction of the output beam, which is inconvenient for many applications and thus requires much more complex adjustment topologies [127].

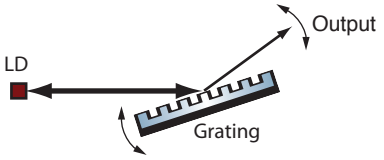

Figure 4.2.: Littrow configuration with a mode selective grating in first-order Littrow mount. The grating combines the extended cavity and the spectral selectivity in one optical device. The direction of the output beam changes when tuning the wavelength by rotating grating.

Littman configuration Figure 4.3 shows the Littman-Metcalf configuration [67]. An additional mirror reflects the first-diffraction order of the grating back to the laser diode, thus realizing an extended resonator between laser diode and the mirror. While the grating orientation is fixed, the mirror can be rotated to tune the wavelength. The diffraction at the grating occurs twice and thus better frequency resolution is realized [125]. The rotation of the additional mirror allows a tuning of the wavelength. In contrast to the Littrow configuration the angle of the output beam is constant. But since the beam reflected by the tuning mirror and then diffracted in zeroth order at the grating is unequal to the zeroth order reflection of the laser diode output, this output power is lost. Consequently the possible output power is lower than that for the Littrow configuration.

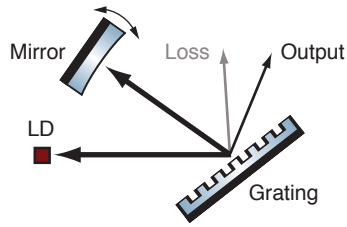

Figure 4.3.: Littman-Metcalf configuration with a fixed grating and a rotatable mirror. The frequency resolution is doubled but the beam reflected at the mirror and then diffracted in zeroth order at the grating acts as loss channel (grey arrow).

Littman-Littrow configuration Another, more sophisticated, approach uses two diffraction gratings (see Fig. 4.4). It can be seen as combination of Littman and Littrow configurations. The first grating is fixed and the wavelength tuning is achieved by the second rotatable grating. The advantage is that the frequency resolution is again doubled with respect to the Littman setup and that the angle of the output beam is constant. A disadvantage is the growing complexity and the additional loss channel introduced by the second grating.

External resonators

In Figure 4.5 approaches that use external cavities for resonant optical feedback are shown [68]. This concept, commonly referred to as *diode laser with resonant optical*

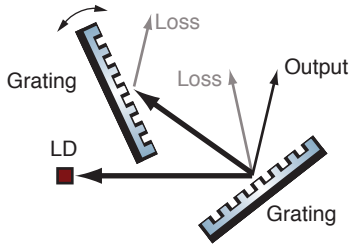

Figure 4.4.: Littman-Littrow configuration with a fixed grating and a second rotatable grating. The frequency resolution is improved but additional loss channels are introduced (grey arrow).

feedback has the advantage that the reflectivity values achievable for dielectric HR mirrors are usually orders of magnitude higher than the corresponding performance of optical gratings. Thus, a much higher optical finesse can be realized. Depending on the finesse of the external cavity and on the strength of the optical feedback, linewidths of a few kHz and tuning ranges of a few hundred MHz can be achieved [69]. Up to now, proposals to combine gratings and external resonators as shown in Fig. 4.5 (b) suffer from the disadvantage of a rather complex setup involving several optical components and thus from growing handling complexities.

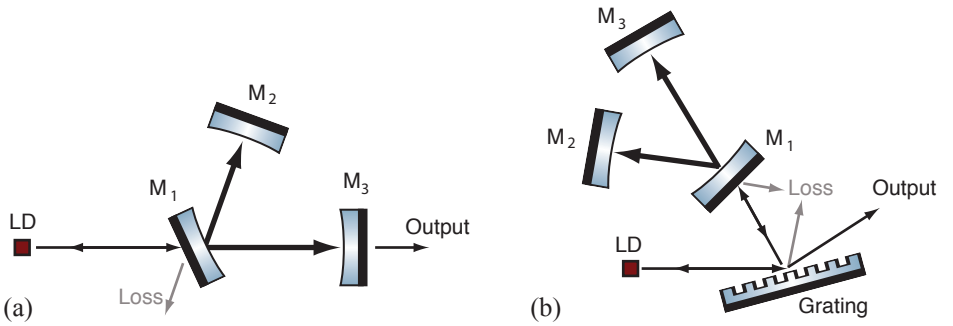

Figure 4.5.: Diode lasers with resonant optical feedback from an external cavity. (a) The (partially transmissive) mirrors M_n form a folded resonator with a considerably high finesse. (b) Combination of a Littman grating and a folded resonator. The two concepts suffer from growing complexities and loss channels (indicated by the grey arrows).

4.1.4. Concept of 3-port gratings for optical feedback

The initial application of the dielectric gratings investigated in this work and within the Hannover-Jena collaboration was the potential of all-reflective topologies for future gravitational wave detectors. This application and the required characteristics such as low loss, large substrates and very precisely controllable diffraction efficiencies, have pushed this field over the last years and initiated numerous research projects resulting in a multitude of publications and theses [50, 51, 77–79]. The profound analysis of 3-port coupled cavities has led to another potential application, which is the use as an external optical device for optical feedback to laser diodes [64]. Therein, the mode selective reflectivity of the grating cavity and the high damage threshold of dielectric materials are of interest. This might finally allow the realization of narrow-linewidth and high-finesse 3-port grating cavities that act as a mode-selective mirror.

In Fig. 4.6 the basic layout of the proposed concept is presented. This new approach for optical feedback to semiconductor laser diodes can combine the principles of an extended laser diode resonator and an external resonator by using a dielectric 3-port grating. In principle, this setup is comparable to the experiment shown in Sec. 2.3.2. Now, the power-recycling mirror is replaced by the laser diode. Thus, a system of two coupled resonators is formed where the grating is the coupling component. The first cavity is the extended cavity between the grating and the end-facet of the laser diode, while the second cavity is a 3-port-grating coupled resonator. If η_2 is small, a very high feedback factor can be reached. As seen in Chap. 2 the constructive interference at the backward-reflected port may provide a feedback factor of up to unity if the cavity is on resonance. Consequently, a stable operation in the strong feedback regime V (Sec. 4.1.2) can be reached. When allowing for a small amplitude transmission at the end mirror of the cavity, this transmission port can be used as the output port of the laser system as shown in Fig. 4.6. Thus, the external 3-port grating-coupled cavity makes it possible to yield a spectrally and spatially filtered output beam with a perfectly circular profile. In contrast to conventional concepts such a circular profile can enable the coupling to an optical fiber without additional optical loss or complex two-dimensional mode matchings. Moreover, this property is highly important for generation of squeezed light and an application e. g. in quantum information networks or laser interferometers [102, 117]. The grating cavity laser combines the laser light

source and a mode-cleaning cavity [50] in one single device providing a high-quality TEM_{00} spatial mode.

In addition to the mode cleaning properties, the high damage threshold of dielectric materials is of interest. High-finesse-resonators are realizable for very high laser output powers. Such a cavity can provide a spatially and spectrally filtered feedback field for very narrowband laser emission. Moreover, this cavity does not induce any additional loss channel known from other diode laser concepts with resonant optical feedback. Moreover, a broad window in the frequency spectrum for potential applications is accessible since laser diodes at almost any wavelength in the visible and near-infrared band are available and the electron lithography fabrication of the gratings [79] can produce 3-port gratings with different grating periods depending on the designated use of the laser wavelength.

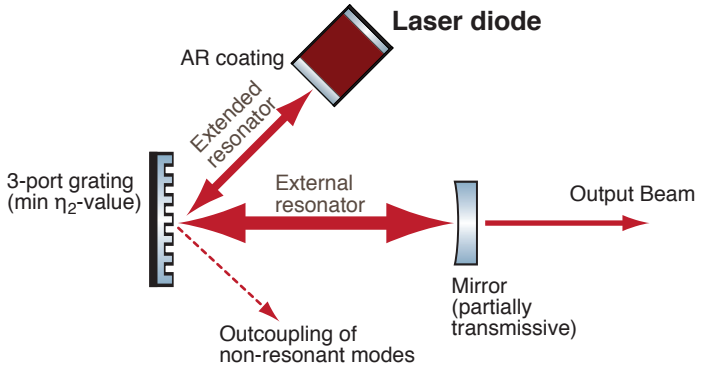

Figure 4.6.: Concept of the laser diode with optical feedback from an external 3-port-grating coupled cavity. The $\eta_{2\min}$-configuration of the grating provides strong feedback on cavity resonance. Because of the mode selective character of the grating cavity, the non-resonant modes are coupled out of the system at the forward-reflected port. The grating combines an extended and an external resonator. Because of the high damaging threshold of dielectric gratings high-finesse resonators are feasible. The end mirror has a small transmission which provides the output beam in a spatially and spectrally filtered circular output mode.

4.2. Second-order Littrow external-cavity diode laser

In this section presents the experimental realization of a laser diode with optical feedback from an external cavity with a dielectric 3-port grating. The laser diode was a commercially available ridge-waveguide laser diode with an AR coated front facet. The grating was manufactured in Jena with a first diffraction efficiency of $\eta_1^2 = 0.066\,\%$ and a corresponding minimal second-order diffraction efficiency. The external cavity that was set-up, was a 3-port-grating coupled cavity with a finesse of 1850. With optical feedback, the threshold current of the laser diode was reduced by a factor of four from 120 mA to 30 mA. The concept and the proof-of-principle results have been published in [128].

4.2.1. Laser diode and external cavity

The laser diode was a commercial single-mode ridge-waveguide GaAs laser with a maximal output power of 100 mW and an amplification profile ranging from 960 nm to 1080 nm as shown in Fig. 4.7 (a). The front facet had an AR-coating for these wavelengths. The designated central operation wavelength of the external cavity laser was 1064 nm, where the threshold pump current of the laser diode without optical feedback was about 120 mA. Figure 4.7 (b) shows a sketch of the diode housing [129].

The laser diode mount and the external grating cavity were realized as separate components (see Fig. 4.8). For temperature control, the laser diode was housed in

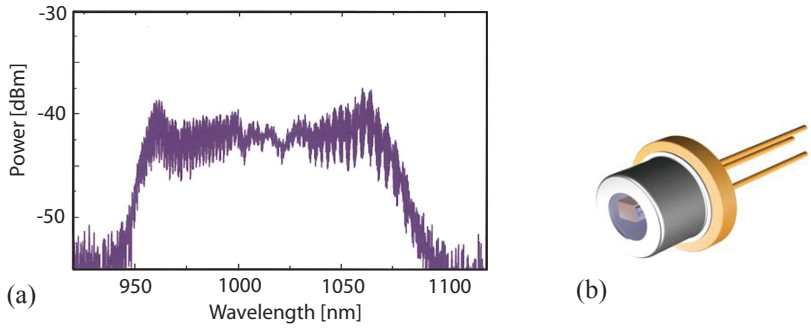

Figure 4.7.: (a) Typical amplification profile ranging from 960 nm to 1080 nm. (b) CAD drawing of the AR-coated ridge-waveguide GaAs laser diode. Source: [129]

an aluminum mount with Peltier elements attached to it. This set was mounted on a three-axis mount for beam alignment of the output beam onto the grating cavity. The output beam was transmitted through an aspheric lens with $f_{eff} = 11\,mm$ and coupled into the grating resonator via an additional alignment mirror. The grating resonator was set up as a monolithic aluminum block, aiming at a temperature stabilization in a future upgrade. The grating was housed in a flexure mount, allowing accessing the tip-tilt degrees of freedom with an increased amount of long-term alignment stability. The curved cavity end mirror ($R_c = 0.1\,m$) was glued to a ring piezo-electric transducer (PZT), thus making it possible to change the optical length of the cavity for a preliminary alignment procedure.

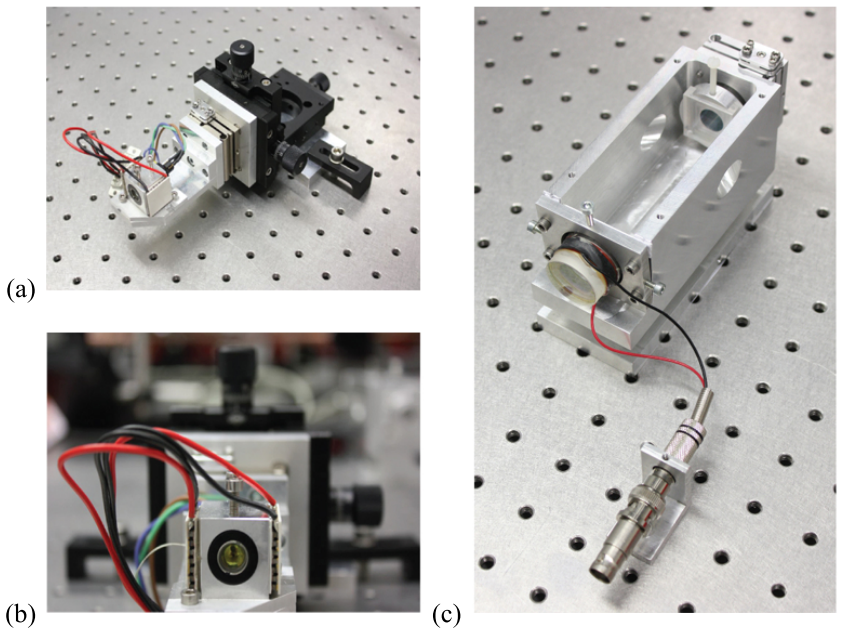

Figure 4.8.: Photographs of the laser diode and the external cavity. (a) For beam alignment, the LD was mounted onto a three-axis-mount. (b) The LD was housed in an aluminum mount. (c) The grating resonator was set up as a monolithic aluminum block. The cavity end mirror is glued to a ring PZT.

4.2.2. Grating and grating-cavity characterization

The dielectric 3-port grating was a $1'' \times 1''$ fused silica substrate manufactured at the IAP in Jena [81] with the grating structure etched in the topmost layer of a HR coating. The grating period was $d = 1450\,\text{nm}$ for a second-order Littrow angle of $\beta_2 = 47.2°$ for the used laser wavelength of 1064 nm. Figure 4.9(a) shows a photograph of the grating mounted in an aluminum holder.

For a narrowband external cavity, small coupling efficiencies are desired (see Chap. 2). Therefore the grating design process aimed at rather shallow grating groove depths to realize first-order diffraction efficiencies of $\eta_1^2 < 0.1\,\%$. In App. A.2 the ultra low-efficiency gratings manufactured in Jena and characterized in the framework of the thesis are listed. The grating chosen for the experiment had the design parameters that were a groove depth of $s = 50\,\text{nm}$ and a groove width of $g = 600\,\text{nm}$ [130]. Figure 4.9 (b) shows a scanning electron microscope (SEM) image of the grating that was finally chosen for the experiment. The fill factor realized, which is the ratio of the groove g width and the grating period d, was about $g/d = 0.485$.

To characterize the grating and the grating cavity in terms of loss and correspondingly of finesse, an independent measurement was performed employing the method already presented in Sec. 3.2.2. For this the grating was mounted in the aluminum spacer having a length of $L = 9.7\,\text{cm}$ (see Fig. 4.8). An auxiliary 1064 nm NPRO Nd:YAG laser was used to determine the diffraction efficiencies. The cavity setup in

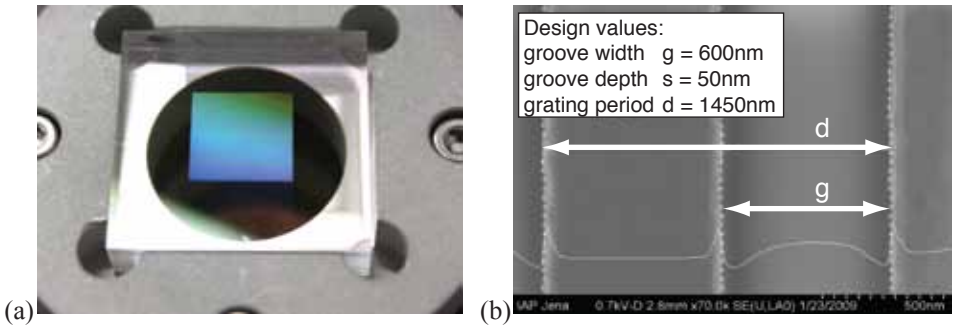

Figure 4.9.: (a) Photograph of the $1'' \times 1''$ fused silica substrate with the grating structure etched in the topmost layer of a HR coating. (b) SEM image of the grating. With the chosen design parameters a fill factor $g/d = 0.485$ was realized [130].

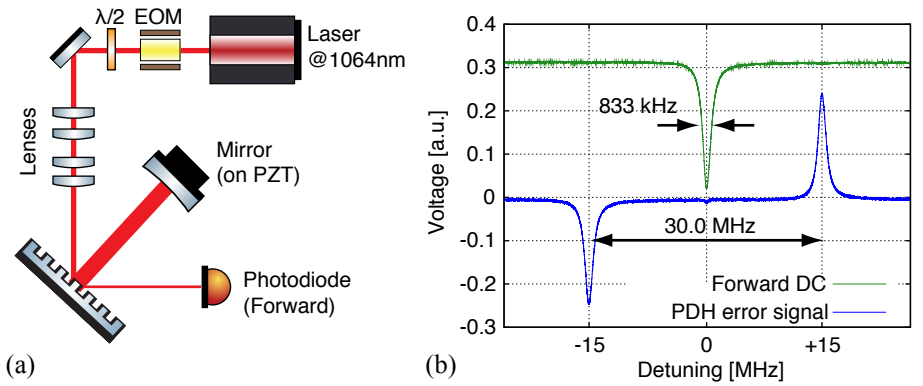

Figure 4.10.: (a) Setup for the grating characterization procedure. Laser light at a wavelength of 1064 nm was used and PDH error signals were imprinted with an EOM. Four cylindrical lenses were used for mode matching. The signals (AC,DC) were detected at the forward-reflected port. (b) DC signal and generated PDH signal at 15 MHz. The cavity had a linewidth of 833 kHz.

second-order Littrow mount is shown in Fig. 4.10(a). An EOM was used to produce PDH error signals at 15 MHz to determine the resonator linewidth. It was measured to be 833 kHz as shown in Fig. 4.10 (b).

In an independent measurement, the amplitude transmission of the end mirror was measured to $\tau_{\mathrm{M}} = 742 \pm 19$ ppm. The 1st diffraction order, being the coupling efficiency, was measured to $\eta_1^2 = 658 \pm 34$ ppm, while the second diffraction order was not measurable in the setup and thus determined to be below 10 ppm by the measurement accuracy. From the measurement of η_1^2 and the power reflectivity of the grating ρ_0^2, the theoretical boundary $\eta_{2\mathrm{min}}^2 = 0.4$ ppm can be determined [123]. The cavity parameters are summarized in Table 4.1. Note that the cavity finesse of 1855 ± 211 constitutes the highest finesse value for a 3-port-grating-coupled cavity up to now reported.

4.2.3. Experimental setup

Cavity prealignment For the cavity prealignment the grating cavity was set up in the aluminum spacer and the same NPRO laser was used (schematics of the setup shown in Fig. 4.11). The laser beam was spatially and spectrally filtered with a ring mode cleaner [70] and coupled to the cavity through the end mirror. Mode matching

Table 4.1.: Parameters of the external cavity.

Parameter	Measured value
1st diffraction order (η_1^2)	658 ($\pm$34) ppm
2nd diffraction order (η_2^2)	$<$ 10 ppm
Grating power reflectivity (ρ_0^2)	99.74 ($\pm$0.04) %
Grating loss at normal incidence	1330 ($\pm$480) ppm
End mirror transmission ($\tau_\mathbf{M}$)	742 ($\pm$19) ppm
FSR	1.55 ($\pm$0.02) GHz
FWHM	833 ($\pm$47) kHz
Finesse	1855 ($\pm$211)

was carried out with two circular lenses as shown. The end mirror was glued to a PZT that was used to linearly sweep the optical length of the cavity for the alignment procedure. Since 3-port gratings have a symmetric surface structure with respect to the grating normal, the light is coupled out of the cavity via diffraction into the plus *and* minus first diffraction order (see Fig. 4.11). Thus, when coupling light to the grating cavity through the cavity's end mirror the grating cavity has two grating output ports that provide similar output characteristics. In one of the output ports a photodiode was placed to monitor the intracavity field.

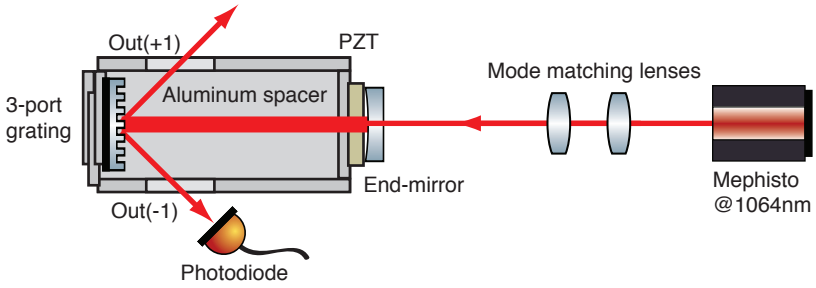

Figure 4.11.: Grating cavity prealignment with an NPRO Nd:YAG laser that was coupled through the cavity end mirror. Mode matching was carried out with circular lenses. The end mirror was glued to a ring PZT to linearly scan the cavity. A photodiode in the Out(-1)-port was used to detect the DC signal.

The result of the prealignment procedure monitored at the output port is presented in Fig. 4.12. The detuning of the external cavity over one FSR is shown.

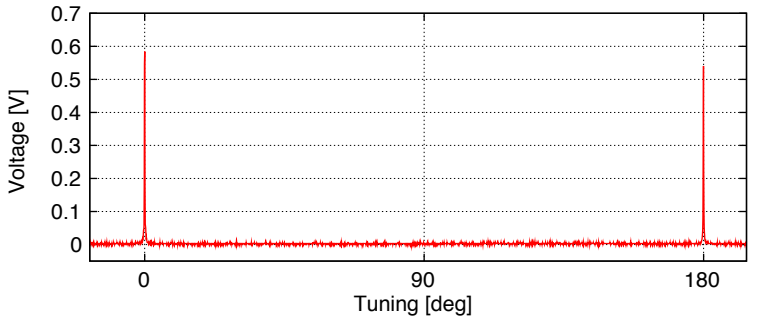

Figure 4.12.: DC signal of the photodiode placed in output port OUT(-1). The cavity is tuned over one FSR. No higher-order modes are visible within the resolution of the data aquisition system. The cavity finesse value of $1855\ (\pm 211)$ is the highest value for a 3-port-grating coupled cavity reported so far.

Experimental procedure The layout of the experiment is shown in Fig. 4.13. An additional alignment mirror was implemented to align the output beam of the laser diode onto the grating. The optical axis of the laser diode output beam that was diffracted at the grating in zeroth order and coupled out at the forward-reflected port was aligned to the optical axis that was defined by the cavity output fixed in the cavity prealignment procedure [123]. The cavity parameters (L and R_{c}) define the size of the waist w'_0 of the cavity according to Eq. (3.6) when illuminating the cavity with laser light at a wavelength of 1064 nm. Including Eq. (3.7) the required waists for vertical (x) and horizontal (y) dimensions were found to be $w'_{0\mathrm{y}} = 50\ \mu\mathrm{m}$ and $w'_{0\mathrm{y}} = 81\ \mu\mathrm{m}$, respectively. With the aspheric lens placed in front of the laser diode in x-dimension a waist of $w_{0\mathrm{x}} = 51(\pm 15)\ \mu\mathrm{m}$ at a distance of $z_{0\mathrm{x}} = 32.8(\pm 0.5)\ \mathrm{cm}$ from the laser diode's front facet was realized. Laser light that is emitted by ridge waveguide laser diodes has differing divergence angles in the two orthogonal directions (x and y) due to the dimension of the gain medium [120]. The laser diode used for the experiment x-axis divergence angle of $\theta_x \approx 30^\circ$ and a divergence angle of $\theta_y \approx 10^\circ$ of the y-axis [129]. Thus, the aspheric lens used for mode matching led to a waist in y-dimension which was considerably larger and measured to be $w_{0\mathrm{y}} = 87(\pm 15)\ \mu\mathrm{m}$

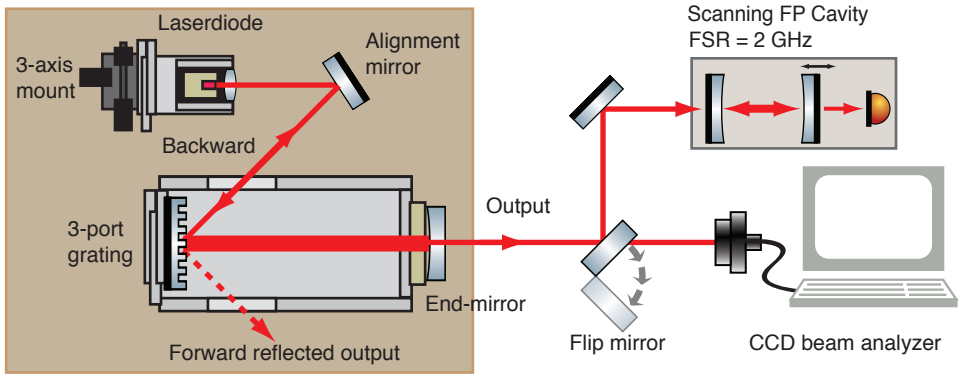

Figure 4.13.: Schematic of the external-cavity diode laser setup. The 3-axis-mount and an alignment mirror served for laser output beam alignment onto the optical axis that was defined by the prealigned resonator. The geometrical beam parameters of the diode output were adjusted with the acircular output lens in front of the diode to match the eigenmode of the grating cavity. At the output port a beam analyzer and scanning Fabry-Pérot cavity were implemented.

at a distance $z_{0y} = 33.1(\pm 0.5)$ cm from the front facet. Thus the ellipticity of the laser output can directly be used for the improvement of diode output onto the given eigenmode of the grating cavity. Nevertheless, the deviation of 15 % from the derived waist size in x dimension remained. After the aligning the overlap of prealignment-optical axis and laser diode output axis, the input laser and sinusoidal voltage to the PZT was switched off and for the characterization at the output port of the laser system a scanning Fabry-Pérot cavity and a CCD beam anaylzer were used (see Fig. 4.13).

4.2.4. Results

Decreasing the laser threshold

For power measurements, a power meter was placed in the output port. The decreased laser threshold of the diode due to the optical feedback of the external cavity was directly measurable. At the wavelength of 1064 nm, the threshold current was reduced from 120 mA in the case of a free-running laser diode to 30 mA using the optical feedback. The laser diode temperature was stabilized to 25°C. The slope efficiency was 0.018W/A.

The mode overlap between the output mode of the laser diode and the cavity eigenmode that was theoretically possible due to the restrictions described above was about 85 %. Because in the experiment no degree of freedom was present to actually characterize and thus to optimize the mode matching, this theoretical (upper) boundary was not reached. For optimization, the power output was monitored and maximized. The fact that the output at the forward-reflected port was by a factor 10 to 25 higher than the one at the outcoupling port shows the limitations of the applied procedure.

Although the grating is designed and optimized for a wavelength of 1064 nm, by changing the angle of the alignment mirror (see Fig. 4.13), the wavelength of the output beam could be tuned. The threshold value was found to be similarly reduced for wavelengths in the range from 1003 nm to 1064 nm. In Fig. 4.14 the measurements for several wavelengths, and respectively, input angles of the laser diode beam to the cavity, are shown. The best slope efficiency was realized for a wavelength of 1018 nm. Since the grating structure (defining the diffraction efficiencies) and the end mirror (in particular the HR-coating) were designed for a wavelength of 1064 nm, at this value high reflectivities, low-coupling efficiencies and a high-finesse value is realized. Thus, because of the non-optimal mode matching a lower power build-up inside the cavity and a resulting lower output power was achieved.

With two polarizing beam splitters also placed in the output port the polarization

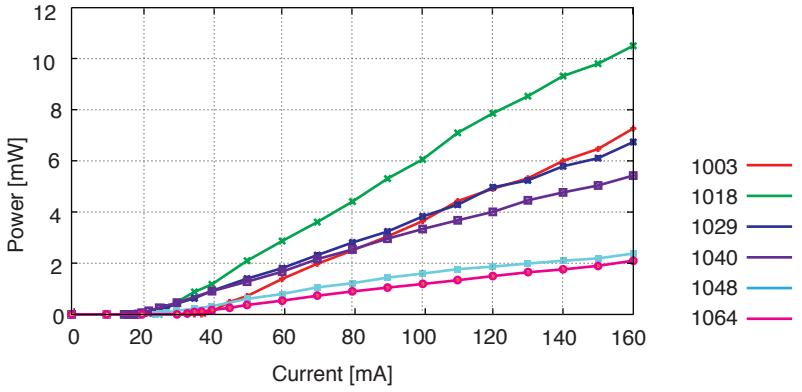

Figure 4.14.: Using the alignment mirror between LD and cavity, laser emission at the cavity output port was realized for different wavelengths. The threshold value was similarly reduced for wavelengths in the range from 1003 nm to 1064 nm

purity of the laser output was measured. The output beam was linearly polarized and the light power ratio of $P_{\mathrm{s-pol}} : P_{\mathrm{p-pol}}$ was measured to be >1000 : 1.

Circular beam profile

As shown in Fig. 4.13, a CCD beam analyzer (Type: Spiricon LBA-USB-SP620) was placed in the output port to evaluate the quality of the beam transmitted through the end mirror of the grating cavity. Figure 4.15 shows the profile of the TEM_{00} mode and a cross-section of the profile's width in the major and minor beam axis. A rotationally symmetric beam profile at the output port, being a consequence of the circular eigenmode of the grating cavity, was realized. Note that any deviations in Fig. 4.15 (b) are due to the measurement apparatus. Thus, the shown results shown mark a lower boundary for the mode quality of the laser that was achievable with the proof of concept layout.

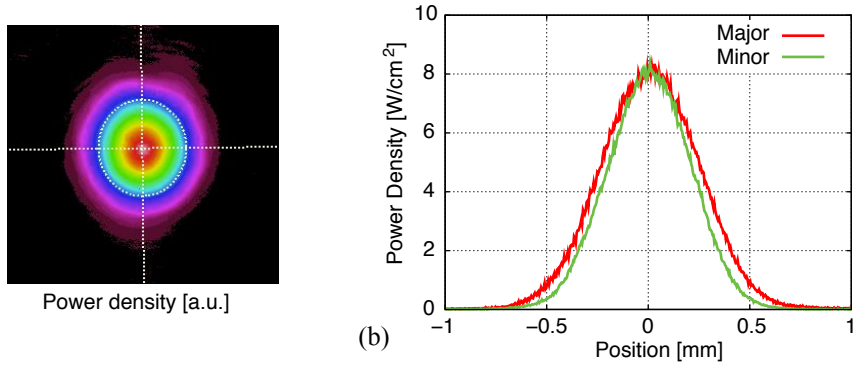

Figure 4.15.: (a) Output beam at the transmission port of the cavity end mirror detected and visualized with a CCD beam analyzer. (b) The major and minor profiles are slightly different due to the beam analyzer apparatus.

Figure 4.16 shows another evaluation of the circular output beam profile. In Fig. 4.16(a) a 3D-shot of the beam profile is shown. The cross-section of the beam profile's width is shown in 4.16 (b) along the major axis of the power density of the profile. The corresponding regression curve revealed a correlation of 97.3 %. This value was also limitted by the measument apparatus of the beam analyzer and a possibly tilted setup of the CCD camera with respect to the optical axis. Within the resolution of the CCD

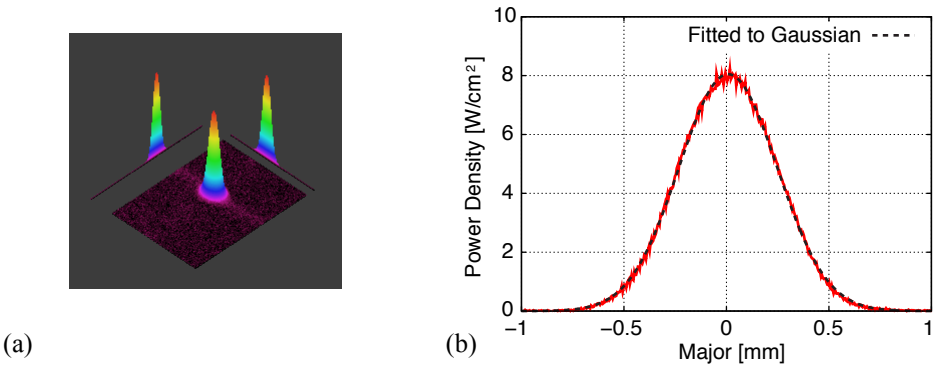

Figure 4.16.: (a) Output beam at Port T detected and visualized with a CCD beam analyzer. (b) The gaussian fit to the major beam width revealed a value of 97.3 %.

beam analyzer no higher-order transversal modes were visible.

Longitudinal single-mode operation

The scanning Fabry-Pérot interferometer, shown in Fig. 4.13, was used to verify that with the implementation of the 3-port-grating cavity no additional higher-order modes were generated and a longitudinal single-mode operation of the laser diode with optical feedback was realized. The Fabry-Pérot interferometer used (type: Toptica Photonics FPI 100) was a piezoelectrically scanned confocal FP interferometer with a resulting free spectral range of 2 GHz [123]. Note that for a confocal cavity the degeneration of higher-order transversal modes allows an investigation of the higher-order longitudinal modes of the output beam of the laser system without an extensive mode matching procedure [131].

Figure 4.17 presents the results obtained for two different cases. The case of a strongly misaligned external grating cavity is shown over several FSRs of the scanning FP interferometer in Fig. 4.17(a). Here, the misalignment allows two different longitudinal modes to be resonant in the cavity. They show frequency difference of one or several free spectral ranges of the external cavity which is 1.5 GHz (see Table 3.2). Figure 4.17 (b) shows the operation of the laser system with a properly aligned external cavity, comparable to the prealigned cavity shown in Fig. 4.12. No higher-order longitudinal modes were observable within the resolution of the oscilloscope used for

data acquisition. The small peaks that are visible in the trace of 4.17 (b) could be traced back to electronic artefacts of the data acquisition system.

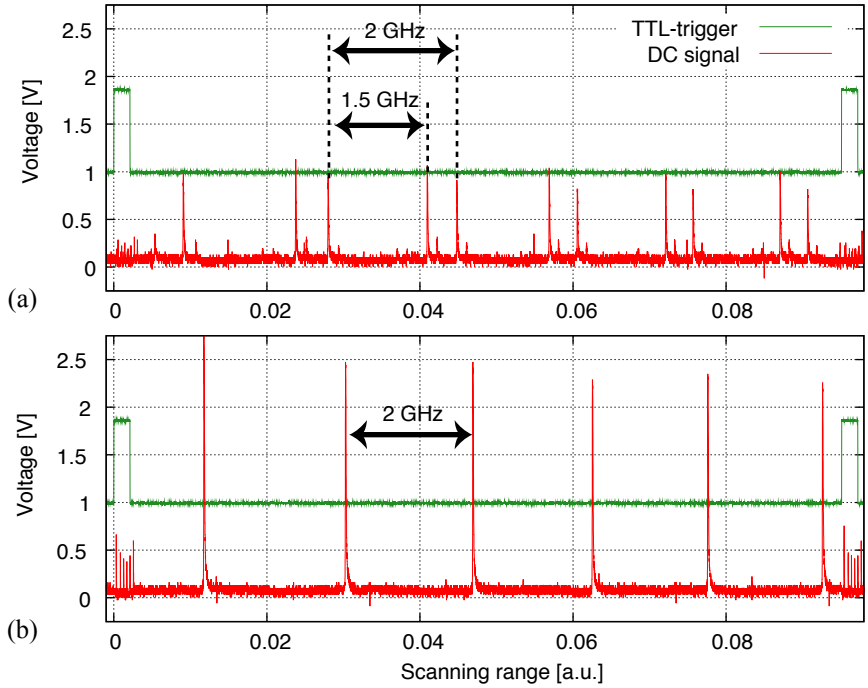

Figure 4.17.: Laser system operating in fundamental condition (b) and in an operation condition where several longitudinal modes are resonant in the external cavity at a minimal frequency difference of 1.5 GHz (the FSR of the external grating cavity) and therefore induce a degeneration in laser operation (b). The results were obtained with a confocal scanning Fabry-Pérot interferometer with having a free spectral range of 2 GHz.

4.3. Conclusion

An external-cavity diode laser in second-order Littrow configuration was demonstrated. This concept combines the benefits of an external narrow-linewidth cavity with the frequency-selectivity of a grating. In particular it makes use of the optical properties of dielectric 3-port gratings as all-reflective cavity couplers and of the increase in grating fabricational skills over the last decade. A cavity with a 3-port grating that has

a small η_2-value, can be seen as a mode-selective mirror that provides strong optical feedback to the laser diode a particular wavelength. The high damage threshold of dielectric materials and the precisely controllable diffraction characteristics of today's diffractive gratings allow the realization of high-power and narrow-linewidth external resonators for optical feedback applications. In the experimental investigations presented here a high-finesse external cavity with $\mathcal{F} = 1855$ was realized using a 3-port grating with a shallow grating-on-top structure and a measured optical loss of $1330\,(\pm 480)$ ppm at normal incidence. With optical feedback the threshold current of the laser diode was reduced by a factor of four from 120 mA to 30 mA. The output power was limited by the intra-cavity loss and the non-optimal mode-matching of the laser diode output beam to the eigenmode of the external grating cavity. A key-feature of the proposed concept was the mode-cleaning ability of the 3-port grating cavity. A high spatial TEM_{00} mode content together with a high polarization purity was achieved.

Chapter 5

Summary and outlook

Within the framework of this thesis two applications that employ a dielectric all-reflective 3-port diffraction grating as the coupling component to an optical resonator were theoretically investigated and experimentally demonstrated.

Laser interferometric gravitational wave (GW) detectors utilize optical resonators to increase the amount of light power stored in the arms of the interferometer. Diffraction gratings have been proposed as all-reflective alternatives for future GW observatories because they permit the increase of circulating light power and hence the improvement of the shot-noise limited sensitivity without being limited by thermal effects in the (partially) transmissive substrates. In the context of this work, a Michelson-type interferometer with diffractively-coupled arm resonators was investigated. In Chap. 2, the signal response of 3-port-grating cavities was presented for phase modulation signals generated inside the cavity in analogy to the effect of a GW. It was theoretically shown that a 3-port-grating coupled cavity can be employed as the arm cavity of an interferometer without losing signal when detecting at both output ports of the cavity.

In Chap. 3, the experimental demonstration of this proposal was presented. This topology introduces a second detection port where the light paths from the forward-reflected ports of the cavities interfere. Two custom made similar dielectric gratings with a minimal second-order diffraction efficiency were used. Due to grating inhomogeneities, the two arm cavities had slightly different finesse values of 91 and 98, respectively. Phase modulation signals were generated inside the arm resonators us-

ing electro-optical modulators and subsequently detected at the two signal ports. A contrast of 98.7 % and 93.7 % was realized at these ports. The strength of the signals was limited by optical loss and imperfect electronic loops. However, the sum of the signals was still larger by 46 % than the signal from the signal detection port at the main beam splitter. Thus, the theoretical concept was confirmed. Taking into account optical loss and experimental restrictions, it was shown that in principle the same measurement sensitivity can be reached with this multi-port topology compared to the linear arm cavities of a single-output-port Michelson interferometer, assuming equal power build-ups inside the grating arm cavities.

In Chap. 4, a diode laser system employing optical feedback from an external 3-port-grating coupled cavity was proposed and demonstrated. This new concept combines the benefits of an external narrow-linewidth cavity with the frequency-selectivity of a grating. A key feature of the external-cavity diode laser is a high spatial TEM_{00} mode content due to the mode-cleaning ability of the optical cavity, making it a laser with an inherent mode-cleaning device. The 3-port grating used, had very low first- and second diffraction order efficiencies of $\eta_1^2 = 658(\pm 34)$ ppm and $\eta_2^2 < 10$ ppm, respectively. The measured cavity finesse was $\mathcal{F} = 1855$, being the highest value ever reported for a 3-port-grating coupled cavity. With optical feedback the threshold current of the laser diode was reduced by a factor of four from 120 mA to 30 mA. Further features were a high polarization purity as well as a potential tuning range extending over several GHz (using the piezo-actuator attached to the cavity end mirror).

The high damage threshold of dielectric materials makes the use 3-port gratings as key components for external cavities a promising approach to provide optical feedback to high-power applications and to multi-mode laser diodes. Thus, the mode-cleaning feature of 3-port-grating cavities and their potential narrow linewidth may allow access to high power outputs *and* high optical beam qualities of laser diodes at any wavelength where appropriate semiconductor laser diodes are available. This, along with a comparatively low complexity and correspondingly low cost, makes the 3-port grating cavity a promising device for optical feedback applications.

Before dielectric gratings can be employed as key components in GW observatories, the high demands of future detectors will continue to push further developments in this research field. Further investigations of optical loss channels are necessary. The opti-

cal properties of gratings have been improved step by step over the past years due to improving etching techniques and new electron beam lithography (EBL) instruments [74, 79]. The new EBL facility recently commissioned at the IAP in Jena [81] enables the production of 3-port gratings with shallow but more accurately shaped grating-on-top structures for potential low-scattering gratings. The grating presented in Chap. 4, with an optical loss of $1330(\pm 480)$ ppm at normal incidence, was processed in this facility. Further improvements in optical loss are required to provide diffractive optics that may also be capable for the use of squeezed states of light, which has become a technology routinely accessible for use in future detectors [133]. Moreover, with this EBL facility a dielectric 3-port grating on a $9'' \times 9''$ substrate has already been realized. Large-scale optics are essential for future GW detectors.

An open question that needs to be solved in the future is the consequence of additional degrees of freedom that are introduced by diffraction gratings. Lateral displacement has been identified as a noise source in grating interferometers [49]. It was, however, shown that the transversal effects are still below an equivalent longitudinal displacement which is not a grating-specific noise source [134]. Future investigations will have to reveal the consequences for the sensitivities of all-reflective interferometers and thus the demands for the choice of mechanical and optical schemes.

The use of diffractive optics, as presented in this thesis, can avoid any thermal effects that are associated with a residual absorption in the substrate materials. Moreover, reflection gratings enable the use of substrate materials that are less transmissive or even opaque for the laser wavelength used, but offer favorable mechanical and thermal properties. However, the multilayer coatings used to realize high reflectivities of dielectric mirrors have been identified as a dominant noise source in GW detectors. Such coatings are also applied to diffractive optics for a highly reflective surface. *Resonant waveguide gratings* have been studied as coating-reduced or even coating-free alternatives to conventional highly reflective mirrors. Current investigations are aiming at an application of this technology to dielectric diffraction gratings [62].

This work has demonstrated all-reflective replacements of optical key components in Michelson-type interferometers. These results, and a combination of all-reflective concepts with resonant waveguide technologies, can in the future be expected to clear the way for an all-reflective *and* coating-free interferometry.

Appendix A

Characterization of 3-port gratings

In the framework of this thesis, several dielectric gratings manufactured at the Institute of Applied Physics in Jena [81] were characterized with different setups. Here, the obtained results by means of optical properties are provided. All gratings are 3-port diffraction gratings designed for a center wavelength of 1064 nm with a grating period of 1450 nm for the resulting second-order Littrow angle of $\alpha_{\mathrm{in}} = 47.2°$. For further information about of the manufacturing process, the substrate and coating materials and their characteristics see [77, 79].

A.1. 3-port gratings G0.035_x

For the Michelson interferometer with 3-port-grating arm cavities, presented in Chap. 3 three gratings were manufactured in Jena, aiming at a first-order diffraction efficiency of $\eta_1^2 = 3.5\%$ for s-polarized light. The gratings were mounted with the grating ridges pointing in vertical direction in respect to the table surface. The incident light power provided by an NPRO Nd:YAG laser operating at a wavelength of 1064 nm was about 104 mW. The diffraction efficiencies at normal incidence and at second-order Littrow incidence (see Fig. 3.2) were measured with a power meter. The results for the three gratings are shown in Table A.1 for the second-order Littrow setup and in Table A.2 for normal incidence including the residual transmission.

The grating finally chosen for the experiment was grating $\mathrm{G0.035_3}$, providing the

Table A.1.: Measured diffraction efficiencies at second-order Littrow incidence.

Grating	η_0^2 [%]	η_1^2 [%]	η_2^2 [%]
$G0.035_1$	95.41 ($\pm$2.3)	4.17 ($\pm$0.26)	0.22 ($\pm$0.02)
$G0.035_2$	96.24 ($\pm$2.3)	4.22 ($\pm$0.26)	0.25 ($\pm$0.02)
$G0.035_3$	96.41 ($\pm$2.3)	3.30 ($\pm$0.23)	0.04 ($\pm$0.02)

Table A.2.: Measured diffraction efficiencies and residual transmission at normal incidence.

Grating	η_{-1}^2 [%]	η_{+1}^2 [%]	τ_0^2 [ppm]
$G0.035_1$	4.05 ($\pm$0.30)	4.20 ($\pm$0.31)	37.8 ($\pm$3.8)
$G0.035_2$	4.43 ($\pm$0.33)	4.37 ($\pm$0.33)	26.4 ($\pm$2.6)
$G0.035_3$	3.53 ($\pm$0.26)	3.52 ($\pm$0.26)	20.7 ($\pm$2.1)

lowest transmission, similar values for the first-order diffraction efficiencies at normal incidence, and a second order diffraction efficiency very close to the theoretical minimal value $\eta_{2\min}$ which suggests a low influence of the applied grating structure on the reflectivity of the multilayer coating. After the first characterization, $G0.035_3$ was split into two parts at the IAP in Jena and the two parts where characterized again. The results are given in Table 3.2.

A.2. 3-port gratings with very low first-order diffraction efficiency

Several dielectric 3-port gratings with very low first-order diffraction efficiencies were characterized in view of the use in high-finesse grating cavities. The initial substrate was a $6'' \times 6'' \times 0.25''$ fused silica substrate with an multilayer coating of 18 double layers (Manufacturer: Tafelmaier [132]). The coating was optimized for an angle of incidence of 30°and consist of 36 alternating layers of SiO_2 with a specified thickness of 191 nm, and Ta_2O_5 with a thickness of 125 nm providing a (simulated) power reflectivity of $r > 99.999\,\%$ [130]. The considerably shallow grating structures were etched in the additional top layer of SiO_2 that had a thickness of 75 nm. Five of the

gratings were designed with a groove depth of 20 nm and seven of the gratings had a design groove depth of 50 nm. Figure A.1 shows a photograph of the gratings after the EBL-process. The initial $6'' \times 6''$ substrate was cut into 25 $1'' \times 1''$ gratings.

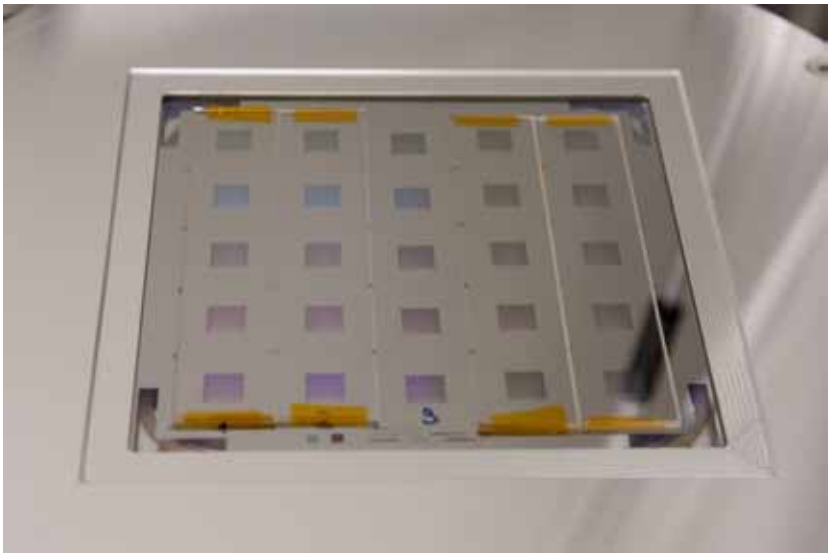

Figure A.1.: Photograph of the gratings after the EBL-process. The initial $6'' \times 6''$ substrate was cut into 25 $1'' \times 1''$ gratings. Credits: [81]

Twelve of the gratings were investigated with respect to their first-order diffraction efficiency η_1^2. For this, they were mounted in second-order Littrow configuration. The diffraction efficiencies were measured for a wavelength of 1064 nm for s and p-polarized laser light with a power meter, leading to a measurement uncertainty of $\pm 5\,\%$, are shown in Table A.3. The nomenclature used for the gratings is chosen such that grating G450_20_1 denotes a dielectric 3-port grating with a design groove width of 450 nm and a design groove depth of 20 nm. The last number denotes the counting number of the grating since several gratings with equal parameters were manufactured. The grating G600_50_1 was used for the proof-of-concept experiment presented in Chap. 4. An SEM-image of this grating is shown in Fig. 4.9 (b).

Table A.3.: 3-port gratings with low efficiency first-order diffraction efficiency

Grating	Pol.	η_1^2 [%]	η_2^2 [%]	**Grating**	Pol.	η_1^2 [%]	η_2^2 [%]
G450_20_1	s	0.021	0.000	G450_50_2	s	0.055	0.002
	p	0.016	0.001		p	0.033	0.056
G550_20_1	s	0.020	0.001	G550_50_1	s	0.038	0.003
	p	0.013	0.003		p	0.017	0.018
G600_20_1	s	0.023	0.000	G550_50_2	s	0.026	0.001
	p	0.016	0.001		p	0.007	0.028
G600_20_2	s	0.021	0.000	G600_50_1	s	0.069	0.001
	p	0.011	0.001		p	0.040	0.009
G650_20_1	s	0.032	0.000	G600_50_2	s	0.064	0.001
	p	0.021	0.000		p	0.037	0.008
G450_50_1	s	0.026	0.000	G600_50_3	s	0.059	0.001
	p	0.011	0.000		p	0.032	0.044

A.3. High-finesse 3-port grating cavities

The gratings listed in Table A.3 are expected to exhibit an optical loss similar to the grating G600_50_1 since they were cut from the same initial substrate and originated from the same EBL and etching run. These gratings thus may be used as cavity couplers to realize high-finesse cavities. Figure A.2 shows calculated finesse values that are achievable with 3-port gratings having an optical loss below 0.20 % (as already shown for grating G600_50_1) and first-order diffraction efficiencies of $\eta_1^2 < 0.025\,\%$.

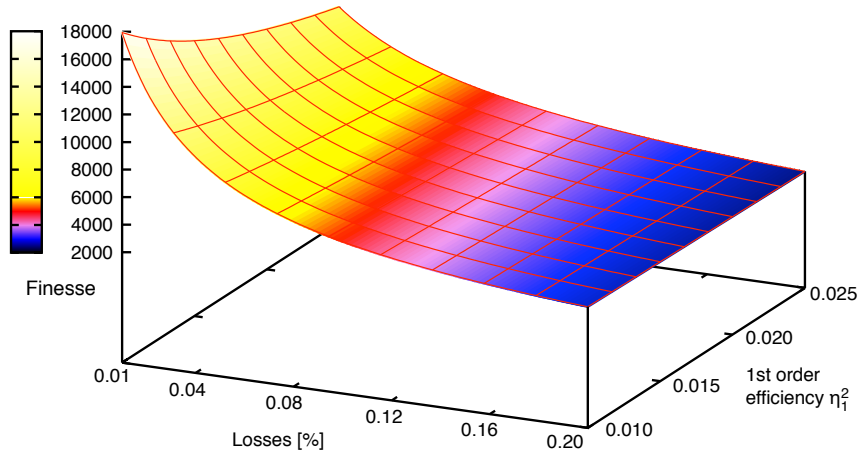

Figure A.2.: Calculated finesse of a 3-port grating coupled cavity as a function of the cavity loss (including end mirror transmission) and the first-order diffraction efficiency η_1^2 as the cavity coupling efficiency.

A.4. List of characterized 3-port gratings

For the sake of completeness, a list of all further 3-port gratings characterized in the framework of this thesis is given in Table A.4. Some of the optics were implemented in an optical cavity to measure the cavity finesse $\mathcal{F}$ using an end mirror that with a radius curvature of $R_c = 50\,\mathrm{cm}$ and a residual transmission of $\tau_1^2 = 300(\pm 30)\,\mathrm{ppm}$. Estimated values for the optical loss and for the reflectivity at normal incidence (ρ_0^2) were derived from this cavity measurements. The measurements of the diffraction efficiencies were performed with a power meter, leading to a measurement uncertainty of $\pm 5\,\%$.

The following gratings were more precisely characterized in the context of their experimental application. The grating GEO65 was used for an experiment in which the applicability of a PDH locking scheme for 3-port-grating cavities with strongly asymmetric resonance profiles were verified [110]. Grating GEO42 was used in a grating cavity with power-recycling [94]. Grating GEO67 was implemented in the suspended cavity experiment in the Glasgow 10 m interferometer facility [134, 135].

Table A.4.: Measured optical properties of dielectric 3-port gratings

Grating	Pol.	η_0^2 [%]	η_1^2 [%]	η_2^2 [%]	$\mathcal{F}$	ρ_0^2 [%]	Loss [%]
GEO41	s	97.84	1.39	0.023	212.2	97.11	0.11
	p	98.14	0.078	0.00	1742.1	99.67	0.17
GEO42	s	92.16	6.01	0.096	48.6	87.90	0.10
	p	97.39	1.89	0.13	160.3	96.19	0.03
GEO43	s	92.84	5.13	0.115	54.0	89.04	0.70
	p	94.78	1.47	0.21	177.3	96.54	0.51
GEO51	s	68.76	13.22	16.99	–	–	–
	p	92.92	1.93	2.23	–	–	–
GEO52	s	64.06	12.50	21.89	–	–	–
	p	91.59	1.73	1.96	–	–	–
GEO54	s	94.41	2.74	0.367	37.7	84.69	9.82
	p	82.65	8.61	2.92	31.0	81.70	1.08
GEO55	s	97.61	2.29	0.23	56.4	89.49	5.93
	p	81.96	8.93	2.74	23.2	76.35	5.79
GEO59	s	93.38	4.93	0.64	47.5	87.65	2.49
	p	76.20	13.15	3.60	19.85	72.91	1.09
GEO64	s	81.08	6.25	11.83	–	–	–
GEO65	s	78.24	1.71	19.47	172.5	96.45	0.13
	p	96.35	0.12	0.71	1213.6	99.51	0.25
GEO66	s	33.06	7.22	57.89	–	–	–
GEO67	s	99.560	0.077	0.018	1714	99.669	0.182
	p	99.690	0.201	0.078	762	99.209	0.389
GEO68	s	99.91	0.02	0.002	983	99.39	0.57
GEO18a_3	s	–	0.15	–	1105	99.46	0.24

Bibliography

[1] A. Einstein, *"Zur Quantentheorie der Strahlung,"* Physikalische Gesellschaft Zürich **18**, 47–62 (1916).

[2] A. Einstein, *"Approximative integration of the field equations of gravitation,"* Sitzungsber. Preuss. Akad. Wiss. Berlin, 688 (1916).

[3] A. Einstein, *"On gravitational waves,"* Sitzungsber. Preuss. Akad. Wiss. Berlin, 154 (1918).

[4] P. Aufmuth and K. Danzmann, *"Gravitational wave detectors,"* New Jour. Phys. **7**, 202 (2005).

[5] B. F. Schutz, *"A first course in General Relativity,"* Cambridge University Press, Cambridge 2009.

[6] P. Saulson, *"Fundamentals of interferometric gravitational wave detectors,"* World Scientific, Singapore 1994.

[7] D. G. Blair, L. Ju, C. Zhao and E. J. Howell (editors), *"Advanced gravitational wave detectors,"* Cambridge University Press (2012).

[8] J. Mizuno, *"Comparison of optical configurations for laser-interferometric gravitational-wave detectors,"* Internal report MPQ **203** (1995).

[9] R. A. Hulse, *"The discovery of the binary pulsar (PSR 1913+16),"* Rev. Mod. Phys. **66**, 699 (1994).

[10] J. H. Taylor, *"Binary Pulsars and relativistic gravity,"* Rev. Mod. Phys. **66**, 711 (1994).

[11] C. D. Ott, *"Probing the core-collapse supernova mechanism with gravitational wave,"* Class. Quantum Grav. **26**, 204015 (2009).

[12] J. Weber , *"Evidence for discovery of Gravitational Radiation,"* Phys. Rev. Lett. **22**, 1320 (1969).

[13] J. L. Levine and R. L. Garwin, *"Absence of Gravity-Wave signals in a Bar at 1695 Hz,"* Phys. Rev. Lett. **31**, 173 (1973).

[14] J. A. Tyson, *"Null Search for Bursts of Gravitational Radiation,"* Phys. Rev. Lett. **31**, 326 (1973).

[15] P. Kafka and L. Schnupp, *"Final Result of the Munich-Frascati Gravitational Radiation Experiment,"* Astron. Astrophys. **70**, 97–103 (1973).

[16] R. Weiss, *"Electromagnetically Coupled Broadband Gravitational Antenna,"* RLE Quarterly Progress Report **105**, 54 (1973).

[17] The LIGO Scientific Collaboration, *"LIGO: the Laser Interferometer Gravitational-Wave Observatory,"* Proposal of the Consortium, 10th November (2011).

[18] The Virgo Collaboration, *"Status of Virgo,"* Class. Quant. Grav. **25**, 114045 (2008).

[19] H. Grote (for the LIGO Scientific Collaboration), *"The GEO 600 status,"* Class. Quant. Grav. **27**, 084003 (2010).

[20] J. Mizuno, K. A. Strain, P. G. Nelson, J. M. Chen, R. Schilling, A. Rüdiger, W. Winkler and K. Danzmann, *"Resonant sideband extraction: a new configuration for interferometric gravitational-wave detectors,"* Phys. Rev. A **175**, 273–276 (1993).

[21] G. Heinzel, J. Mizuno, R. Schilling, A. Rüdiger, W. Winkler and K. Danzmann, *"An experimental demonstration of resonant sideband extraction for laser-interferometric gravitational-wave detectors,"* Phys. Lett. A **217**, 305 (1996).

[22] The LIGO Scientific Collaboration & The Virgo Collaboration, *"An upper limit on the stochastic gravitational-wave background of cosmological origin,"* Nature **460**, 990 (2009).

[23] J. Abadie et al., *"Search for gravitational waves from low mass compact binary coalescence in LIGO's sixth science run and Virgo's science runs 2 and 3,"* Phys. Rev. D **85**, 082002 (2012).

[24] B. Willke et al., *"The GEO-HF project,"* Class. Quantum Grav. **23**, S207–S214 (2006)

[25] J. Abadie et al., *"A gravitational wave observatory operating beyond the quantum shot-noise limit,"* Nature Physics **7**, 962 - 965 (2011).

[26] G. M. Harry (for the LIGO Scientific Collaboration), *"Advanced LIGO: the next generation of gravitational-wave detectors,"* Class. Quantum Grav. **27**, 084006 (2010).

[27] T. Accadia and B. L. Swinkels (for the VIRGO Collaboration), *"Commissioning status of the Virgo interferometer,"* Class. Quantum Grav. **27**, 084002 (2010).

[28] IndIGO - Indian Initiative in Gravitaional-wave Observation, *"LIGO-INDIA - Proposal for an interferometric gravitational-wave observatory,"* Rep. Prog. Phys. **72**, 076901 (2009). `http://www.gw-indigo.org`

[29] S. Kawamura, *"Ground-based interferometers and ther science reach,"* Class. Quantum Grav. **27**, 084001 (2010).

[30] K. Kuroda (on behalf of the LCGT Collaboration1), *"Status of LCGT,"* Class. Quantum Grav **27**, 084004 (2010)

[31] M. Punturo et al., *"The third generation of gravitational-wave observatories and their science reach,"* Class. Quantum Grav. **27**, 084007 (2010).

[32] ET Science Team, *"Einstein gravitational wave telescope. Conceptual design study,"* Internal report ET-0106C-10 (2011).

[33] S. Goßler, *"The suspension systems of the interferometric gravitational-wave detector GEO 600,"* PhD thesis, Leibniz Universität Hannover, (2004).

[34] V. B. Braginsky and F. Ya. Khalili , *"Quantum Measurements,"* Cambridge University Press, Cambridge, (1992).

[35] P. R. Saulson, *"Thermal noise in mechanical experiments,"* Phys. Rev. D **42**, 2437–2445 (1990).

[36] R. Nawrodt, S. Rowan, J. Hough, M. Punturo, F. Ricci, J.-Y. Vinet, *"Challenges in thermal noise for 3rd generation of gravitational wave detectors,"* Gen. Relativ. Gravit. **43**, 593-622, (2011).

[37] V. B. Braginsky, M. L. Gorodetsky, S. P. Vyatchanin, *"Thermodynamical fluctuations and photo-thermal shot noise in gravitational wave antennae,"* Phys. Rev. A **264**, 1 (1999).

[38] V. B. Braginsky, M. L. Gorodetsky, and S. P. Vyatchanin, *"Thermo-refractive noise in gravitational-wave antennae,"* Phys. Rev. A **271**, 303-307 (2000).

[39] S. Hild, H. Lück, W. Winkler, K. Strain, H. Grote, J. Smith, M. Malec, M. Hewitson, B. Willke, J. Hough, K. Danzmann, *"Measurement of a low-absorption sample of OH-reduced fused silica,"* Appl. Opt. **45**, 7269 (2006).

[40] W. Winkler, K. Danzmann, A. Rüdiger, R. Schilling, *"Heating by optical absorption and the performance of interferometric gravitational-wave detectors,"* Phys. Rev. A **44**, 7022 (1991).

[41] K. A. Strain, K. Danzmann, J. Mizuno, R. G. Nelson, A. Rüdiger, R. Schilling, W. Winkler, *"Thermal lensing in recycling interferometric gravitational wave detectors,"* Phys. Lett. A **194**, 124 (1994).

[42] J. Degallaix, *"Compensation of strong thermal lensing in advanced interferometric gravitational waves detectors,"* PhD thesis, University of Western Australia, (2006).

[43] R. L. Byer, *"Gravitational Astronomy: Instrument Design and Astrophysical Prospects,"* D. E. McClelland and H.-A. Bachor (ed.), World Scientific, Singapore (1990).

[44] R. W. P. Drever, *"Concepts for extending the ultimate sensitivity of interferometric Gravitational Wave Detectors Using Non-Transmissive Optics with Diffractive or Holographic Coupling,"* Proceedings of the Seventh Marcel Grossman Meeting on General Relativity M. Keiser and R.T. Jantzen (ed.), World Scientific, Singapore (1995).

[45] R. Nawrodt, A. Zimmer, T. Koettig, T. Clausnitzer, A. Bunkowski, E. B. Kley, R. Schnabel, K. Danzmann, S. Nietzsche, W. Vodel, A. Tünnermann and P. Seidel, *"Mechanical Q-factor measurements on a test mass with a structured surface,"* New J. Phys. **9**, 225 (2007).

[46] R. Nawrodt et al., *"High mechanical Q-factor measurements on silicon bulk samples,"* Journal of Physics: Conference Series **122**, 012008 (2008).

[47] Homepage of the Sonderforschungsbereich TR7, `http://wwwsfb.tpi.uni-jena.de/`

[48] A. Bunkowski, O. Burmeister, K. Danzmann, R. Schnabel, T. Clausnitzer, E.-B. Kley, A. Tünnermann, *"Optical Characterization of ultra-high diffraction efficiency gratings,"* Appl. Opt **45**, 23 5795 (2006).

[49] A. Freise, A. Bunkowski and R. Schnabel, *"Phase and alignment noise in grating interferometers,"* New Journal of Physics **9**, 433 (2007).

[50] A. Bunkowski, *"Laser interferometry with gratings,"* PhD thesis, Leibniz Universität Hannover, (2006).

[51] O. Burmeister, *"Optical properties of 3-port-grating coupled cavities,"* PhD thesis, Leibniz Universität Hannover, (2009).

[52] D. Friedrich, O. Burmeister, A. Bunkowski, T. Clausnitzer, S. Fahr, E.-B. Kley, A. Tünnermann, K. Danzmann, R. Schnabel, *"Diffractive beam splitter characterization via a power-recycled interferometer,"* Opt. Lett. **33**, 101 (2008).

[53] S. Fahr, T. Clausnitzer, E.-B. Kley and A. Tünnermann, *"Reflective diffractive beam splitter for laser interferometers,"* Appl. Opt. **46**, 6092 (2007).

[54] G. M. Harry, A. M. Gretarsson, P. R. Saulson, S. E. Kittelberger, S. D. Penn, W. J. Startin, S. Rowan, M. M. Fejer, D. R. M. Crooks, G. Cagnoli, J. Hough, N. Nakagawa, *"Thermal noise in interferometric gravitational wave detectors due to dielectric optical coatings,"* Class. Quantum Grav. **19**, 897 (2002).

[55] D. R. M. Crooks, G. Cagnoli, M. M. Fejer, A. Gretarsson, G. Harry, J. Hough, N. Nakagawa, S. D. Penn, R. Route, S. Rowan, P. H. Sneddon, *"Experimental measurements of coating mechanical loss factors,"* Class. Quantum Grav. **21**, S1059 (2004).

[56] G. M. Harry, H. Armandula, E. Black, D. R. M. Crooks, G. Cagnoli, J. Hough, P. Murray, S. Reid, S. Rowan, P. Sneddon, M. M. Fejer, R. Route, S. D. Penn, *"Thermal noise from optical coatings in gravitational wave detectors,"* Appl. Opt. **45**, 1569 (2006).

[57] I. Martin, I et al., *"Measurements of a low-temperature mechanical dissipation peak in a single layer of Ta_2O_5 doped with TiO_2,"* Class. Quantum Grav. **25**, 055005 (2008).

[58] F. Ya. Khalili, *"Reducing the mirrors coating noise in laser gravitational-wave antennae by means of double mirrors,"* Phys. Lett. A **334**, 67 (2005).

[59] A. Bunkowski, O. Burmeister, D. Friedrich, K. Danzmann, R. Schnabel, *"High reflectivity grating waveguide coatings for 1064 nm,"* Class. Quantum Grav. **23**, 7297, (2006).

[60] F. Brückner, T. Clausnitzer, O. Burmeister, D. Friedrich, E.-B. Kley, K. Danzmann, A. Tünnermann, R. Schnabel, *"Monolithic dielectric surfaces as new low-loss light-matter interfaces,"* Opt. Lett. **33**, 264 (2008).

[61] F. Brückner, D. Friedrich,T. Clausnitzer, M. Britzger, O. Burmeister, K. Danzmann, E.-B. Kley, A. Tünnermann, and R. Schnabel, *"Realization of a Monolithic High-Reflectivity Cavity Mirror from a Single Silicon Crystal,"* Phys. Rev. Lett. **104**, 163903 (2010).

[62] S Kroker, F. Brückner, E.-B. Kley, and A. Tünnermann, *"Enhanced angular tolerance of resonant waveguide grating reflectors,"* Opt. Lett. **36**, 537–539 (2011).

[63] J. Turunen and F. Wyrowski, *"Diffraction Optics for Industrial and Commercial Applications,"* Akademie Verlag, Berlin (1997).

[64] R. Schnabel, O. Burmeister, A. Bunkowski, A.Thühring, E.-Rinkleff, and K. Danzmann, *"Laser Device"* International patent application, PCT/EP 2006/062626 (2006).

[65] R. Lang, K. Kobayashi, *"External Optical Feedback Effects on Semiconductor Injection Laser Properties,"* IEEE Journal of Quantum Electronics **16**, 347–355 (1980).

[66] M. W. Flemming and A. Mooradian, *"Spectral characteristics of external-cavity controlled semiconductor lasers,"* IEEE Quantum Electron. **17**, 44-59 (2005).

[67] M. G. Littman and H. J. Metcalf, *"Spectrally narrow pulsed dye laser without beam expander,"* Appl. Opt. **17**, 2224-2227 (1978).

[68] C. E. Wieman and L. Hollberg, *"Using diode lasers for atomic physics,"* Rev. Sci. Instrum. **62**, 1-20 (1991).

[69] A. Wicht, M. Rudolf, P. Huke, R.-H. Rinkleff, and K. Danzmann, *"Grating enhanced external cavity diode laser,"* Appl. Phys. B **78**, 137-144 (2004).

[70] B. Willke, N. Uehara, E. K. Gustafson, R. L. Byer, *"Spatial and temporal filtering of a 10-W Nd:YAG laser with a Fabry-Perot ring-cavity premode cleaner,"* Opt. Lett. **23**, 1704-1706 (1998).

[71] D. H. Martz, H. T. Nguyen, D. Patel, J. A. Britten, D. Alessi, E. Krous, Y. Wang, M. A. Larotonda, J. George, B. Knollenberg, B. M. Luther, J. J. Rocca and C. S. Menoni, *"Large area high efficiency broad bandwidth 800 nm dielectric gratings for high energy laser pulse compression,"* Opt. Express **17**, 23809–23816 (2009).

[72] C. Palmer, *"Diffraction Gratings Handbook,"* Thermo RGL, Rochester (2002).

[73] K.-X. Sun, R. L. Byer, *"All-reflective Michelson, Sagnac, and Fabry-Perot interferometers based on grating beam splitters,"* Opt. Lett. **23**, 567 (1998).

[74] P. Lu, *"Diffraction Gratings for Optical Sensing,"* PhD thesis, Stanford University (2009).

[75] L.M. Hobrock, H.L. Gravin, R.J. Withrington, and C.T. Wellman, *"Method for fabrication of low efficiency diffraction gratings and product obtained thereby,"* May 9 1989. US Patent 4,828,356.

[76] M. Nevière and E. Popov, *"Light propagation in periodic media,"* Marcel Dekker, NewYork (2003).

[77] F. Brückner, *"Advanced mirror concepts for high-precision metrology,"* PhD thesis, Friedrich-Schiller Universität Jena, (2010).

[78] D. Friedrich, *"Laser interferometry with coating free mirrors,"* PhD thesis, Leibniz Universität Hannover, (2011).

[79] T. Clausnitzer, *"Kontrolle der Beugungseffizienzen dielektrischer Gitter,"* PhD thesis, Friedrich-Schiller Universität Jena, (2007).

[80] Unigit - A rigorous grating solver, `http://www.unigit.com/`

[81] Institut für Angewandte Physik, Friedrich-Schiller-Universität Jena, `http://www.iap.uni-jena.de/`

[82] B. W. Shore, M. D. Perry, J. A. Britten, R. D. Boyd, M. D. Feit, H. T. Nguyen, R. Chow, G. E. Loomis, and L. Li, *"Design of high-efficiency dielectric reflection gratings,"* J. Opt. Soc. Am. A. **14**, 1124 (1997).

[83] A. Bunkowski, O. Burmeister, P. Beyersdorf, K. Danzmann, R. Schnabel, T. Clausnitzer, E.-B. Kley, A. Tünnermann, *"Low-loss grating for coupling to a high-finesse cavity,"* Opt. Lett. **29**, 2342 (2004).

[84] A. Duparré, *"Light scattering of thin dielectric films"* in Handbook of Optical Properties - Thin Films for Optical Coatings, R.E. Hummel, K.H. Guenther, eds. (CRC Press, Boca Raton, 1995).

[85] O. Burmeister, *"Fabry-Perot Resonatoren mit diffraktiven Einkopplern,"* Diploma thesis, Leibniz Universität Hannover (2005).

[86] F. Brückner, *Personal communication and internal documentation* Hannover, Jena (2011).

[87] The large area grating shown in Fig 2.4 (b) was processed with the newly installed EBL instrument in Jena (Type: Vistec SB350 OS), `http://www.vistec-semi.com/products-applications/products/vistec-sb351/` Hannover, (April 2012).

[88] A. E. Siegman, *"Lasers"* University Science Books, Sausalito (1986).

[89] A. Bunkowski, O. Burmeister, K. Danzmann, R. Schnabel, *"Input-output relations for a 3-port grating coupled Fabry-Perot cavity,"* Opt. Lett. **30**, 1183 (2005).

[90] A. Thüring, *"Investigations of coupled and Kerr non-linear optical resonators,"* PhD thesis, Leibniz Universität Hannover, (2009).

[91] B. J. Meers, *"Recycling in laser-interferometric gravitational-wave detectors,"* Phys. Rev. D **38**, 2317 - 2326 (1988).

[92] P. Fritschel, D. Shoemaker, R. Weiss, *"Demonstration of light recycling in a Michelson interferometer with Fabry-Perot cavities,"* Appl. Opt. **31**, 1412 (1992).

[93] O. Burmeister, M. Britzger, A. Thüring, D. Friedrich, F. Brückner, K. Danzmann, and R. Schnabel, *"All-reflective coupling of two optical cavities with 3-port diffraction gratings,"* Opt. Express **18**, 9119-9132 (2010).

[94] M. Britzger, D. Friedrich, S. Kroker, F. Brückner, O. Burmeister, E. B. Kley, A. Tünnermann K. Danzmann, and R. Schnabel, *"Diffractively coupled Fabry-Perot resonator with power-recycling,"* Opt. Express **16**, 14964-14975 (2011).

[95] T. Clausnitzer, E.-B. Kley, A. Tünnermann, A. Bunkowski, O. Burmeister, R. Schnabel, K. Danzmann, S. Gliech, and A. Duparré, *"Ultra low-loss low-efficiency diffraction gratings,"* Opt. Express **13**, 4370 (2005).

[96] A. Thüring, R. Schnabel, H. Lück, and K. Danzmann, *"Detuned Twin-Signal-Recycling for ultrahigh-precision interferometers,"* Opt. Lett. **32**, 985 (2007).

[97] J. Poirson, F. Bretenaker, M. Vallet, and A. L. Floch, *"Analytical and experimental study of ringing effects in a fabry-perot cavity. Application to the measurement of high finesses,"* J. Opt. Soc. Am. B **14**, 2811-2817.

[98] G. Heinzel, *"Advanced optical techniques for laser-interferomertric gravitational-wave detectors,"* PhD thesis, Leibniz Universität Hannover, (1999).

[99] E. D. Black, *"An introduction to Pound-Drever-Hall laser frequency stabilization,"* Am. J. Phys. **69**, 79 (2001).

[100] M. Malec, *"Commissioning of advanced, dual-recycled gravitational wave detectors: simulations of complex optical systems guided by the phasor picture,"* PhD thesis, Leibniz Universität Hannover, (2006).

[101] A. Freise, "FINESSE *(Frequency domain INterferomEter Simulation SoftwarE 0.99.8,"*
`http://www.gwoptics.org/finesse/`

[102] R. Schnabel, N. Mavalvala, D. E. McClelland and P. K. Lam, *"Quantum metrology for gravitational wave astronomy,"* Nat. Commun. **1**, 121 (2010).

[103] A. Samblowski, *"State Preparation for Quantum Information Science and Metrology,"* PhD thesis, Leibniz Universität Hannover (2012).

[104] M. Britzger, M. H. Wimmer, A. Khalaidovski, D. Friedrich, S. Kroker, F. Brückner, E.-B. Kley, K. Danzmann, and R. Schnabel, *"Michelson interferometer with diffractively-coupled arm resonators in second-order Littrow configuration,"* Opt. Express. **20**, 25400–25408 (2012).

[105] M. Wimmer, *"Interferometrie mit gittergekoppelten Arm-Resonatoren,"* Diplomarbeit, Leibniz Universität Hannover (2010).

[106] R. W. P. Drever, J. L. Hall, F. V. Kowalski, J. Hough, G. M. Ford, A. J. Munley, and H. Ward, *"Laser Phase and Frequency Stabilization using an Optical Resonator,"* Appl. Phys. B. **31**, 97-105 (1983).

[107] M. Mehmet, *"Squeezing at 1550 nm,"* PhD thesis, Leibniz Universität Hannover (2012).

[108] H. Kogelnik and T. Li,, *"Laser Beams and Resonators,"* Appl. Opt. **5**, 1550-1567 (1966).

[109] F. K. Kneubühl, M. W. Sigrist, *"Laser,"* Teubner, Leipzig (1999).

[110] M. Britzger, D. Friedrich, S. Kroker, F. Brückner, O. Burmeister, E. B. Kley, A. Tünnermann K. Danzmann, and R. Schnabel, *"Pound–Drever–Hall error signals for the length control of three-port grating coupled cavities,"* Appl. Opt. **50**, 4340-4346 (2011).

[111] F. Brückner, *Personal communication* Hannover, Jena (2010).

[112] N. Lastzka,, *JamMt - Just another mode matching tool* `http://www.sr.bham.ac.uk/dokuwiki/doku.php?id=geosim:jammt` Hannover, (August 2012)

[113] D. Shoemaker, R. Schilling, L. Schnupp, W. Winkler, K. Maischberger, A. Rüdiger, *"Noise behavior of the Garching 30-meter prototype gravitational-wave detector,"* Phys. Rev. D **38**, 423-432 (1988).

[114] T. Maiman, *"Solid state laser and iraser studies,"* Solid State Electronics, **4**, 236–249 (1962).

[115] R. N. Hall, I. Ismailov, J. D. Kingsley, T. J. Soltys and R. O. Carlson, *"Coherent Light Emission From GaAs Junctions,"* Phys. Rev. Lett. **9**, 366-368 (1962).

[116] W. Demtröder, *"Laser Spectroscopy,"* Springer Verlag, 3. Auflage (2002).

[117] J. S. Neergaard-Nielsen, B. Melholt Nielsen, C. Hettich, K. Molmer and E. S. Polzik, *"Generation of a Superposition of Odd Photon Number States for Quantum Information Networks,"* Phys. Rev. Lett. **97**, 083604 (2006).

[118] P. G. Eliseev, G. E. Fenner, M. A. Man'ko, V. P. Strakhov, *"Injection Semiconductor Laser with Compound Resonator,"* ZhETF Pis ma Redaktsiiu **9**, 594 (1969).

[119] T. Numai, *"Fundamentals of Semiconductor Lasers (Springer Series in Optical Sciences),"* Springer, 1st edition, 2010.

[120] J. Ohtsubo, *"Semiconductor Lasers,"* Springer, 1st edition, 2007.

[121] F. Träger (Ed.), *"Handbook of Lasers and Optics,"* Springer, 1st edition, 2007.

[122] R. W. Tkach, A. R. Chraplyvy, *"Regimes of feedback effects in 1.5 μm distributed feedback lasers,"* Journal of Lightwave Technology **4**, 1655–1661 (1986).

[123] B. Hemb, *"Diodenlaser mit Dreiport-Gitter-Resonator in zweiter Ordnung Littrow,"* Diplomarbeit, Leibniz Universität Hannover (2010).

[124] R. W. Tkach, A. R. Chraplyvy, *"Linewidth broadening and mode splitting due to weak feedback in single-frequency 1.5 μm lasers,"* Electron. Lett., **47**, 1081–183 (1985).

[125] Encyclopedia of Laser Physics and Technology , `http://www.rp-photonics.com/encyclopedia.html`

[126] M. Gilowski, C. Schubert, M. Zaiser, W. Herr, T. Wübbena, T. Wendrich, T. Müller, E. M. Rasel, W. Ertmer, *"Narrow bandwidth interference filter-stabilized diode laser systems for the manipulation of neutral atoms,"* Opt. Comm. **280**, 443-447 (2007).

[127] C. J. Hawthorn, K. P. Weber, and R. E. Scholten, *"Littrow configuration tunable external cavity diode laser with fixed direction output beam,"* Rev. Sci. Instrum. **72**, 4477 (2001).

[128] M. Britzger, A. Khalaidovski, B. Hemb, E.-B. Kley, F. Brückner, R.-H. Rinkleff, K. Danzmann, and R. Schnabel, *"External-cavity diode laser in second order Littrow configuration,"* Opt. Lett. **37**, 3117–3119 (2012).

[129] *eagleyard - Producer of Laserdiodes,* `http://www.eagleyard.com` Data sheet of the laser diode type: EYP-RWL-1060-00100-0750-SOT01-0000.

[130] T. Clausnitzer, *Personal communication and internal documentation*, Hannover, Jena (2009).

[131] TOPTICA - Photonics,
`http://www.toptica.com/`

[132] Tafelmaier - Thin Film Technology,
`http://www.tafelmaier.de`

[133] A. Khalaidovski, *"Beyond the Quantum Limit – A Squeezed-Light Laser for GEO 600,"* PhD thesis, Leibniz Universität Hannover (2012).

[134] B. W. Barr, M. P. Edgar, J. Nelson, M. V. Plissi, S. H. Huttner, B. Sorazu, K. A. Strain, O. Burmeister, M. Britzger, D. Friedrich, R. Schnabel, K. Danzmann, J. Hallam, A. Freise, T. Clausnitzer, F. Brückner, E.-B. Kley, and A. Tünnermann, *"Translational, rotational, and vibrational coupling into phase in diffractively coupled optical cavities,"* Opt. Lett. **36**, 2746 (2011).

[135] M. P. Edgar, B. W. Barr, J. Nelson, M. V. Plissi, K. A. Strain, O. Burmeister, M. Britzger, K. Danzmann, R. Schnabel, T. Clausnitzer, F. Brückner, E.-B. Kley, A. Tünnermann, *"Experimental demonstration of a suspended diffractively coupled optical cavity,"* Opt. Lett. **34**, 3184 (2009).

Acknowledgements

Working at the Albert Einstein Institute and doing research within the ambitious international gravitational physics community is an outstanding experience. I am very glad to have been part of this community. Excellent research conditions, infrastructural support, and the countless helping hands and friendly colleagues made the daily work at the institute very enjoyable. I would like to thank Prof. Karsten Danzmann for leading this place with an inspiring enthusiasm for physics and science in general.

I would like to express my gratitude to Prof. Roman Schnabel for being my advisor from the beginning of my diploma thesis and for giving me the opportunity to become a member of his group. It was a privilege to take part in your zeal for research and to learn from you. I would like to thank all members of the Schnabel-group, both past and present, for the cheerful atmosphere.

For pioneering the research field of diffractive optics at the AEI and for introducing me to it I thank Alexander Bunkowski, Oliver Burmeister and Daniel Friedrich. I had fun working in the lab with Maximilian Wimmer and Björn Hemb. A special thanks goes to my colleagues in Jena for their constant support; Tina Clausnitzer, Stefanie Kroker and Frank Brückner. The author likes to thank André Thüring, Henning Vahlbruch, James DiGuglielmo, Boris Hage, Aiko Samblowski and Alexander Khalaidovski for 'fruitful' discussions. I had a good time in Callinstr. 36 with my building mates Henning Kaufer, Stefan Ast, Melanie Meinders, Oliver Gerbering, Marina Dehne, Jens Reiche and all the others from the LISA group. For proof reading I thank Stefan, Henning, Daniel, Marina, Albrecht Rüdiger, Michèle Heurs and Alexander.

I thank Prof. Eberhard Tiemann for supervising and leading the EGC.

Special thanks go to Stefan Pfalz and the staff of QUEST for giving me the opportunity to take skills beyond science within the outreach project 'DFG-Science-TV'. I thank all the 'wave hunters' that participated in this project, and Prof. Danzmann and Prof. Schnabel for their support.

For being the buddies that you need to have inside and outside of the institute I thank Daniel Friedrich, Moritz Mehmet and Tobias Meier.

I would like to thank my parents and my brother for support and impulses throughout my work. Thank you Sarah for patience, encouragement and love.

Curriculum vitae

Michael Britzger
Teichstraße 3
30449 Hannover

Born on March 12th, 1979 in Marktoberdorf, Germany

University studies

02/2008 - present	Scientific assistant, Leibniz Universität Hannover
02/2008 - present	Doctoral studies in Physics, Leibniz Universität Hannover
02/2008 - present	Member of the International Max Planck Research School (IMPRS) on Gravitational Wave Astronomy
02/2008 - 12/2011	Member of the European Graduate College (EGC) "Interference and Quantum Applications"
12/2007	Diploma thesis, Leibniz Universität Hannover, Title: *Dreiport-Gitter-Resonator mit Power-Recycling*
09/2005 - 03/2006	Physics studies, University of Salamanca, Spain
10/2002 - 12/2007	Physics studies, Leibniz Universität Hannover
03/2002 - 09/2002	Economics/Politics studies, University of Vienna, Austria
10/1999 - 02/2002	Economics studies, University of Hohenheim

Community service

08/1998 - 09/1999	Civil service, Kreiskrankenhaus Marktoberdorf

Education

06/1998	Abitur, Peter-Dörfler-Gymnasium Marktoberdorf

Publications

Publications within the diffractive optics project

1. M. Britzger, M. H. Wimmer, A. Khalaidovski, D. Friedrich, S. Kroker, F. Brückner, E.-B. Kley, K. Danzmann, and R. Schnabel, *"Michelson interferometer with diffractively-coupled arm resonators in second-order Littrow configuration,"* Opt. Express. **20**, 25400–25408 (2012).

2. M. Britzger, A. Khalaidovski, B. Hemb, E.-B. Kley, F. Brückner, R.-H. Rinkleff, K. Danzmann, and R. Schnabel, *"External-cavity diode laser in second order Littrow configuration,"* Opt. Lett. **37**, 3117–3119 (2012).

3. M. Britzger, D. Friedrich, S. Kroker, F. Brückner, O. Burmeister, E.-B. Kley, A. Tünnermann, K. Danzmann, and R. Schnabel, *"Diffractively coupled Fabry-Perot resonator with power-recycling,"* Opt. Express **19**, 14964–14975 (2011).

4. M. Britzger, D. Friedrich, S. Kroker, F. Brückner, O. Burmeister, E.-B. Kley, A. Tünnermann, K. Danzmann, and R. Schnabel, *"Pound–Drever–Hall error signals for the length control of three-port grating coupled cavities,"* Appl. Opt. **50**, 4340–4346 (2011).

5. ET Science Team, J. Abernathy, ... , M. Britzger, ... , K. Yamamoto, *"Einstein gravitational wave telescope. Conceptual design study,"* Internal report ET-0106C-10 (2011).

6. B. W. Barr, M. P. Edgar, J. Nelson, M. V. Plissi, S. H. Huttner, B. Sorazu, K. A. Strain, O. Burmeister, M. Britzger, D. Friedrich, R. Schnabel, K. Danzmann, J. Hallam, A. Freise, T. Clausnitzer, F. Brückner, E.-B. Kley, and A. Tünnermann, *"Translational, rotational, and vibrational coupling into phase in diffractively coupled optical cavities,"* Opt. Lett. **36**, 2746 (2011).

7. D. Friedrich, B. W. Barr, F. Brückner, S. Hild, J. Nelson, J. Macarthur, M. V. Plissi, M. P. Edgar, S. H. Huttner, B. Sorazu, S. Kroker, M. Britzger, E.-B. Kley, K. Danzmann, A. Tünnermann, K. A. Strain, and R. Schnabel, *"Waveguide*

grating mirror in a fully suspended 10 meter cavity," Opt. Express, **18**, 14955–14963 (2011).

8. F. Brückner, D. Friedrich, T. Clausnitzer, M. Britzger, O. Burmeister, K. Danzmann, E.-B. Kley, A. Tünnermann, and R. Schnabel, *"Realization of a Monolithic High-Reflectivity Cavity Mirror from a Single Silicon Crystal,"* Phys. Rev. Lett., **104**, 163903 (2010).

9. R. Schnabel, M. Britzger, F. Brückner, O. Burmeister, K. Danzmann, J. Dück, T. Eberle, D. Friedrich, H. Lück, M. Mehmet, R. Nawrodt, S. Steinlechner, and B. Willke, *"Building blocks for future detectors: Silicon test masses and 1550 nm laser light,"* Journal of Physics: Conf. Series, **228**, 012029 (2010).

10. O. Burmeister, M. Britzger, A. Thüring, D. Friedrich, F. Brückner, K. Danzmann, and R. Schnabel, *"All-reflective coupling of two optical cavities with 3-port diffraction gratings,"* Opt. Express, **18**, 9119–9132 (2010).

11. F. Brückner, D. Friedrich, T. Clausnitzer, O. Burmeister, M. Britzger, E.-B. Kley, K. Danzmann, A. Tünnermann, and R. Schnabel, *"Demonstration of a cavity coupler based on a resonant waveguide grating,"* Opt. Express, **17**, 163–169 (2009).

12. M. P. Edgar, B. W. Barr, J. Nelson, M. V. Plissi, K. A. Strain, O. Burmeister, M. Britzger, K. Danzmann, R. Schnabel, T. Clausnitzer, F. Brückner, E.-B. Kley, A. Tünnermann, *"Experimental demonstration of a suspended diffractively coupled optical cavity,"* Opt. Lett. **34**, 3184 (2009).

13. F. Brückner, D. Friedrich, M. Britzger, T. Clausnitzer, O. Burmeister, E.-B. Kley, K. Danzmann, A. Tünnermann, and R. Schnabel, *"Encapsulated subwavelength grating as a quasi-monolithic resonant reflector,"* Opt. Express, **17**, 24334–24341 (2009).

14. D. Friedrich, O. Burmeister, M. Britzger, A. Bunkowski, T. Clausnitzer, S. Fahr, E.-B. Kley, A. Tünnermann, K. Danzmann and R. Schnabel, *"Power-recycled Michelson interferometer with a 50/50 grating beam splitter,"* J.Phys.: Conf. Ser., **122**, 012018 (2008).

15. M. Britzger, *"Dreiport-Gitter-Resonator mit Power-Recycling"* Diplomarbeit, Leibniz Universität Hannover (2007).

Publications within the LIGO Scientific Collaboration

16. J. Abadie, ... , M. Britzger, ... , J. Zweizig, *"All-sky search for gravitational-wave bursts in the second joint LIGO-Virgo run,"* Phys. Rev. D **85**, 122007 (2012).

17. J. Abadie, ... , M. Britzger, ... , J. Zweizig, *"Upper limits on a stochastic gravitational-wave background using LIGO and Virgo interferometers at 600–1000 Hz,"* Phys. Rev. D **85**, 122001 (2012).

18. J. Abadie, ... , M. Britzger, ... , J. Zweizig, *"Search for gravitational waves from intermediate mass binary black holes,"* Phys. Rev. D **85**, 102004 (2012).

19. J. Abadie, ... , M. Britzger, ... , J. Zweizig, *"Search for gravitational waves from low mass compact binary coalescence in LIGO's sixth science run and Virgo's science runs 2 and 3,"* Phys. Rev. D **85**, 082002 (2012).

20. J. Abadie, ... , M. Britzger, ... , J. Zweizig, *"All-sky search for periodic gravitational waves in the full S5 LIGO data,"* Phys. Rev. D **85**, 022001 (2012).

21. J. Abadie, ... , M. Britzger, ... , J. Palfreyman, *"Beating the spin-down limit on gravitational wave emission from the Vela pulsar,"* Ap. J. **373**, 93 (2011).

22. J. Abadie, ... , M. Britzger, ... , J. Zweizig, *"Directional Limits on Persistent Gravitational Waves Using LIGO S5 Science Data,"* Phys. Rev. Lett. **107**, 271102 (2011).

23. J. Abadie, ... , M. Britzger, ... , K. Yamaoka, *"Search for gravitational wave bursts from six magnetars,"* Ap.J., **734**, L35 (2011).

24. J. Abadie, ... , M. Britzger, ... , J. Zweizig, *"A gravitational wave observatory operating beyond the quantum shot-noise limit,"* Nature Physics **7**, 962 - 965 (2011).

25. J. Abadie, ... , M. Britzger, ... , J. Zweizig, *"Search for gravitational waves from binary black hole inspiral, merger, and ringdown,"* Phys. Rev. D, **83**, 122005 (2011).

26. J. Abadie, ... , M. Britzger, ... , J. Zweizig, *"Search for gravitational waves associated with the August 2006 timing glitch of the Vela pulsar,"* Phys. Rev. D, **83**, 042001 (2011).

27. J. Abadie, ... , M. Britzger, ... , J. Zweizig, *"Calibration of the LIGO gravitational wave detectors in the fifth science run,"* Nucl. Instrum. Meth. A **624**, 223 - 240 (2010).

28. J. Abadie, ... , M. Britzger, ... , J. Zweizig, *"First search for gravitational waves from the youngest known neutron star,"* Ap.J., **722**, 1504–1513 (2010).

29. J. Abadie, ... , M. Britzger, ... , J. Zweizig, *"Search for gravitational waves from compact binary coalescence in LIGO and Virgo data from S5 and VSR1,"* Phys. Rev. D, **82**, 102001 (2010).

30. J. Abadie, ... , M. Britzger, ... , J. Zweizig, K. Belczynski, *"Predictions for the rates of compact binary coalescences observable by ground-based gravitational-wave detectors,"* Class. Quantum Grav., **27**, 173001 (2010).

31. J. Abadie, ... , M. Britzger, ... , J. Zweizig, *"All-sky search for gravitational-wave bursts in the first joint LIGO-GEO-Virgo run,"* Phys. Rev. D, **81**, 102001 (2010).

32. J. Abadie, ... , M. Britzger, ... , J. Zweizig, *"Search for gravitational-wave inspiral signals associated with short gamma-ray bursts during LIGO's fifth and Virgos's first science run,"* Ap. J., **715**, 1453–1461 (2010).